NGU REPORT 2025.017

Critical metals (P, REE, HFSE, nepheline) in the southern part of the Oslo rift, Vestfold, Norway

GEOLOGY FOR SOCIETY

SINCE 1858

GEOLOGICAL SURVEY OF NORWAY

- NGU -

NGU REPORT 2025.017

Critical metals (P, REE, HFSE, nepheline) in the southern part of the Oslo rift, Vestfold, Norway

GEOLOGICAL SURVEY OF NORWAY
- NGU -

NGU REPORT
Geology for society

Geological Survey of Norway
P.O. Box 6315 Torgarden
NO-7491 Trondheim, Norway
Tel. +47 73 90 40 00

Report no.: 2025.017
ISSN: 0800-3416 (print)
ISSN:2387-35150 (digital)
Grading:

Title: Critical metals (P-REE-HFSE; nepheline) potential in the southern part of the Oslo rift, Vestfold, Norway
Authors: Coint, Nolwenn, Mansur, Eduardo T., Miranda, Ana C.R., Wang, Ying, Szitkar, Florent, Acosta-Gongora, Pedro, Baranwal, Vikas C. and Nasuti, Aziz.
Client: Treschow-Fritzøe AS
County: Norway
Municipality: Larvik, Sandefjord, Siljan, Skien

Map-sheet name (M=1:250.000): Oslo (7), Skien (6)
Map-sheet name (M=1:50.000): Siljan (1713-1), Holmestrand (1813-4), Sandefjord (1813-3), Porsgrunn (1713-2), Stavern (1812-4), Langesund (1712-1), Nordagutu (1713-4)
Deposit name and grid-reference:
Numbers of pages: 92
Price (NOK): 280 NOK

Map enclosures:
Fieldwork carried out: summers 2022 to 2024
Date of report: May 2025
Project no.: 400200
Person responsible: Torkil
Keywords: Fe-Ti-P-(REE) mineralisation, Nb-Zr-REE mineralisation, Critical metals, Oslo Rift, Prospectivity mapping, Supervised machine learning, Drone magnetic survey, Soil geochemistry, Ore petrogenesis

Summary:
Critical metals, such as rare earth elements, phosphorous and high field strength elements (Nb, Ta, Zr, Hf) are essential for advanced technologies, including batteries, renewable energy systems, and electronics. Their growing demand is driving the need for more efficient exploration techniques to locate and extract these resources. One innovative approach to improving mineral exploration involves integrating the various geological disciplines to better predict the location of future resources. This report summarises the scientific results from a project conducted by the geological Survey of Norway in the southern part of the Oslo rift. The project consisted in describing mineral occurrences and associated intrusive rocks, understanding the processes behind the formation of these mineralisation and test various tools that can be used for mineral exploration, including machine learning and prospectivity mapping, drone magnetic survey and geochemical soil survey.

Alkaline magmatism related to the initial opening of the Permian Oslo rift resulted in emplacement of large, nested intrusions of monzodiorite to syenitic composition, locally mineralized in Fe-Ti-P +/- (REE) and Zr-Nb-REE. Uranium-Pb geochronology and Hf isotopes on zircon indicate that magmatism moved from the south (Larvik Plutonic Complex: 295-288 Ma) toward the north (Kiste, Rimstad, Løkka, Siljan-Hvarnes intrusions 284-278 Ma) and that the Kodal Fe-Ti-P-(REE) deposit, previously assumed to belong to the Larvik Plutonic Complex, is instead likely part of the younger set of intrusions. Mineralisation is associated with the two groups of intrusive rocks, however the

one hosted by the youngest set tends to be more voluminous (Kodal I and II and occurrences of the Siljan-Hvarnes intrusion).

Mineralisation can be divided in three sub-types based on their mineralogy and geochemistry: 1) Fe-Ti-P-(REE) mineralisation, associated with monzonite and where ore mineral mainly includes apatite, titanomagnetite, minor ilmenite, monazite and zirconolite, 2) Zr-Nb-REE mineralisation found in syenite and quartz-monzonite, where elements of interest are hosted in zircon, hemo-ilmenite and apatite 3) Zr-Nb-REE pegmatite, also found in syenite and quartz syenite containing zircon, titanite, chevkinite, pyrochlore and possibly minerals from the britholite family. Iron-Ti-P-(REE) mineralisation is the only type of mineralisation that reach volume large enough to be characterized as an ore deposit (Kodal I), however, the numerous occurrences of Zr-Nb-REE-rich rocks in the area does not preclude the existence of larger ore bodies. Field observations, petrographic descriptions, whole-rock and mineral chemistry suggest that silicate-liquid immiscibility processes formed both the Fe-Ti-P-(REE) and Zr-Nb-REE, although in the second case the process is not documented in detail yet.

The second part of the report focuses on methodology. We developed a supervised machine learning routine to construct a regional prospectivity map targeted toward Fe-Ti-P-(REE) mineralisation, integrating airborne geophysics, topography, and whole-rock geochemical datasets. The concept relies on the stark contrast of geochemical and petrophysical properties existing between the ore and host-rock. Results show that prospectivity maps can be used to guide mineral exploration in a region, however a good understanding of the geology is necessary to interpret the data properly. False positives, related to the presence of lakes, rocks with similar geochemical and petrophysical properties as the ore, occur.

Finally, we evaluated two new mineral exploration methods, high-resolution drone magnetic and geochemical soil surveys, in prospective areas highlighted in the prospectivity map. Results show that these methods are complementary, allowing acquisition of datasets at the local scale and can be used to plan future mineral exploration programs such as drilling campaigns.

By combining these methodologies, mineral exploration can be significantly enhanced. The synergy between ore petrogenesis, regional geophysics, soil geochemistry, and drone surveys allows for a multi-faceted approach, reducing exploration costs and increasing the likelihood of successful mineral discoveries. As the demand for critical metals continues to rise, embracing innovative exploration techniques will be essential for meeting future resource needs. Overall, the fusion of these advanced technologies represents a transformative step in the field of mineral exploration.

Table of contents

Supplementary material can be downloaded at

https://www.ngu.no/upload/Publikasjoner/Rapporter/2025/2025_017_vedlegg.zip

1. INTRODUCTION

Phosphorus (P), Rare earth elements (REE), Zirconium (Zr) and Niobium (Nb), also called high field strength elements (HFSE) play a crucial role in the transition to a sustainable, green economy. As the world seeks to reduce carbon emissions and embrace renewable energy technologies, metals are essential in the production of batteries, solar panels, and electric vehicles. Rare earth elements, known for their unique magnetic and optical properties, are vital in advanced technologies that enhance energy efficiency (e.g. Goodenough et al. 2016). Meanwhile, phosphorus is key for sustainable agriculture, contributing to food security (e.g. Ihlen et al. 2014). Together, these elements facilitate the innovations necessary for a greener, more sustainable future and will see their demand increase in the coming years.

The uneven distribution of mineral resources and the extraction/processing industry between countries are associated with a significant supply risk, a strategic parameter now monitored closely by numerous countries. Consequently, elements of interest in this study (REE, P but also Nb and Zr) are all classified as Critical Raw Materials (CRMs) by the EU (https://single-market-economy.ec.europa.eu/sectors/raw-materials/areas-specific-interest/critical-raw-materials_en) based their high economic importance and high supply risk (e.g. Decrée et al. 2023; Goodenough et al. 2016). In 2023, feldspar and nepheline joined the list of CRMs. This project is part of an ongoing effort to map and characterize Critical Raw Materials deposits in Norway.

Large Fe-Ti-P deposits are typically associated either with mafic intrusive systems related to Anorthosite-mangerite-charnockite-granite (AMCG) suites such as Damiao in China; the Bjerkreim-Sokndal layered intrusion in Norway or the Sept-île intrusion in Canada (e.g. Ihlen et al. 2014; Namur et al. 2012; Charlier et al. 2015), or to Iron Oxide Apatite (IOA) deposits where the ore is hosted in strongly altered metavolcanic rocks and where the role of hydrothermal fluids in the formation of the ore remains highly debated (e.g. Kirunavaara, Sweden; Carajás Province, Brazil; El Laco, Chile - (Reich et al. 2022)). Iron-Ti-P-(REE) mineralisation associated with intrusive rocks of intermediate composition, however, have not yet been considered as a potential source for critical metals, although they can locally contain anomalous concentrations of elements such as Fe, Ti, P, REE, Zr and Nb (e.g. Decrée et al. 2023; Coint et al. 2023; Coint et al. 2020; Ihlen et al. 2014; Andersen and Seiersten 1994) and occur in several Norwegian geological provinces (Ihlen et al. 2014). Alkaline rocks also host nepheline syenites, source of nepheline and feldspar concentrate used in the glass industry. Two

nepheline occurrences are associated with the intrusions considered in this study. This project was developed to characterize these mineralized systems and provide new tools for potential future mineral exploration.

Project goals:

- Describe and provide a modern geochemical dataset for the various occurrences of Fe-Ti-P-(REE) mineralisation and Zr-Nb-REE occurrences associated with intermediate and felsic intrusive rocks from the southern part of the Oslo rift.
- Provide a timeline for the emplacement of the various intrusions in the region and understand the extent of interaction between host-rocks and magmas during their emplacement.
- Provide a model explaining how the mineralisation formed.
- Assess the prospectivity for Fe-Ti-P-(REE) mineralisation in the southern part of the Oslo rift.
- Test new potential mineral exploration tools (magnetic drone survey and geochemical soil survey).
- Update the NGU mineral resource database.

This report is associated with downloadable datasets associated with GPS coordinates which can be integrated in Geographical Information System (GIS) software (Supplementary materials).

2. GEOLOGICAL CONTEXT: THE PERMIAN OSLO RIFT

The Oslo Rift (Fig. 1) comprises a 400 km-long and 60–120-km-wide zone that can be broadly divided into two main parts, the Oslo Graben (which encompasses the offset grabens Vestfold, Akershus and Rendal towards the North) and the Skagerrak Graben, which is the southernmost submerged extension of the system (Larsen et al. 2008). The rift developed along the southwest margin of the Baltic Shield, which was formed by accretionary magmatism mainly at 1.75–1.50 Ga (e.g. Slagstad et al. 2020; Bingen et al. 2008; Andersen et al. 2004 and reference therein). The magmatism within the rift is marked by large volumes of extrusive and intrusive rocks with variable geochemical affinity and associated with sedimentary rocks. Overall, its evolution can be subdivided into six main stages: i. a proto-rift stage, ii. an initial basalt stage, iii. a main

plateau-lava and rift-valley stage, iv. a central volcano and calderas stage, v. a syenitic batholith stage, and vi. a termination stage (Olaussen et al. 1994; Sundvoll and Larsen 1990).

The initial proto-rift stage is marked by the deposition of the fluvial and lacustrine sediments of the Asker Group (Dahlgren and Corfu 2001; Olaussen et al. 1994). The following initial rift stage is characterised by widespread mafic magmatism, with the volcanic activity leading to the formation of an up to 800-1500 m-thick lava flow sequence, dated by U-Pb in perovskite and titanite at 300-299 Ma (Corfu and Dahlgren 2008). These volcanic rocks are referred to as B1 basalts and comprise nephelinites, basanites and alkali basalts in Skien (South), transitional compositions in Vestfold-Jeløya and quartz tholeiite (North) in Krokskogen (Neumann et al. 2002).

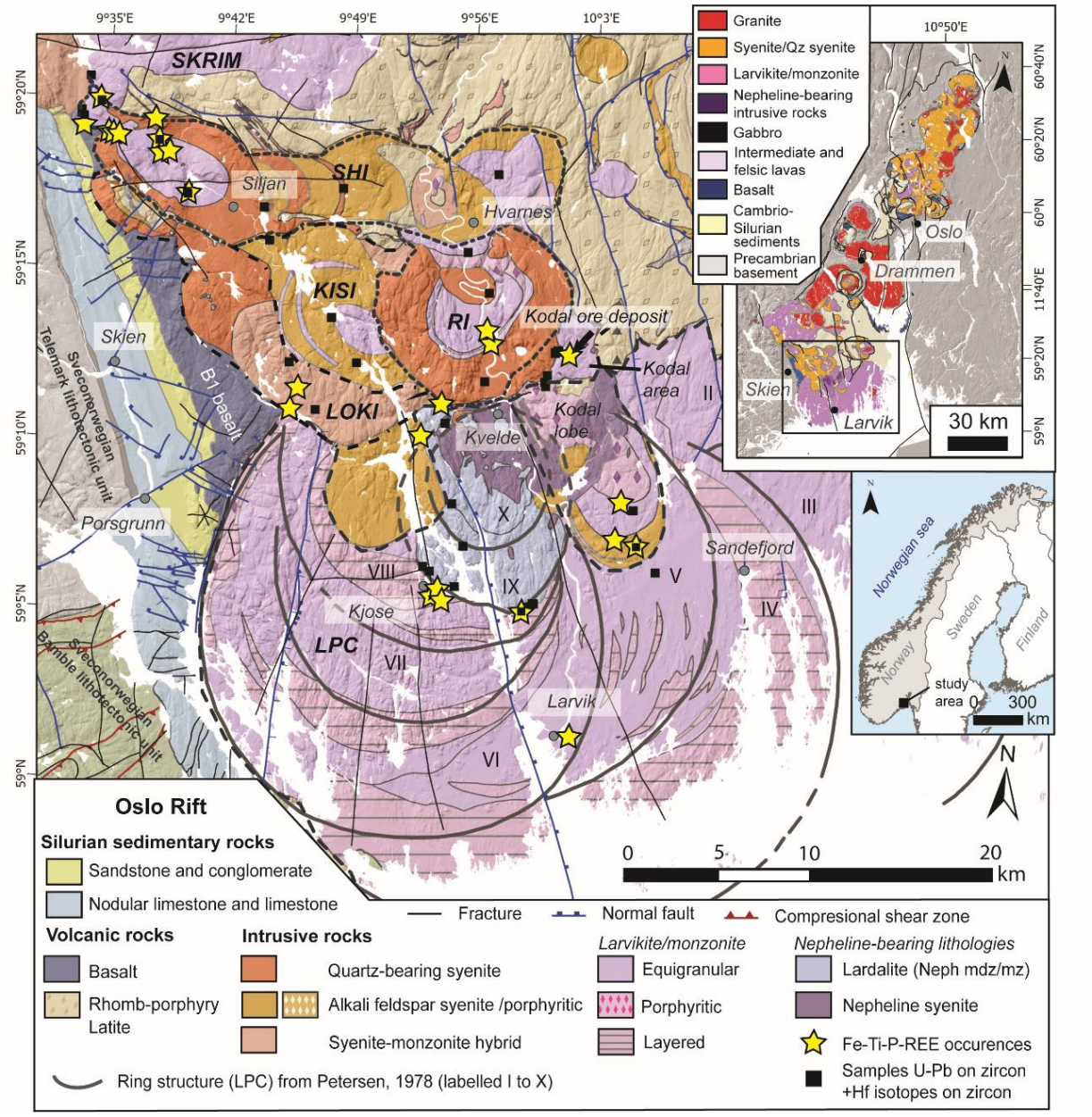

Figure 1: Simplified geologic map of the study area and location of samples collected for geochronology. The light grey dashed lines indicate the delineation of main intrusions. Abbreviations: LPC – Larvik Plutonic Complex; LOKI – Løkka intrusion; RI – Rimstad intrusion; KISI – Kiste intrusion; SHI – Siljan-Hvarnes intrusion. Figure from Mansur et al., submitted.

The volcanic pile reaches a maximum thickness in the central portions of the graben, with only relatively thin intervals (i.e. approximately 15 m thick) at the latitude of Oslo and no volcanic rocks preserved further north (Neumann 2019; Neumann et al. 2004; Neumann et al. 2002; Olaussen et al. 1994). The initial part of the following period, a main plateau-lava and rift-valley stage, overlaps in time with the late stages of basaltic magmatism and is marked by the eruption of rhomb-porphyry lavas. This is coeval with the emplacement of the plutonic counterparts of rhomb-porphyry lavas comprising mainly monzonites and nepheline syenites, which are the subject of this contribution. The most distinct intrusive complex of this stage is

the LPC, which occupies almost the full width of the Oslo Rift at its southern part (Lutro and Nordgulen 2008). The LPC comprises mainly a series of silica slightly over- to undersaturated monzonites with rhomb-shaped ternary feldspar (i.e. local name *larvikites*), reddish quartz-bearing monzonite (i.e. local name *tønsbergite*) and nepheline monzodiorites, nepheline monzosyenites and nepheline syenites (i.e. local name *lardalite*) (Sundvoll and Larsen 1990; Rasmussen et al. 1988; Neumann et al. 1988; Neumann 1980).

The LPC intrusions are broadly distributed within ten successive ring-sections, interpreted as a sequence of intrusive centres, intersecting each other (Petersen 1978), and becoming progressively younger westwards from 299 to 289 Ma (Rämö et al. 2022). In addition, intrusive complexes immediately north of the LPC, namely the Skrim larvikite and the Siljan-Hvarnes Complex yield U-Pb zircon and baddeleyite ages ranging from 281.2 ± 0.6 to 277.3 ± 0.8 Ma (Pedersen et al. 1995). These ages support a progressively younger magmatism north of the LPC. The following two stages of the Oslo Rift mark the initial development of central volcanoes, cauldron collapse and graben fill, with lavas ranging in composition from alkaline olivine basalts to Si-saturated counterparts, and the ensuing emplacement of syenitic to granitic batholiths in central and northern parts of the Oslo Rift, prior to the termination stage (Larsen et al. 2008).

The magmatic rocks emplaced during the main plateau-lava and rift-valley stage of the Oslo Rift also host Fe-Ti-P mineralisation (Fig. 1). The largest and most studied example in the region is the Kodal deposit (Decrée et al. 2023; Ihlen et al. 2014; Andersen and Seiersten 1994; Kragh and Jensen 1991; Lindberg 1985; Bergstøl 1972). The Kodal deposit is poorly exposed, except for an old mining pit area (Fig. 1), where massive nelsonites can be observed. Extensive drilling through the deposit, conducted by Norsk Hydro and Kodal Minerals (1970's-2010's), indicates that the Fe-Ti-P orebody consists of an approximately 2 km-long, and 100 m-thick, tabular, E-W-trending, subvertical orebody, dipping towards the south (Ihlen et al., 2014). Details about Kodal can be found in chapter 3.4.1. Other occurrences associated with the LPC and the Siljan-Hvarnes intrusion (Andersen 2021) have been described, indicating intrusions other than the LPC can host Fe-Ti-P-(REE) occurrences. These are described in more details in chapter 3.3.

3. INTRUSIVE ROCKS AND ASSOCIATED MINERALISATION

A large part of this project was acquiring an adequate whole-rock geochemical dataset to assess the enrichment of the mineralisation in phosphorus and critical metals and provide a regional dataset for the machine learning framework tested as part of this project (see chapter 4). Thus, an initial step of the project was to obtain systematic field descriptions and whole-rock chemical compositions of the main features observed in each of the intrusions to be studied (Fig. 2). We provide below an overview of the areas and intrusions addressed for the purpose of this study. The areas comprise rings V, IX and X of the LPC, the Kodal lobe and Kodal area, and the Rimstad, Kiste, Løkka, Siljan-Hvarnes and Skrim intrusions (Fig. 1).

3.1 Monzodiorite, monzonite and syenite intrusions in the study area

This chapter comprises the description section of a manuscript sent for peer-review publication (Mansur et al., submitted to Norwegian Journal of Geology), as well as a summary of the results, including illustrations and a table from the same manuscript.

3.1.1 The Larvik Plutonic Complex (LPC)

"The lithologies found in the LPC vary according to the position within the intrusive rings. Ring V comprises mainly larvikite and alkali-feldspar syenite. Larvikite is the most abundant lithology, with similar petrographic characteristics as previously described in the literature (Rämö et al. 2022; Rasmussen et al. 1988; Neumann et al. 1988; Neumann 1980). It is predominantly coarse- to medium-grained with monzonitic composition and dominated (more than 80 vol. %) by subhedral to euhedral alkali feldspar and plagioclase (Fig. 2A). Mafic minerals consist of subrounded olivine, subhedral augite, locally containing olivine inclusions, Fe-oxides (Ti-magnetite and ilmenite), apatite, calcic brown or green amphibole and phlogopite form the matrix between the large subhedral rhomb-shaped feldspar and can be associated with interstitial K- feldspars. Although larvikite mostly display an isotropic fabric, the occurrence of oriented feldspar grains locally defines a flow texture (Fig. 3A). In fact, flow textures are remarkable close to contact zones between the lardalite from ring IX and larvikite from ring VIII (Fig. 1). In these areas it is possible to observe the progressive shift of the feldspar orientation from isotropic portions towards flow-dominated zones (Fig. 3B). Alkali-feldspar syenite is less abundant and characterised by euhedral medium-grained alkali feldspar with 1-2 cm augite, Fe-oxides, biotite and minor amphibole and apatite agglomerates (Fig. 3C).

Variations in grain size are observed for both larvikite and syenite with locally fine-grained parts.

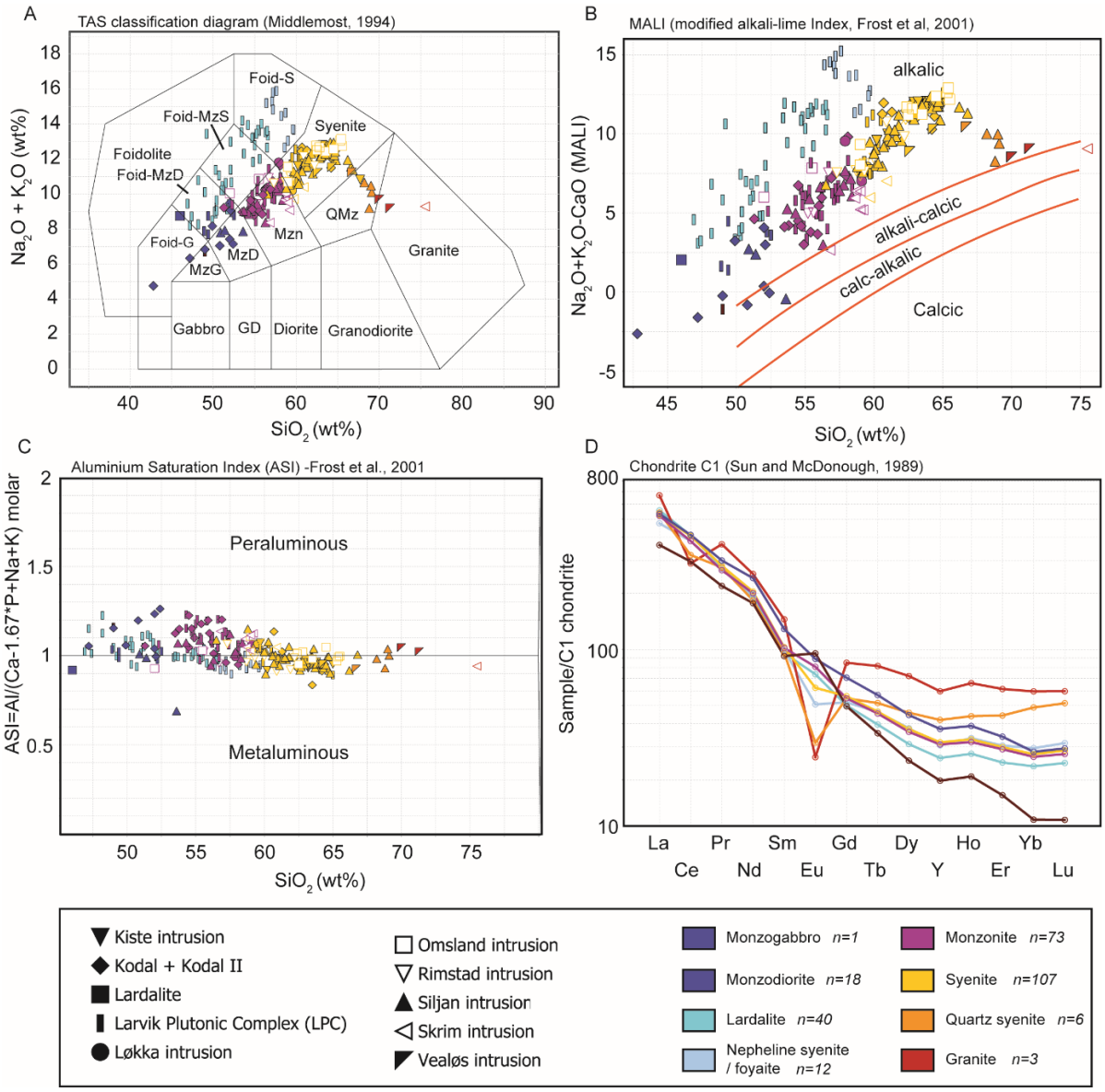

Figure 2: Whole-rock data. A) TAS diagram, MG: monzogabbro, MzD: Monzodiorite, Mz: monzonite, S: syenite, QzMz: quartz monzonite, Foid-S: Foid-syenite or nepheline syenite, Foid-Mz: Foid-monzonite, Foid-MzD: foid-monzodiorite, Foid-G: Foid-gabbro. B) MALI versus SiO_2, C) Aluminium Saturation Index (ASI) versus SiO_2. D) average REE patterns for various lithologies (n= is the number of analyses per lithology).

Samples from rings IX and X represent Si-undersaturated portions of the LPC, comprising mainly lardalite intruded by nepheline syenite. Both terms refer to nepheline-bearing lithologies. Lardalite, which vary between nepheline monzodiorite and syenite (Fig. 2a), display a coarse-grained texture composed mainly of 2-7 cm long rhomb-shaped anorthoclase, 1-4 cm euhedral nepheline and mafic minerals restricted mostly to the space between the feldspar (Fig. 3D).

Figure 3: Field and textural observations. A) Typical medium-grained larvikite from the Larvik Plutonic Complex (LPC); B) porphyritic larvikite with a centimetre-scale corridor with strong flow texture. C) medium-grained syenite from the LPC; D) typical lardalite (coarse-grained nepheline syenite) from the LPC with prismatic nepheline crystals; E) medium-grained nepheline syenite with euhedral feldspar and interstitial nepheline; F) mingling zone between fine-grained monzonite and layered monzodiorite with the occurrence of Fe-Ti-P at contact zones between both lithologies; G) coarse-grained monzonite and H) porphyritic monzonite from the Kodal lobe; I) sharp contact zone between syenite and monzonite from the Kodal lobe; J) mingling zone near the Kodal deposit with mingling between fine- and coarse-grained monzonite and medium-grained syenite; K) mingling zone between syenite and monzonite with the accumulation of Fe-Ti-P mineralisation in-between; L) Fe-Ti-P massive mineralisation hosted within monzonite displaying marked flow texture and magmatic folding; M) photomicrograph of pyroxene-rich portions of massive Fe-Ti-P mineralisation of the Kodal deposit; N) photomicrograph of pyroxene-poor portions of massive Fe-Ti-P mineralisation of the Kodal deposit, displaying a typical nelsonite; and O) medium-grained quartz-bearing syenite with miarolitic cavities. This lithology cuts the Kodal deposit at its western termination. Abbreviations: Ap – apatite; Bt – biotite; Cpx – clinopyroxene; Fsp – feldspar; Ilm – ilmenite; Mt – magnetite; Nph – nepheline; Qtz- quartz. Figure from Mansur et al., submitted.

The latter include 1 mm, rounded olivine, subhedral 2-5 mm augite, ilmenite, titanomagnetite and subhedral apatite. Zircon appears as an anhedral, late-crystallizing phase. Towards the centre of the intrusion, the lardalite becomes more porphyritic and contains more mafic minerals forming a medium-grained matrix. Samples from the LPC are alkalic and plot at the border between peraluminous and peralkaline (Fig. 2B-C). Nepheline syenite refers to a nepheline syenite with a sub-trachytic texture (Fig. 3E) where lath-shaped perthitic alkali feldspars are euhedral 5 to 7 mm long and define the matrix of the rock.

They can be randomly oriented or aligned. Nepheline is subhedral to interstitial, locally altered into zeolite. It can be abundant and reach up to 30 modal % around Anundsjøen (Schjølberg 2023; chapter 3.3.4). Locally, sodalite forms oikocrysts or anhedral crystals. Mafic minerals consist of subhedral to interstitial aegirine, biotite and titanite. Pyrochlore, zircon and apatite are accessory minerals. All samples are alkalic, plot in the metaluminous field (Fig. 2C) and display a steep REE pattern characterized by an enrichment in LREE (Light Rare Earth Elements; Fig. 2D).

Although the Si-saturated and undersaturated portions of the LPC, i.e. rings VIII and IX respectively, display different lithologies, the occurrence of Fe-Ti-P-rich rocks at their contact zone is relatively common. These rocks are fine-grained accumulations of Fe-oxides (Ti-magnetite and ilmenite) and apatite, with variable proportions of augite, olivine, biotite and accessory monazite, zircon and titanite (Fig. 3F). For simplicity, we refer herein to these rocks as Fe-Ti-P mineralisation. This does not imply any economic significance but refers to the accumulations of Fe-Ti-P-rich minerals. The Fe-Ti-P mineralisation are mostly associated with contact zones between different lithologies, displaying mingling features, and commonly associated with the occurrence of slightly more primitive rocks such as fine-grained monzodiorite (Fig. 3F).

3.1.2 Kodal lobe

The region referred to as the Kodal lobe was first described by Buelens and co-authors (2024) based on the 1:100,000 Oslo Rift geologic map from the Geological Survey of Norway and comprises a series of oval-shaped intrusions extending southwards from the Kodal deposit for around 15 km in length and 5 km in width (Fig. 1), originally within ring V of the LPC (e.g. Rämö et al. 2022). Overall, the shape of the lobe suggests that it intruded the ring V from the LPC, whereas it is intersected by the nepheline syenite from ring X, providing some temporal constraints relative to surrounding intrusions. The Kodal lobe is dominated by a coarse- to

medium-grained monzonite (Fig. 3G) with similar petrographic characteristics to the larvikite from the LPC. Moreover, the monzonites locally display a gradual transition from a coarse-grained to a porphyritic texture with progressively more fine-grained matrix interstitial to large (i.e. 3 to 10 cm) rhomb-shape ternary feldspar (Fig. 3H). The second-most common lithology of the Kodal lobe is a medium-grained syenite with euhedral alkali-feldspar and minor clinopyroxene and accessory biotite, Fe-oxides and apatite.

3.1.3 Kodal area

The Kodal area is used to indicate the rocks at the immediate vicinity of the Kodal deposit - i.e. within 1 km of the Kodal ore body (Fig. 1). The host rock of the Kodal deposit is a medium- to coarse-grained monzonite petrographically similar to the monzonite found within the Kodal lobe. Nevertheless, in the vicinity of the Kodal deposit, it displays significant variation in grain size. The monzonite displays centimetre-thick and relatively round pockets that are fine-grained. Moreover, relatively rounded, centimetre-scale patches of coarse-grained biotite-bearing syenite are also observed and suggest mingling between syenite and monzonite in the vicinity of the Kodal deposit. In some cases, centimetre-scale patches of Fe-Ti-P mineralisation, with similar petrographic characteristics as those described for the LPC, are observed at the contact between monzonite and syenite. Overall, the rocks of the Kodal area are petrographically similar to the rest of the Kodal lobe but display more complex textural relationships with common mingling textures and grain-size variations. The zones that display mingling textures are commonly marked by the presence of patches of Fe-Ti-P mineralisation (Fig. 3K)

The Kodal deposit, the main Fe-Ti-P mineralisation in the Kodal area, is poorly exposed in the field; however, some textural relationships can be observed (detailed description of the deposit can be found in chapters 3.3 and 3.4). The Fe-Ti-P mineralisation occurs as centimetre-scale domains of apatite, Fe-oxides and clinopyroxene accumulation within the monzonite (Fig. 3L-O).

3.1.4 Rimstad intrusion

The Rimstad intrusion occurs immediately west of the Kodal area and defines a relatively circular structure approximately 10 km in diameter comprising concentric intrusions of syenite at the centre, surrounded by monzonite and an outermost syenite to quartz-bearing syenite body (Fig. 1 and 2).

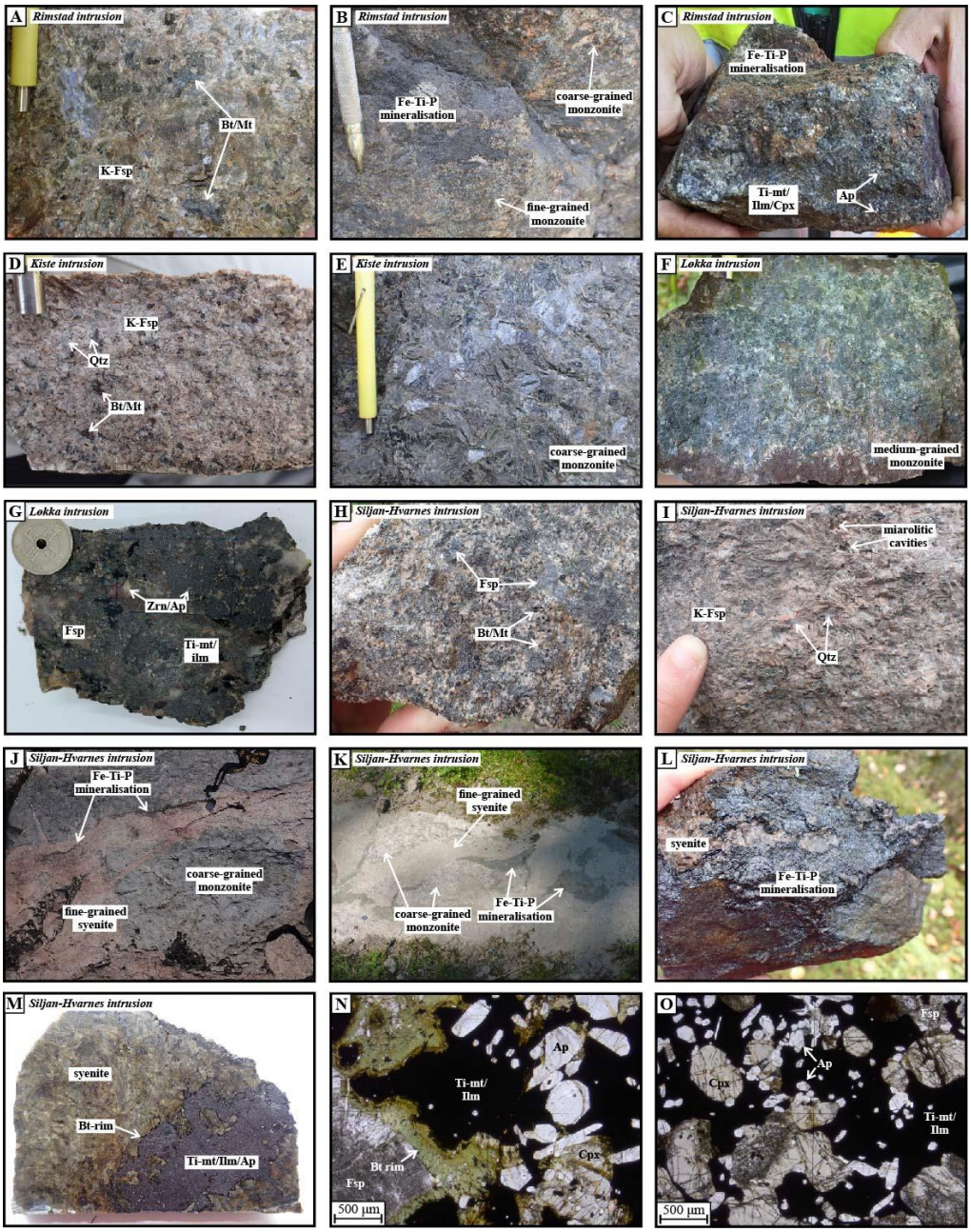

Figure 4: Field and textural observations. A) Medium-grained syenite from the Rimstad intrusion; B) mingling zone between coarse- and fine-grained monzonite and the accumulation of Fe-Ti-P mineralisation in-between; C) detail of the massive Fe-Ti-P mineralisation of the Rimstad intrusion; representative D) medium-grained quartz-bearing syenite; and E) coarse-grained monzonite from the Kiste intrusion; F) medium-grained monzonite from the Løkka intrusion; and G) associated massive Fe-Ti-P mineralisation with abundant zircon; H) porphyritic monzonite; and I) quartz-syenite with miarolitic cavities from the Siljan-Hvarnes intrusion; J) and K) mingling zones between fine-grained syenite and coarse-grained monzonite with the accumulation of Fe-Ti-P mineralisation at the contact between both lithologies; L) detail of massive Fe-Ti-P mineralisation hosted within medium-grained syenite from the Siljan-Hvarnes intrusion; M) detail of the thin biotite-rich reactional rim developed at the sharp contact between massive Fe-Ti-P mineralisation and host syenite. Note the absence of Fe-rich minerals in the host syenite; N) photomicrograph showing the detail of biotite reactional rim between syenite feldspar crystals and the Fe-Ti-P mineralisation; O) photomicrograph of typical Fe-Ti-P mineralisation of the Siljan-Hvarnes intrusion with fine-grained apatite and medium-grained clinopyroxene (augite), Ti-magnetite and ilmenite. Abbreviations: Ap – apatite; Bt – biotite; Cpx – clinopyroxene; Fsp – feldspar; Ilm – ilmenite; Mt – magnetite; Nph – nepheline; Qtz- quartz; Zrn – zircon. Figure from Mansur et al., submitted.

Monzonite of the Rimstad intrusion, like the one from the LPC, is dominated by large, subhedral, zoned rhombohedral alkali feldspars, containing cores of plagioclase. Mafic minerals are mostly restricted to the rim of the large alkali feldspars, except for 10-100 µm-scale augite, magnetite and rare apatite. The order of appearance of mafic minerals is subrounded olivine, subhedral augite and late interstitial to poikilitic brown reddish biotite or brown amphibole. Apatite is present as inclusions in all mafic phases and rims of alkali feldspars. The syenite is medium- to coarse grained and composed of euhedral alkaline feldspar (Fig. 4A), and subhedral green aegirine locally rimmed by dark blueish green richterite surrounded by a matrix enriched in magnetite and biotite. Accessory phases are titanomagnetite and ilmenite, locally containing inclusions of hematite, apatite, zircon and late interstitial carbonates.

The monzonite varies from coarse- to fine-grained with the occurrence of both grain sizes together, displaying a lobate contact. Like that observed at other localities, the occurrence of fine-grained Fe-Ti-P mineralisation is typical in mingling zones (Fig. 4B). The Fe-Ti-P mineralisation is dominated by fine-grained Fe-oxides, apatite and clinopyroxene (Fig. 4C), displaying a sharp contact with the host rocks. Monzonite and syenites from the Rimstad intrusion are alkalic, enriched in LREE compared to HREE (Heavy Rare Earth Elements) and display Eu anomalies close to 1 (Fig. 2).

3.1.5 Kiste intrusion

The Kiste intrusion is located west of the Rimstad intrusion, with a semi-circular structure dominated by quartz-monzonite (Fig. 2) with small, elongate monzonite lenses (Fig. 1). The quartz-monzonite is medium-grained with subhedral to euhedral perthitic alkali feldspar crystals and interstitial quartz, euhedral blue-green amphibole and titanite (Fig. 4D). Subhedral magnetite, ilmenite, apatite and zircon are accessory phases. In one sample bright green aegirine is interstitial and locally rims the amphibole. Coarse-grained monzonite is characterised by large subhedral plagioclase and mesoperthitic alkali feldspar with minor interstitial biotite, magnetite and apatite (Fig. 4E). Locally, the proportion of biotite in both syenite and monzonite reaches up to 15 vol. %, which is accompanied by the appearance of millimetre-scale miarolitic cavities. Quartz monzonites from the Kiste intrusion are alkalic and metaluminous. They display a slight negative Eu anomaly and like most intrusive rocks in the region are strongly enriched in LREE (Fig. 2).

3.1.6 Løkka intrusion

The Løkka intrusion is located southwest of the Kiste intrusion and displays a similar semi-circular shape with the southern portion dominated by monzonite and the northern portion comprising mainly syenite (Fig. 1 and 2). The syenite is typically medium-grained, although grain-size variations are common, with subhedral to euhedral alkali-feldspar crystals, euhedral to subhedral aegirine augite, interstitial biotite, and minor apatite, interstitial quartz and titanomagnetite. The monzonite varies from medium- to coarse-grained and is characterised by subhedral plagioclase and alkali feldspar with augite and late interstitial biotite (Fig. 4E). Near the contact with B1 basalts (Figure 1), the monzonite displays several grain-size variations ranging from fine- to coarse-grained, which is accompanied by the occurrence of centimetre-scale pegmatitic REE-Zr-Nb-rich pockets. These tend to be medium- to coarse-grained with apatite and Fe-oxides associated with feldspars. In the northern portion of the contact, the syenite becomes coarser grained to pegmatitic and rich in mafic minerals. These pegmatites, enriched in Nb, Zr and REE are described in more detail in chapter 3.2.3. (Fig. 3G).

3.1.7 Siljan-Hvarnes intrusion

The Siljan-Hvarnes intrusion consists of an approximately 20 km-long and 3-5 km-wide series of monzonite and syenitic intrusions nested into each other with an overall east-west elongation (Fig. 1). Although much textural variation is observed, the typical monzonite is medium- to coarse-grained with subhedral to euhedral plagioclase and alkali-feldspar occurring together with clinopyroxene and minor biotite, magnetite and apatite, similar to other intrusions. A common textural variation is the occurrence of large rhomb-shaped ternary feldspar phenocrysts within a medium- to fine-grained matrix, yielding a porphyritic texture (Fig. 4H). The most typical syenite comprises medium-grained euhedral alkali feldspar with interstitial biotite, and locally quartz (Fig. 4I), normally associated with small miarolitic cavities (Fig. 4I). Most of the Fe-Ti-P mineralisations observed in the intrusion occur in a similar context as described for other intrusions, associated with mingling zones between lithologies displaying grain-size variations (Fig. 3J and chapter 3.3.1). For instance, at contact zones between fine-grained syenite and coarse-grained monzonite, the local accumulation of Fe-Ti-P mineralisation is common (Fig. 4J and 4K). Although the mineralisation may be very local, in some cases Fe-oxides, apatite and clinopyroxene accumulate into relatively larger domains (e.g. Fig. 4K), and eventually lead to the formation of massive ores (Fig. 4L; see chapter 3.3.1 for further details). In such cases, the massive domains comprise Fe-oxides, apatite and augite displaying a sharp contact with the alkali feldspar from the host syenite, bordered by a millimetre-thick biotite rim

(Fig. 4M). Overall, the mineralogy of the Fe-Ti-P mineralisation from the Siljan-Hvarnes intrusion is like that of the Kodal deposit ores, but with slightly less abundant apatite (Fig. 4N). The variation of nelsonite to pyroxene-rich domains is also observed (e.g. Fig. 4O). All rocks, from monzodiorite to quartz-monzonite plot around 1 in the ASI diagram (Fig. 2C). The REE concentration decreases with differentiation. All the lithologies display a strong enrichment in LREE but the REE pattern of quartz monzonite flattens out towards the HREE.

3.1.8 Skrim intrusion

The Skrim intrusion is located north of the Siljan-Hvarnes intrusion defining a rounded structure approximately 20-25 km in diameter which vary between monzonite to granite. Samples of monzonite are typically medium-grained with euhedral plagioclase and alkali feldspar, minor interstitial biotite, augite, inverted pigeonite, ilmenite, magnetite and disseminated fine-grained pyrite. Granite from this intrusion consist of subhedral quartz phenocrysts, tabular perthitic alkali feldspars, interstitial aegirine, and subhedral blue-green amphibole. Fluorite and zircon are the main accessory phases. All samples are peraluminous, except the granite which falls into the metaluminous field (Fig. 2C). Monzonite and syenite both display a steep REE pattern related to a strong enrichment in LREE. The granite, while as enriched in LREE as the two other lithologies is also strongly enriched in HREE (70 times chondrite).

3.2 U-Pb geochronology and Hf isotopes in Zircon

In order to better understand the temporal evolution of the intrusions in the studied area we have analysed U-Pb and Hf isotopes in zircons recovered from 34 samples, covering all the intrusions. The zircons analysed were commonly recovered as fragments of larger crystals, but smaller grains commonly display a prismatic shape, except in the lardalite where zircons are subhedral, interstitial and the last phase to crystallize.

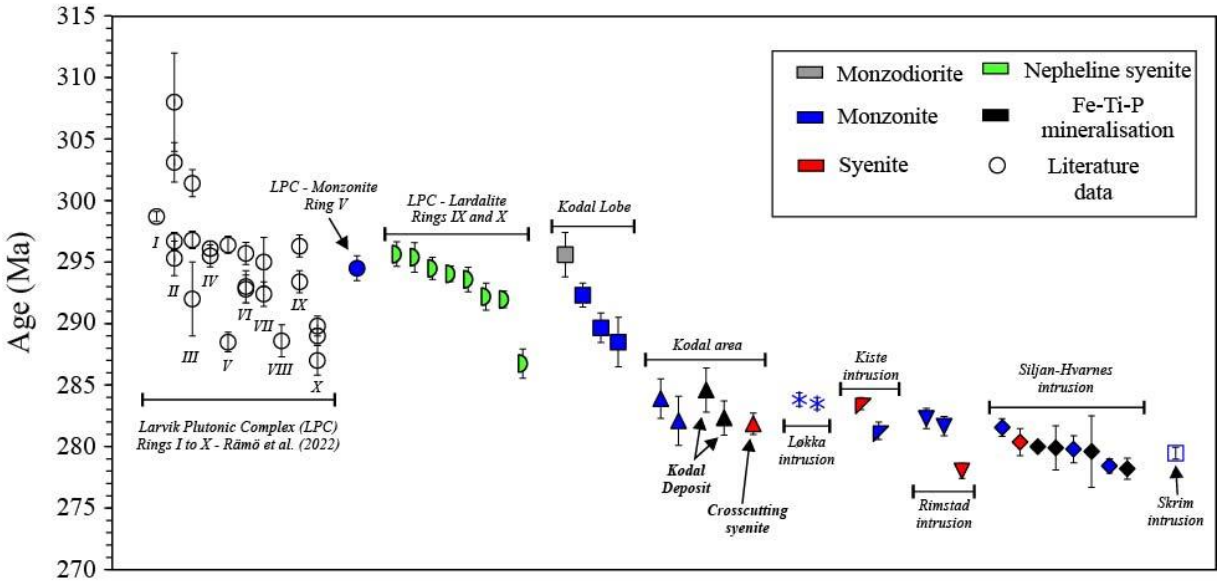

Figure 5: Summary of ages and uncertainties for samples from this study and available in literature (Rämö et al., 2022) for different intrusions. The samples are organised from left to right following progressively younger ages for each intrusion. Figure from Mansur et al., submitted.

Table 1 contains a summary of the results, whereas figures 5 and 6 display the results for U-Pb and Hf isotopes, respectively.

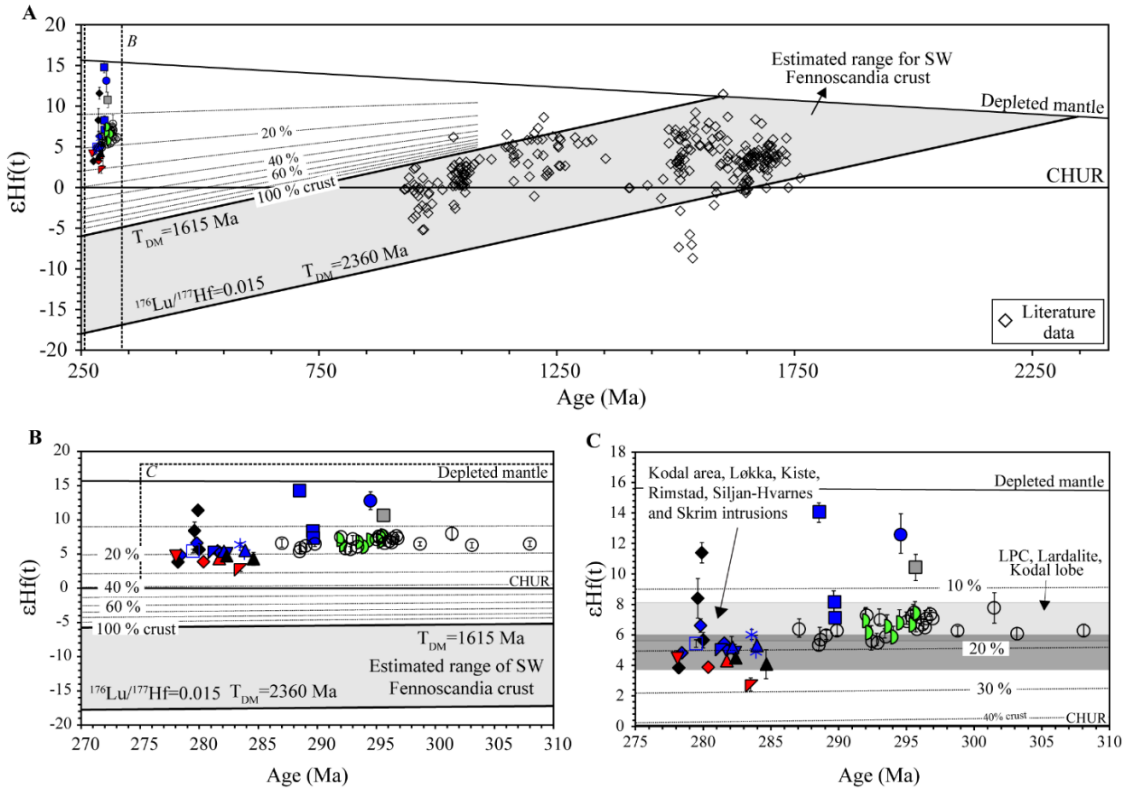

Figure 6: In-situ zircon Hf data from this study. A) Data plotted as εHf(t) versus magmatic age. Literature data is from Slagstad and co-authors (2024) and used to estimate a compositional field for SW Fennoscandia crust. Mixing lines between estimated crust and depleted mantle are plotted with 10 to 20% increments. See text for full explanation. B) and C) detail over samples from this study and literature data from Rämö et al. (2022). Figure from Mansur et al., submitted.

To allow for a better spatial visualisation of the results, figure 7 shows the ages obtained for the samples around the LPC, Kodal lobe and Kodal area, whereas figure 8 displays the ages for samples from the intrusions located northwest of the Kodal deposit.

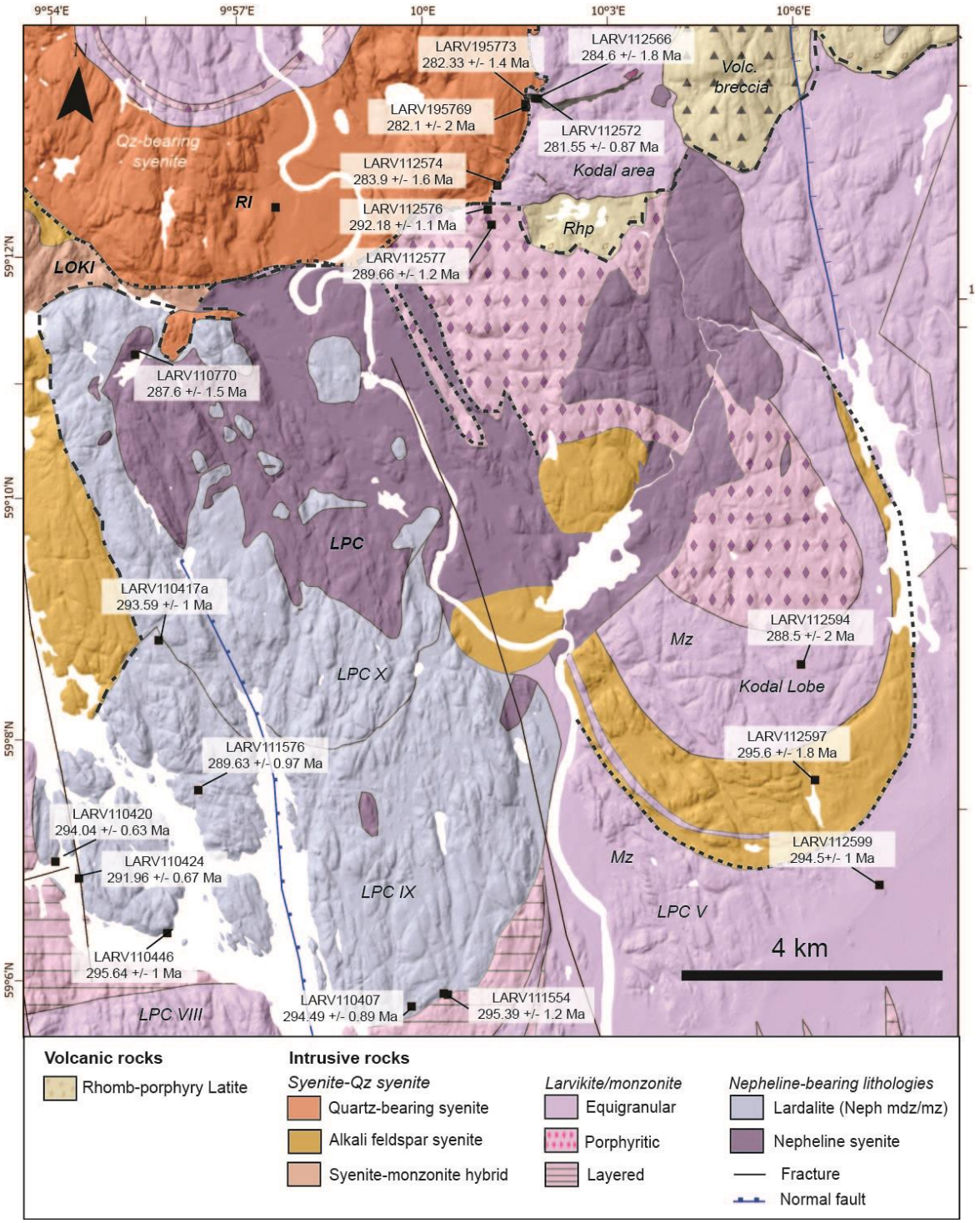

Figure 7: Detailed geologic map over Larvik Plutonic Complex (LPC), Kodal lobe and Kodal area with ages obtained for different samples. Figure from Mansur et al., submitted.

Overall, the intrusions can be divided into two groups comprising the older (295 to 288 Ma) LPC, and the younger (284 to 278 Ma), Kiste, Løkka, Rimstad, Siljan-Hvarnes and Skrim intrusions. Although most rocks from the Kodal lobe yield a similar crystallisation age to the LPC (i.e. older), those from the Kodal Fe-Ti-P deposit and its hosts yield crystallisation ages that belong to the younger group. Therefore, a cogenetic relationship between the Kodal deposit and the LPC is not supported. Older intrusions have higher εHft values (from +8 to +5.5) relative to younger intrusions (from +6 to +3.5). Such difference could be attributed to slight variations in mantle source, differing amounts of crustal assimilation, or variable contaminants.

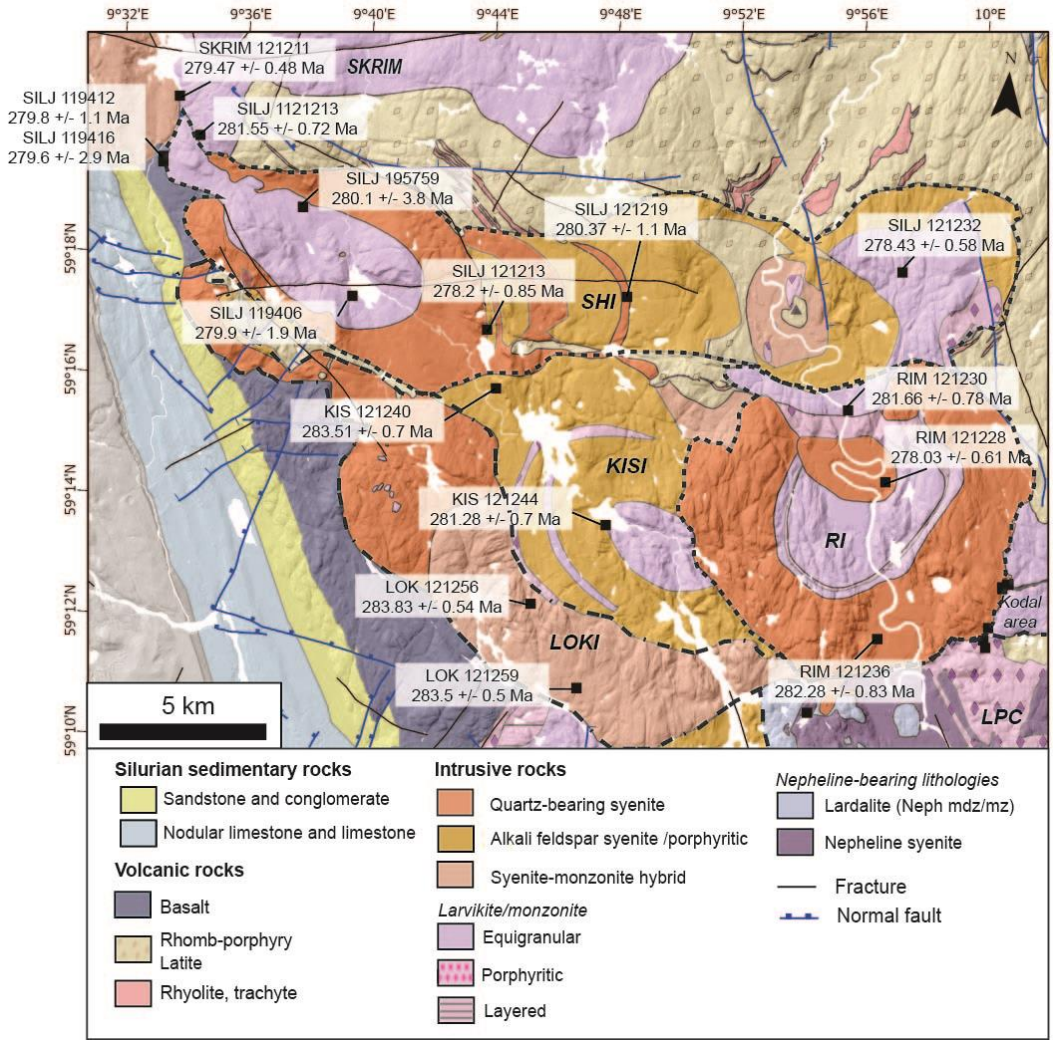

Figure 8: Detailed geologic map over Løkka, Rimstad, Kiste, Siljan-Hvarnes and Skrim intrusions with ages obtained for different samples. Figure from Mansur et al., submitted.

These results are consistent with previous isotopic studies conducted in the area (Buelens et al. 2024; Neumann et al. 1988). Information related to the isotopic analyses have been submitted for peer-review publication and will soon be available to all (Mansur et al. submitted).

Table 1: summary of sample description, zircon U-Pb and Hf isotopic data from this study

Sample	Locality	Classification	Age (Ma)	Average εHf	N	Description
LARV-112599	Larvik Plutonic Complex - Ring V	Monzonite (Larvikite)	294.5 ± 1	12.8 ± 1.3	12	Medium-grained monzonite with 1-2cm iridescent feldspar crystals and interstitial mafic agglomerates (around 20%) comprising subhedral olivine, diopside and minor titanomagnetite, ilmenite, pyrite and apatite. Biotite and brown hornblende are interstitial and form rims or poikilitic crystals around the mafic agglomerates.
LARV-110446	Larvik Plutonic Complex - Ring IX	Lardalite	295.6 ± 1	7.7 ± 0.5	11	Coarse grained nepheline monzonite with 3-4cm nepheline and feldspar euhedral crystals and interstitial finer-grained matrix composed of subhedral feldspar, nepheline, diopside, titanomagnetite, ilmenite and apatite. Brown biotite and amphibole are poikilitic. Zircon are large and interstitial.
LARV-111554	Larvik Plutonic Complex - Ring IX	Fe-Ti-P mineralisation	295.4 ± 1.2	6.9 ± 0.5	9	Medium grained nepheline monzonite with 1-2 cm nepheline and feldspar euhedral crystals in a melanocratic finer-grained matrix containing olivine, diospide, titanomagnetite, ilmenite and apatite, with only minor feldspar and nepheline.
LARV-110407	Larvik Plutonic Complex - Ring IX	Lardalite	294.5 ± 0.9	7 ± 0.6	12	Coarse grained nephline syenite with 3-4cm nepheline and rhomb-shaped feldspar euhedral crystals, poikilitic biotite and brown amphibole. Diopside is subhedral to anhedral. Magnetite and apatite are accessory phases. Local very fine-grained zircon and titanite aglomerates.
LARV-110420	Larvik Plutonic Complex - Ring IX	Lardalite	294 ± 0.6	6.1 ± 0.5	12	Chilled margin at the conctact between larvikite and lardalite. Porphyritic texture with 1-2 cm large euhedral alkali feldspar with nepheline exsolution in a matrix of subhedral olivine, nepheline and anhedral diopside. Apatite, titanomagnetite and ilmenite are scattered in the matrix.
LARV-110417a	Larvik Plutonic Complex - Ring IX	Lardalite	293.6 ± 1	6.8 ± 0.5	11	Porphyritic nepheline monzodiorite with rhomb-shaped feldspar phenocrysts and subhedral nepheline, in a matrix of subhedral olivine, nepheline and anhedral diopside. Apatite, titanomagnetite and ilmenite are scattered in the matrix, while biotite forms late poikilitic crystals.
LARV-111576	Larvik Plutonic Complex - Ring IX	Lardalite	292.2 ± 0.9	6.4 ± 0.5	10	Porphyritic nepheline monzonite with 2-5cm nepheline and feldspar euhedral crystals within a finer-grained matrix of nepheline, feldspar, olivine, diopside with minor biotite, magnetite and apatite.
LARV-110424	Larvik Plutonic Complex - Ring IX	Lardalite	292 ± 0.7	7.1 ± 0.6	9	Porphyritic nepheline monzonite with 3-5cm nepheline and feldspar euhedral crystals within a fine-grained matrix composed of feldspar, nepheline, diopside, olivine,titanomagnetite, ilmenite, late poikilitic biotite and apatite.
LARV-110770	Larvik Plutonic Complex - Ring X	Lardalite	287.6 ± 1.5	6.3 ± 0.5	11	Porphyritic nepheline monzodiorite with 1-2 cm feldspar euhedral crystals within a finer-grained matrix of interstitial nepheline, feldspar and diopside with abundant secondary biotite. Titanomagnetite, ilmenite and apatite are accessory phases.
LARV-112597	Kodal Lobe	Monzodiorite	295.6 ± 1.8	10.7 ± 0.8	10	Fine-grained olivine augite monzodiorite ~~a~~ssociated with the syenite from the Kodal lobe. Plagiocalse is the main feldspar, biotite and brown hornblende are poikilitic, while titanomagnetite and ilmenite are both present.
LARV-112576	Kodal Lobe	Monzonite	290.2 ± 1.0	8.4 ± 0.5	10	Coarse-grained monzonite with 3-4cm iridescent feldspar crystals. Mafic minerals (20%) comprise cm- large subhedral diopside associated with biotite, magnetite, apatite. and secondary titanite rimming titanomagnetite.
LARV-112577	Kodal Lobe	Monzonite	289.7 ± 1.2	7.3 ± 0.6	11	Porphyritic monzonite with 1-4cm feldspar crystals within a medium- to fine-grained matrix of alkali feldspar, biotite, minor augite, zircon, hemo-ilmenite, magnetite and titanite.

Table 1: continued

Sample	Locality	Classification	Age (Ma)	Average εHf	N	Description
LARV-112594	Kodal Lobe	Monzonite	288.5 ± 2	14.3 ± 0.6	13	Medium-grained monzonite with 1-2cm feldspar crystals and interstitial mafic agglomerates (around 10-15%) comprising biotite, diopside, minor titanomagnetite, ilmenite, apatite and titanite.
LARV-112574	Kodal area	Monzonite	283.2 ± 1.7	5.5 ± 0.5	10	Coarse-grained monzonite with 3-4cm euhedral feldspar crystals. Remnent diopside is associated with subhedral magnetite and minor green hornblende. The sample was affected by late fluids. Secondary minerals include epidote, sericite, white micas, biotite and titanite.
LARV-195769	Kodal area	Monzonite	282 ± 2	5.4 ± 0.5	12	Coarse-grained monzonite with 3-4cm euhedral feldspar crystals and fine-grained (around 10%) biotite, magnetite and diopside agglomerates. The feldspar crystals display a thin pinkish rim.
LARV-112566	Kodal area	Fe-Ti-P mineralisation	284.6 ± 1.8	4.3 ± 0.9	12	Fine-grained Fe-Ti-P-rich rock crossed by a 3mm-wide vein of nelsonite. Subhedral diopside, Ti-magnetite, ilmenite and subeuhedral to anhedral apatite with subordinated biotite are tha main mineral phases present.
LARV-195773	Kodal area	Fe-Ti-P mineralisation	282.3 ± 1.4	4.7 ± 0.6	10	Medium-grained nelsonite with euhedral to subeuhedral Ti-magnetite and ilmenite and subeuhedral to anhedral apatite associated with diopside and minor feldspar.
LARV-112572	Kodal area	Quartz syenite	281.8 ± 0.9	4.6 ± 0.4	10	Medium-grained quartz-bearing syenite with 1-2 cm sericitized K-feldspar and interstitial (10%) quartz, biotite and magnetite.
LOK-121256	Løkka intrusion	Monzonite	283.8 ± 0.8	5.1 ± 0.2	12	Coarse-grained quartz-bearing monzonite with 2-4cm euhedral alkali feldspar crystals and fine- to medium grained biotite, titanomagnetite and altered augite. Apatite is acicular.
LOK-121259	Løkka intrusion	Monzonite	283.5 ± 0.5	6.3 ± 0.3	15	Medium-grained monzonite with 1-2cm subhedral feldspar, aegirine augite and interstitial biotite. Titanomagnetite, ilmenite, titanite, zirconolite and apatite are accessory phases.
KIS-121240	Kiste intrusion	Quartz syenite	283.5 ± 0.7	2.9 ± 0.4	13	Medium-grained quartz-bearing syenite with 1-2 cm euhedral K-feldspar and interstitial (10%) quartz, euhedreal blue-green richterite, titanite, biotite, ilmenite and magnetite.
KIS-121244	Kiste intrusion	Monzonite	281.3 ± 0.7	5.2 ± 0.3	14	Medium-grained monzonite with 1-2cm subhedral alkali feldspar, subhedral augite locally rimmed by brown green amphibole. Titanomagnetite, biotite and apatite are accessory phases.
RIM-121236	Rimstad intrusion	Quartz syenite	282.3 ± 0.8	5.1 ± 0.3	12	Medium-grained quartz-bearing syenite with 1-2 cm K-feldspar and interstitial (10%) quartz, biotite and minor magnetite.
RIM-121230	Rimstad intrusion	Monzonite	281.7 ± 0.8	5.2 ± 0.3	13	Medium-grained monzonite with 1-2cm subhedral zoned feldspar in a finer grained matrix composed of augite, altered olivine, titanomagnetite, apatite. Biotite is interstitial.
RIM-121228	Rimstad intrusion	Quartz-bearing monzonite	278.0 ± 0.6	4.7 ± 0.3	16	Medium-grained quartz-bearing monzonite with 1-2cm subhedral feldspar, augite and interstitial biotite and quartz. The feldspar crystals display a thin pinkish rim.
SILJ-121210	Siljan-Hvarnes intrusion	Quartz-bearing monzonite	281.5 ± 0.7	5.5 ± 0.2	14	Coarse-grained quartz-bearing monzonite with 1-4 cm subhedral to euhedral feldspar crystals and finer- to grained matrix composed of altered feldspar, interstitial biotite, titanomagnetite with minor apatite. Zircon is abundant in the matrix.
SILJ-121219	Siljan-Hvarnes intrusion	Quartz syenite	280.4 ± 1.1	3.9 ± 0.3	17	Medium-grained quartz-bearing syenite with 1-2 cm K-feldspar and interstitial (10-20%) quartz, biotite and magnetite with minor altered mafic minerals.
SILJ-195759	Siljan-Hvarnes intrusion	Fe-Ti-P mineralisation	280.1 ± 3.8	5.7 ± 0.5	12	Fe-Ti-P mineralisation comprising fine-grained subheudral to euhedral Ti-magnetite, ilmenite, clinopyroxene and apatite with local feldspar crystals and minor biotite at contact between feldspar and other minerals.

Table 1: continued

Sample	Locality	Classification	Age (Ma)	Average εHf	N	Description
SILJ-119406	Siljan-Hvarnes intrusion	Fe-Ti-P mineralisation	279.9 ± 1.9	11.4 ± 0.7	12	Fe-Ti-P mineralisation comprising fine-grained subheudral to euhedral Ti-magnetite, ilmenite, clinopyroxene, apatite and biotite with local medium-grained feldspar crystals.
SILJ-119412	Siljan-Hvarnes intrusion	Monzonite	279.8 ± 1.1	6.6 ± 0.4	14	Coarse-grained monzonite with 2-5cm subhedral to euhedral feldspar crystals and fine- to medium grained clinopyroxene and interstitial biotite and magnetite.
SILJ-119416	Siljan-Hvarnes intrusion	Fe-Ti-P mineralisation	279.6 ± 2.9	8.4 ± 1.3	13	Fe-Ti-P mineralisation comprising an association of medium-grained subheudral Ti-magnetite, ilmenite, clinopyroxene and fine-grained apatite with minor biotite.
SILJ-121232	Siljan-Hvarnes intrusion	Monzonite	278.4 ± 0.6	4.8 ± 0.2	10	Porphyritic monzonite with 2-4cm feldspar crystals within a fine-grained matrix of feldspar, biotite and augite. Minor magnetite and apatite within the matrix.
SILJ-121213	Siljan-Hvarnes intrusion	Fe-Zr-REE-rich rock	278.2 ± 0.8	3.8 ± 0.3	11	Fe-Zr-REE-rich rock composed of subhedral to euhedral blue green richterite, green to dark green aegirine, zircon, magnetite, sausuritized feldspar and interstitial quartz. Apatite, cheekinite are accessory phases.
SKRIM-121211	Skrim intrusion	Monzonite	279.5 ± 0.5	5.4 ± 0.2	12	Medium-grained quartz-bearing monzonite with 1-cm subhedral to euhedral zoned alkali feldspar crystals with mesoperthitic cores and perthitic rims, fine- to medium grained augite and interstitial biotite ilmenite and magnetite. Minor disseminated pyrite.

N= Number of analyses

Table 1: Summary of sample description, U-Pb geochronology and Hf isotopes for this study. Table from Mansur et al., submitted."

3.3 Mineralisation

In this chapter we describe the various occurrences associated with the intrusions presented in the previous chapter.

Locality	Intrusion	Type of occurrence
Rånerød	Larvik Plutonic Complex	Fe-Ti-P
Heirøningen	Larvik Plutonic Complex	Fe-Ti-P
Kjose	Larvik Plutonic Complex	Fe-Ti-P
Farris vann	Larvik Plutonic Complex	Nepheline
Anundsjøen	Larvik Plutonic Complex	Nepheline
Kodal I	Kodal area	Fe-Ti-P
Kodal II	Kodal area	Fe-Ti-P
Haukaråsen	Løkka intrusion	REE-Zr-Nb pegmatite
Rønningane	Siljan intrusion	Zr-REE-Nb
Erik's gruve	Siljan intrusion	Fe-Ti-(P)
Jernskottet	Siljan intrusion	Fe-Ti-(P)
Kåsemyrene	Siljan intrusion	Fe-Ti-P and minor Zr-REE-Nb
Flittig	Siljan intrusion	Zr-REE-Nb
Meisholt	Siljan intrusion	Fe-Ti-P and minor Zr-REE-Nb
Teigen	Siljan intrusion	Fe-Ti-P
Hesterønningane	Siljan intrusion	Fe-Ti-P and Zr-REE-Nb

Table 2: summary of the occurrences and deposits considered in this study.

To define what constitutes interesting concentrations, here P, REE, Zr and Nb, we propose to use cut-off values associated with resource estimates from important mineral deposits. These numbers do not give any indication on the volume of the mineralisation nor their economic potential but provide a comparison for the concentration of the elements in the whole-rock analyses. Rocks with more than 4 wt% P_2O_5 contain enough phosphorus to be characterized as ore. This value corresponds to the resource estimate cut-off value in the Siilinjärvi deposit (Finland), as of today the only deposit actively mined for phosphorous in Europe (Decrée et al. 2023). In this deposit, phosphorous is hosted by apatite.

The Niobiec mine in Quebec exploiting the Saint-Honoré carbonatite complex has a cut off at 0.2 wt% Nb_2O_5 (1,400 ppm), where Nb is hosted primarily by Ca-Na pyrochlore and Fe columbite (Tremblay et al. 2015; Niobec 2013). Finally, Norra Karr in Sweden, an alkaline intrusion enriched in HREE, has a cut off at 1.7 wt% ZrO_2 (12,600 ppm) associated with its

resource estimate (Bowell et al. 2021). In the latter intrusion, Zr is hosted in the mineral eudialyte. We consider concentrations close or above these numbers to be large enough to be relevant.

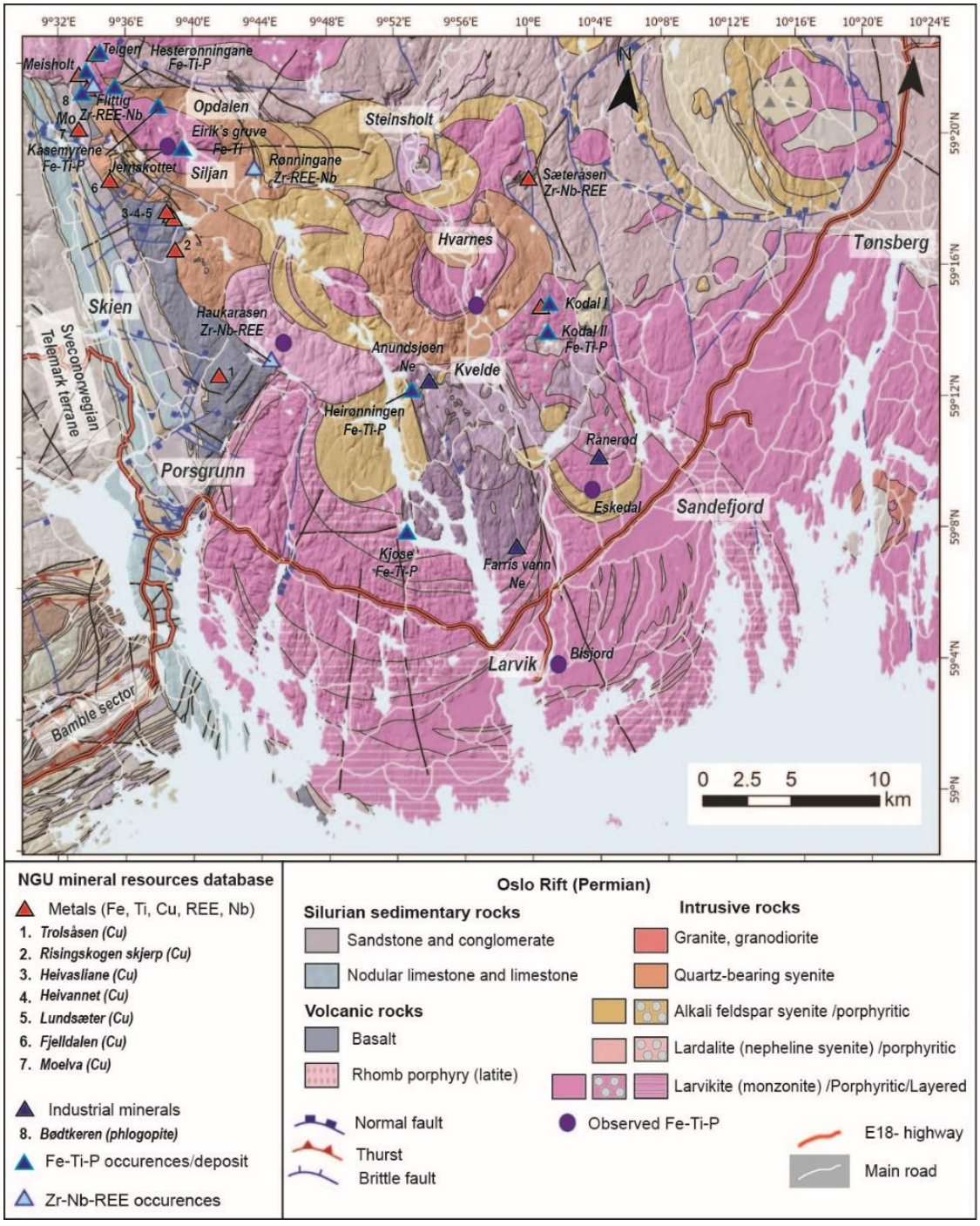

Figure 9: Geologic map of the study area showing the location and the nature of the various occurrences and deposits found in the region (excluding natural stones).

Three types of mineralisations can be separated based on the distribution of the elements in the rocks and their mineralogy: 1) Fe-Ti-P occurrences, 2) Zr-Nb-REE occurrences and 3) Zr-Nb-REE pegmatites. Since they occur in different parts of the intrusive systems and have

different mineral assemblages, we treat them separately. Table 2 summarizes the occurrences and deposits considered in this study. Whole-rock data and microprobe data presented in this chapter are available in appendix A and B respectively. Acquisition methods and instrumentation are described by Coint and co-authors (Coint et al. 2020), and the Kieffer and co-authors (2024) respectively.

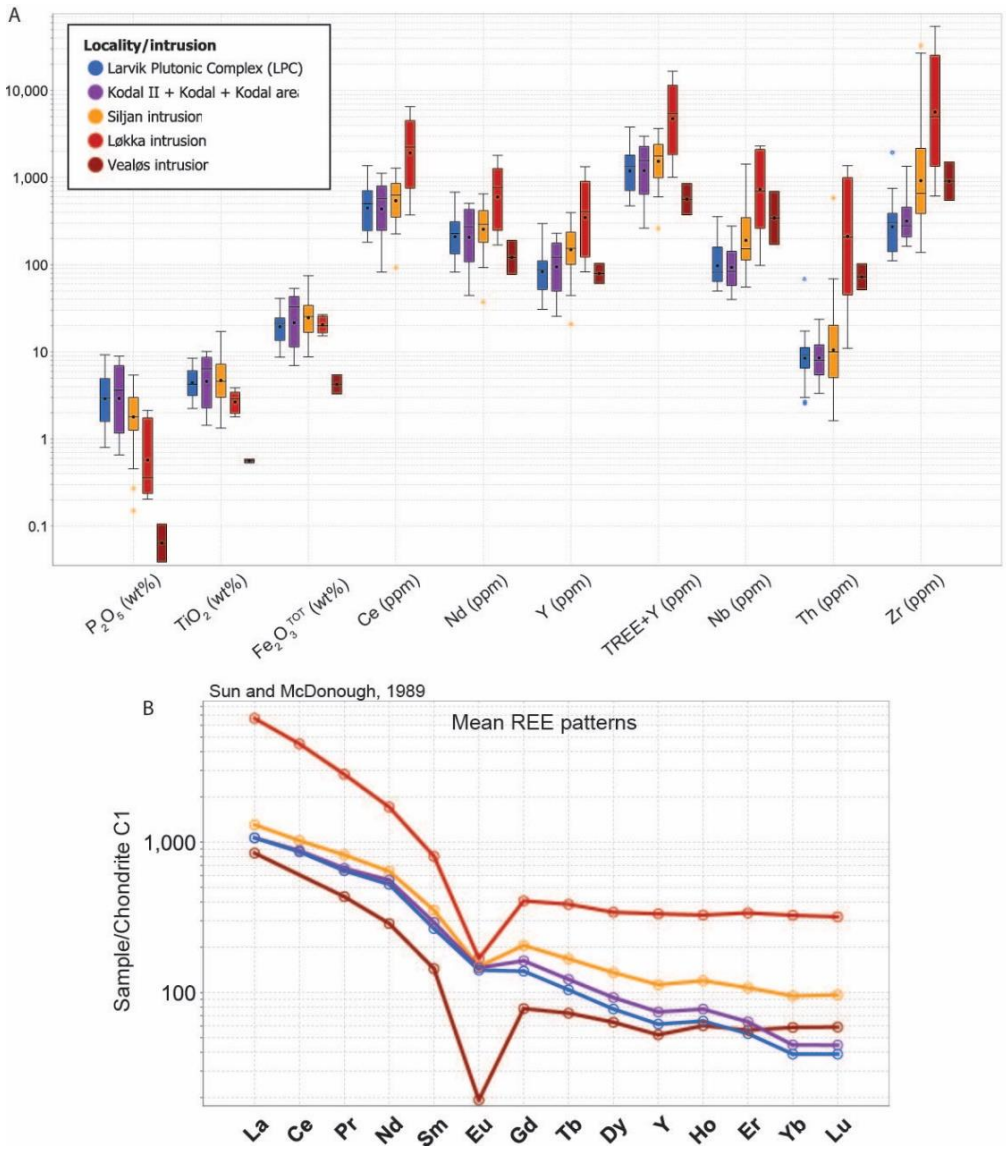

Figure 10: Whole-rock dataset for the various occurrences and deposits of the region sorted by intrusion. A) Box plot for various elements of interest. B) Spider diagrams showing the average REE distribution in ore samples.

The Fe-Ti-P-(REE) occurrences and deposits are hosted by intrusions of mostly monzonitic composition, such as the LPC, the Kodal area and Siljan host (Fig. 1 and 9). Overall, the Siljan intrusion contains mineralisation more enriched in HREE than the ones hosted by the LPC and the Kodal monzonite. The Zr-Nb-REE pegmatites are the most enriched in HFSE,

including Nb, Th and Zr, in addition to REE. The Vealøs granite is depleted in P, Fe, REE but enriched in Th (Fig. 10).

3.3.1 Fe-Ti-P-(REE)

Fe-Ti-P-(REE) occurrences are the most voluminous and the most likely to be the focus of future mineral exploration.

This group includes the main Kodal deposit (Kodal I, in this study- see chapter 3.4.1 for a detailed description), Kodal II (chapter 4.1.4 and 4.3.2), several occurrences in the Siljan intrusion (Teigen, Meisholt), including the Kåsemyrene occurrence and occurrences in the Larvik Plutonic Complex (Heirønningen and Kjose) (Fig. 9). Fe-Ti-P rich-rocks are present in several other areas, notably in the Larvik Plutonic Complex. Apatite is the main REE-bearing phase in these occurrences. While we recorded the presence of these rocks, we chose not to report all of them in the database as some of the occurrences are marginal or contain low concentration of phosphorous. Nevertheless, we have analysed some of the minerals from these localities to compare with the larger occurrences ("Observed Fe-Ti-P" in figure 9).

We subdivided the Fe-Ti-P mineralisation group in three sub-groups based on their chemical composition as mineral proportions can vary widely from one occurrence to the other.

3.3.1.1 Fe-Ti-P in monzodiorite

Rånerød is a small body of Fe-Ti-P-rich monzodiorite hosted in the Larvik Plutonic Complex which can be mapped over a few hundreds of meters. The rock displays a millimetre-thick weak layering defined by higher modal concentrations of mafic minerals. In this occurrence, apatite and Fe-Ti oxides are not restricted to veins and pods but occur scattered throughout the rock with other magmatic minerals such as feldspar, pyroxene and olivine. Although the P_2O_5 content is not particularly high (2.3-2.8 wt% P_2O_5; Fig. 12), apatite is distributed homogeneously throughout the unit.

3.3.1.2 Fe-Ti-P mineralisation in monzonite

Fe-Ti-P-rich rocks occur as decimetres to 15-30 m wide lenses of disseminated or massive ore (Fig. 11A-E). The contact between the monzonite and the massive ore can be sharp or gradational over cm to tens of meters.

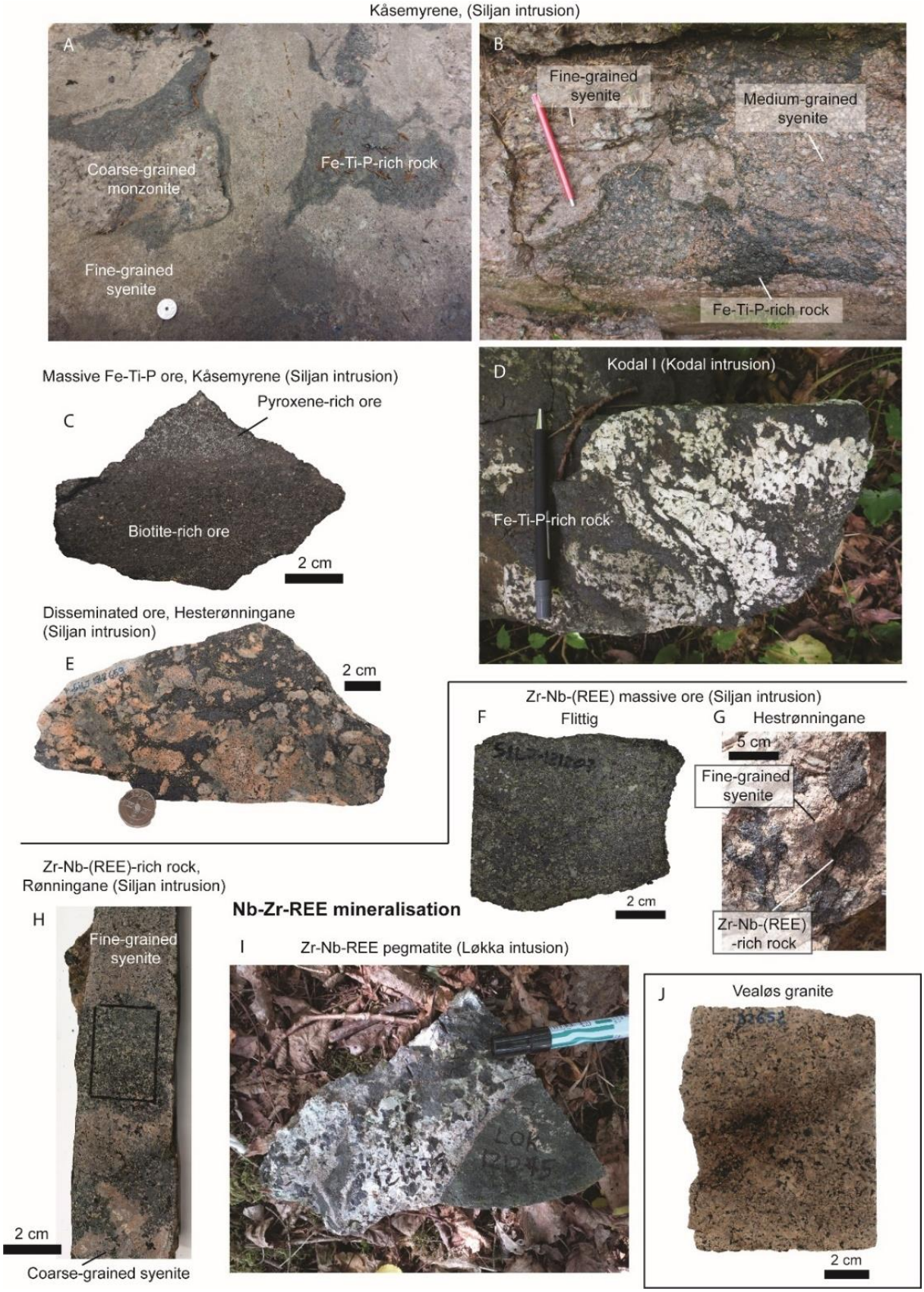

Figure 11: Mineralized rocks in the field. A-B, D-E) Evidence for mingling between two (or more) different monzonite/syenite magma batches and the occurrence of Fe-Ti-P-rich rocks. C) Massive ore from Kåsemyrene. A sharp contact between the biotite- and pyroxene-bearing ore. F-G-H) Massive Zr-Nb-REE ore form cm-scale pods or schlieren in syenite. I) Nb-Zr-REE pegmatite from Haukaråsen. J) Vealøs granite.

In several instances monzodioritic enclaves are observed in the vicinity of the mineralisation, like in Kodal (Fig. 3L and J) or along the Farris Lake in Kjose.

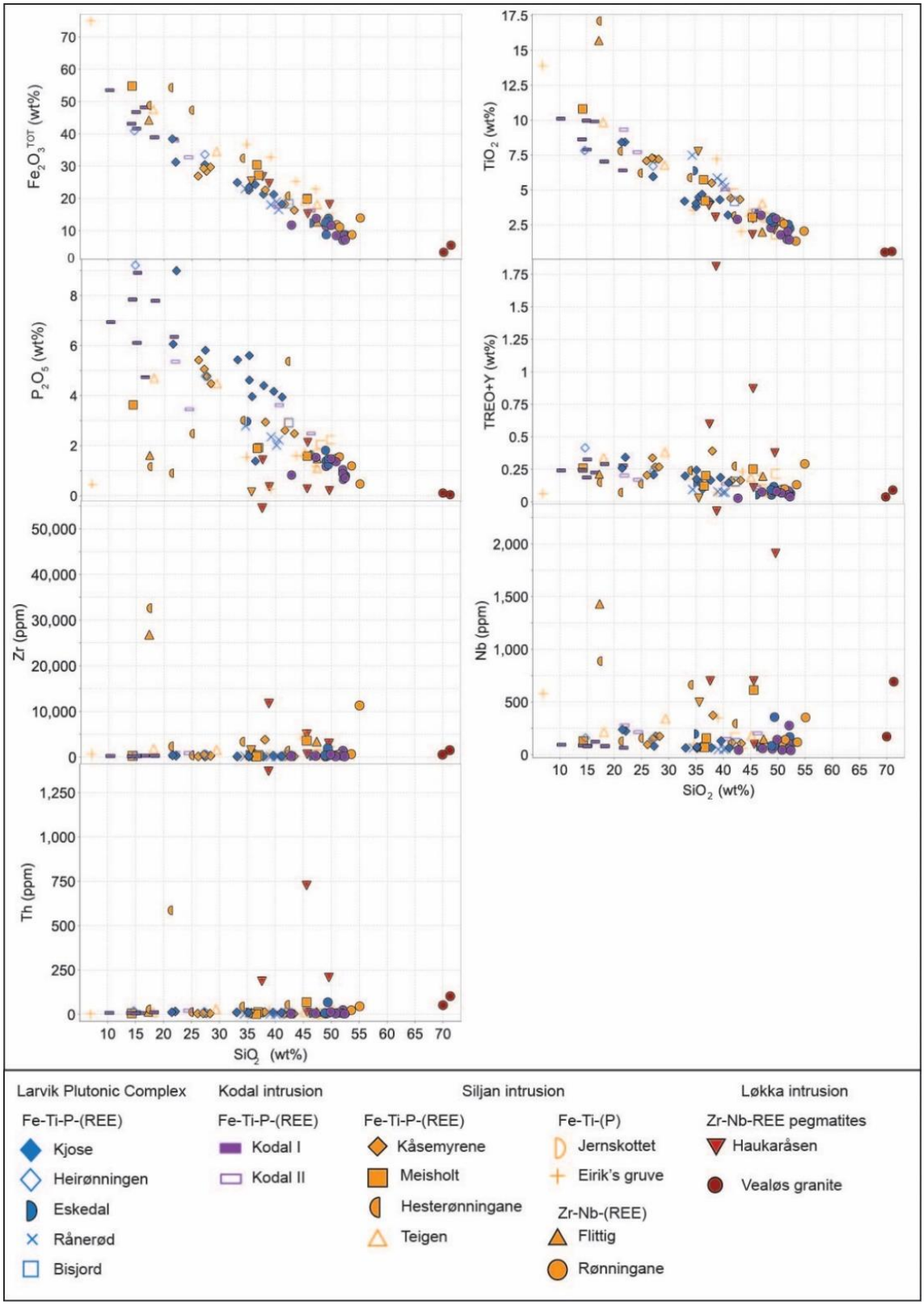

Figure 12: Whole-rock dataset from the occurrences and deposits considered in this study.

Mafic silicates are dominated by clinopyroxene, or more rarely by olivine in the LPC and Teigen occurrence in the Siljan intrusion.

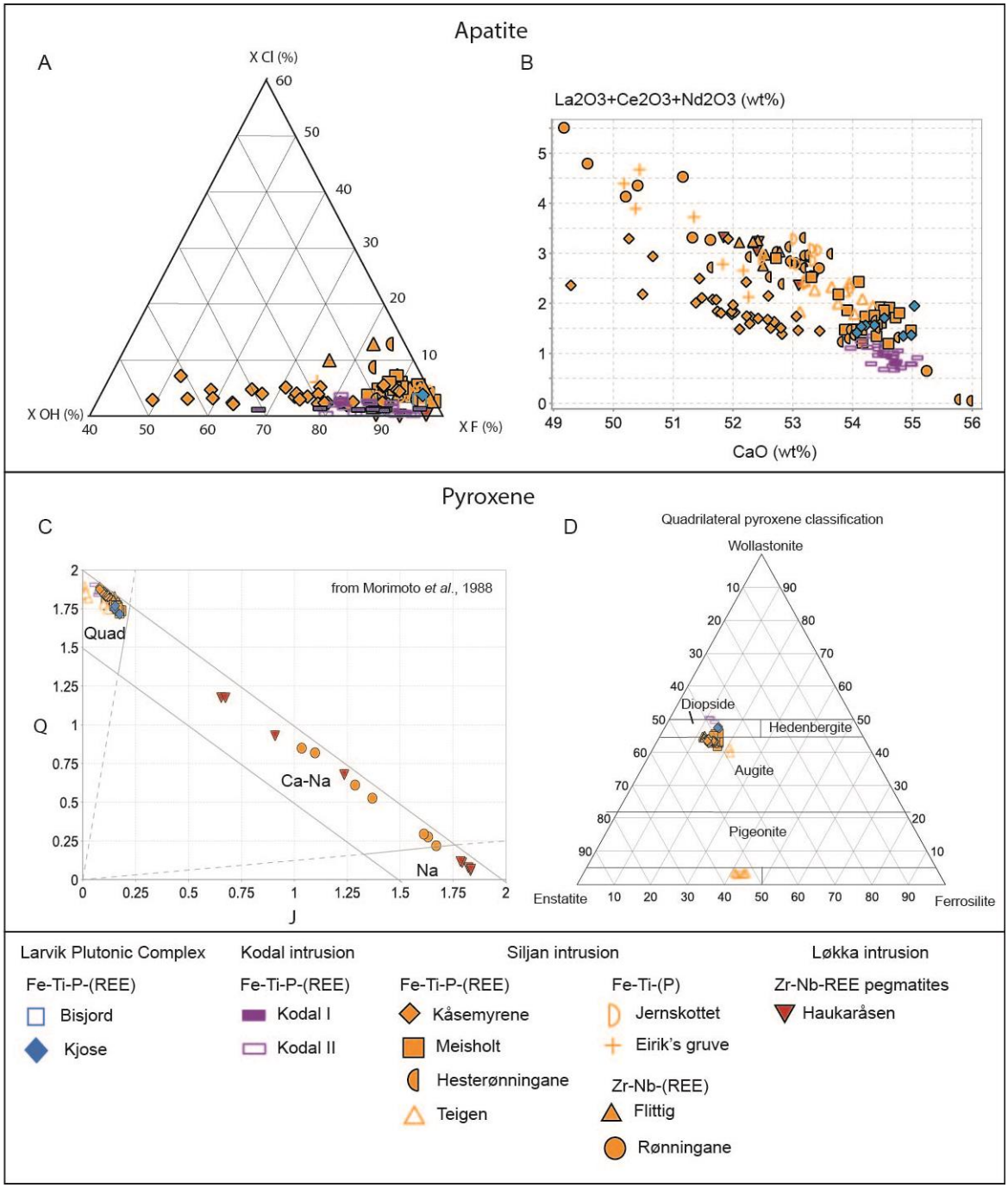

Figure 13: a and b: Major element composition of apatite. c and d: classification diagrams of pyroxene (Morimoto 1988) from the various deposits and occurrences. Q= Ca+Mg+Fe2+, J=Na

Pyroxene in this type of mineralisation consist mainly of diopside or augite (Fig. 13D). In Kåsemyrene, brown Ti-rich pargasite (amphibole) and brown-red phlogopite are locally abundant (Andersen 2021), attesting to the Mg and Ti-rich nature of the magma the ore crystallized from. Orthopyroxene is only stable in the Teigen occurrence.

Both ilmenite and titanomagnetite are present in Fe-Ti-P-rich rocks. Fe-Ti oxides from the Teigen occurrence have a distinct composition. Ilmenite is enriched in Nb (0.87-1.2 wt % Nb_2O_5) and titanomagnetite is enriched in Zn compares to the same Fe-Ti oxides in other Fe-Ti-P occurrences (Appendix B). In all occurrences, apatite is fluorine-rich (fluoroapatite; Fig. 13). Apatite in the Kåsemyrene occurrence have higher hydroxyl component compared to other occurrences.

Rare Earth element concentrations in apatite vary between the different occurrences. Two trends are visible in Fig. 13). Larger occurrences such as at Kodal or Kåsemyrene have apatite less enriched in REE (0.5-3.5 wt%, mostly 1-2 wt% TREO) than smaller occurrences (1.2-3.5 wt%, mostly 2-3.5 wt% TREO).

A possible explanation relates to the limited amount of Rare Earth Element available in a magma, compared to the amount of phosphorous. The concentration of REE in apatite, when the latter is the main REE-bearing phase in the system, depends on the modal amount of apatite crystallizing. The more P is dissolved in the melt, the more apatite will crystallize and the less REE they contain. It is interesting to note though that the amount of REE in apatite vary as a function of the nature of the magma and which intrusion we consider. Iron-Ti-P occurrences associated with the Siljan intrusion contain apatite generally more enriched in REE than occurrences in the Larvik Plutonic Complex and Kodal area, although there is some overlap between the datasets (Fig. 12).

This observation is consistent with the lithologies in the Siljan-Hvarnes intrusion being more differentiated than in the LPC (Fig. 2).

3.3.1.3 Fe-Ti-(P) mineralisation

The Eirik's gruve and Jernskottet occurrences from the Siljan intrusion (Fig. 9) will also be considered in this chapter, although they do not contain much apatite (0.45-0.47 wt% P2O5). Magnetite and ilmenite, or hemo-ilmenite in the case of Jernskottet, are depleted in magnesium and vanadium but enriched in zinc suggesting that they formed from a more evolved magma than common Fe-Ti-P-rich rocks. Apatite in these samples is rare but strongly enriched in REE (2.1-4.67 wt% TREO, Fig. 13B) compared to apatite in other occurrences.

3.3.2 Zr-Nb-(REE) mineralisation

The Zr-Nb-REE occurrences found exposed at the surface vary from meter- to 15-m large bodies. Samples from Flyttig, one from Hesterønningane (Siljan intrusion) and Håkarausen

(Løkka intrusion) reach concentrations of Zr and Nb in the same order of magnitude as the cut-off values for Zr- and Nb ore deposits (Fig. 12). Although occurrences reported in this study represent small volumes and are therefore not economical at the moment, their presence indicates that the processes forming rocks anomalously enriched in HFSE occurred in the region. It is therefore possible that these types of mineralisation can form larger deposits.

Zr-Nb-(REE) mineralisation in Flittig and Hesterønningane are hosted in syenite, close to the contact of B1 basalt or large xenoliths of B1 basalts. They vary from cm to decimetre scale-veins or pods composed of massive ore (Fig. 11F and G). Zircon, Fe-Ti oxides (hemo-ilmenite in Flyttig and Hestrønningane), diopside, and Ti-rich biotite are the main minerals. Zirconolite occurs as late interstitial films which have crystallized late. Niobium is mainly hosted in the hemo-ilmenite or ilmenite which contain between 0.5-0.8 wt% Nb_2O_5 and zirconolite, although our present investigation does not allow to eliminate other potential Nb-rich minerals.

The sample from Rønningane is found in a mingling zone between a fine-grained and coarse-grained syenite (Fig. 11H). The rock is enriched in zirconium but contains less niobium compared to the previously described locality. The mineral assemblage consists of blue-green aegirine-augite (Fig. 13C), amphibole (richterite), alkali feldspar, interstitial quartz, zircon, titanite and apatite which attest to high activity of Na and F, but not enough to transition into mineral assemblage characteristic of agpaitic magmas (Marks et al. 2011). The rock present evidence of hydrothermal alteration. Nb-rich titanium oxide is a secondary mineral. Apatite in this occurrence is strongly enriched in REE (>3 wt% TREO) (Fig. 13B) and locally altered into monazite. Unlike in the two other localities, the zircon-rich rock contains 55 wt% SiO_2 and is quartz-bearing, attesting to the silica oversaturated nature of the magma.

In addition to these occurrences, zircon-rich rocks have also been observed in the cores from the main Kodal deposit (Kodal I) where they are hosted by the quartz-bearing syenite. They can occur in the vicinity of the contact with the massive Fe-Ti-P-(REE) mineralisation. In Kåsemyrene, they were sampled along the riverbank, where the syenite in the north mingles with the monzonite and fine-grained syenite. These occurrences are therefore rather common but remain small in all cases.

3.3.3 Zr-Nb-REE pegmatites

This group is composed of a single occurrence (Haukaråsen, Løkken intrusion; Fig. 9 and 11I) consisting of Zr-Nb-REE-rich pegmatitic rocks. Samples from this locality are the most

enriched in HFSE of all the occurrences we have encountered (Fig. 12; 0.1 %<TREO<1.6 %, 600 ppm<Zr<1.6 %, 100 ppm<Nb<0.23% and 11 ppm<Th<1370 ppm). The relationship between the contact with the B1 basalt, found in the vicinity (a few tens of meters away), the syenite and the mineralized pegmatite remains unclear. Detailed mapping of the area is needed to bring more context to the presence of these rocks. Unlike the pegmatite related to the LPC where mineral assemblages of typical of agpaitic magmas have been recorded (Andersen et al. 2013; Marks et al. 2011; Andersen et al. 2010), the Haukarausen pegmatitic rocks have a miaskitic assemblage where most of the HFSE elements (Zr, Ti, Nb) sit in common minerals such as zircon and titanite.

The mineralogy in these rocks is complex and it is beyond the scope of this report to dive into the structure of Zr-Ti-Nb-REE bearing minerals. Furthermore, low totals obtained for some of the microprobe analyses, indicate that important elements have not been analysed, limiting the mineral identification. However, these data can be used to assess the distribution of the elements and whether they sit in silicates, phosphates or oxides, important information for mineral processing. Zirconium and titanium are hosted in minerals such as zircon ($ZrSiO_4$) and titanite ($CaTiSiO_5$), although zirconolite ($(Ca,Ce)Zr(Ti,Nb,Fe^{3+})_2O_7$) is present (Appendix B). Niobium is primarily hosted by a Ti-rich Nb-Ca-Ti-Na-F oxide (45.5-48 wt% Nb_2O_5 and 1.5-1.9 wt% Ta_2O_5), likely belonging to the pyrochlore family ($(Na,Ca)_2Nb_2O_6(OH,F)$. These minerals also contain 2.6-2.9 wt% ThO_2 and 1.7-3.1 % UO_2. Rare Earth Elements are mostly distributed between a mineral from the britholite family $(Ce,Ca,Th,La,Nd)_5(SiO_4,PO_4)_3(OH,F)$ and chevkinite $(Ce,La,Ca,Th)_4(Fe^{2+},Mg)_2(Ti,Fe^{3+})_3Si_4O_{22}$, and contain 41 to 47 wt% TREO wt%. The absence of complex Zr-silicates indicate that the magma did not reach agpaitic composition despite the stability of sodium-iron-amphibole and fluorite which indicates high activities of sodium and fluor in the melt.

3.3.4 Nepheline

Nepheline is a mineral which contains high concentrations of aluminium and alkaline elements (sodium and potassium) compared to feldspars. It is used as a flux in the ceramic industry to lower the melting point of glass. In 2023, feldspar and nepheline joined the list of Critical Raw Materials (https://single-market-economy.ec.europa.eu/sectors/raw-materials/areas-specific-interest/critical-raw-materials_en). One active mine exists in Norway and is located on the island of Stjernøy (https://www.sibelco.com/en), in Northern Norway. There nepheline syenite is extracted and the feldspar nepheline concentrate shipped to the rest of the world.

High quality Nepheline-feldspar concentrates are characterized by high concentrations of alkaline elements and low Fe-contents (Table 3).

Oxides	Requirement (wt%)	Farrisvann ideal separate			Anundsjøen ideal separate		
		Nph-Fsp 50/50	Nph-Fsp 40/60	Nph-Fsp 30/70	Nph-Fsp 50/50	Nph-Fsp 40/60	Nph-Fsp 30/70
Fe_2O_3	<0.1	0.29	0.26	0.22	0.49	0.42	0.36
Al_2O_3	>23	27.30	25.84	24.38	25.14	23.85	22.56
Na_2O+K_2O	>14	16.00	15.39	14.79	17.69	16.98	16.26

Table 3: Requirement for nepheline, feldspar separate for the glass industry (McLemore et al. 2006) and calculation of ideal nepheline-feldspar separated from the two occurrences. Calculations and microprobe data for nepheline are available in appendix B.

The production of dark/amber glass or fiberglass are not as restrictive on the Fe-content and allows for Fe_2O_3 concentrations up to 0.35 wt%.

The Larvik Plutonic Complex hosts two occurrences of nepheline, both assessed by Norsk Hydro in the 1970's. The first one is related to the intrusive unit IX (Petersen 1978; Fig. 1) and consist of very coarse-grained nepheline monzodiorite, whereas the second one is hosted by the nepheline syenite cropping out in the area of Kvelde (Fig. 9).

3.3.4.1 Farrisvann occurence

The occurrence consists of very coarse-grained nepheline monzonite to syenite (Fig. 3D) where euhedral crystals of nepheline vary from 1 to 4 cm. According to Norsk Hydro, the modal content of nepheline reaches 35-40% along the contact with the intrusive unit VIII of the LPC (Petersen 1978) and decreases towards the north to reach 15-20 % (Fig. 14)

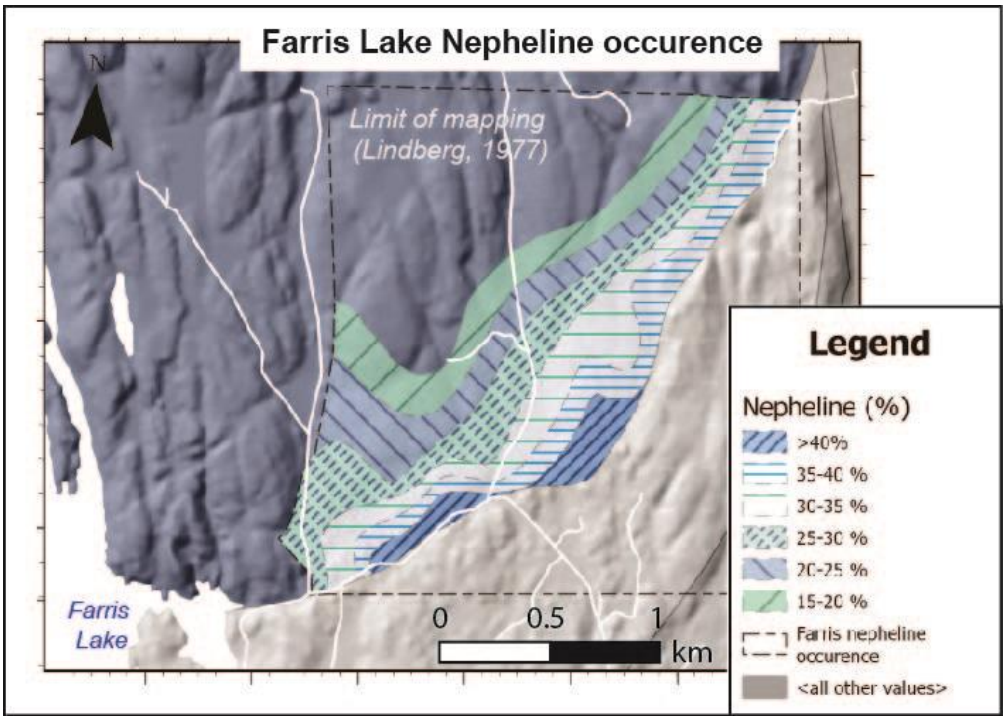

Figure 14: Farrisvann (Farris Lake) nepheline occurrence.

We calculated the composition of a potential pure mineral concentrate, assuming that feldspar and nepheline could be separated from the rest of the minerals (Table 3). We varied the proportions between feldspar and nepheline to reflect the variations encountered in the occurrence, assuming a perfect separation of feldspar and nepheline from other phases during mineral processing. Results show that in the case of the Farrisvann occurrence, nepheline is rich in iron (an average of 0.47 wt% FeO^{tot}) but still meets the requirement for the amber glass industry. Aluminium and alkali contents (Na_2O+K_2O) fulfil the requirements.

3.3.4.2 Anundsjøen occurrence

At the Anundsjøen occurrence (Fig. 9), the rock consists of a medium-grained nepheline syenite where nepheline is interstitial (Fig. 3E). Locally, the rock displays a trachytic texture, where the needle-shaped alkali feldspar crystals are oriented in the same direction, recording paleo flow within the magma chamber. The occurrence was mapped by Norsk Hydro in the late 1970's (Lindberg 1977). They concluded that the nepheline was too iron rich to be interesting. We reach the same conclusion using the microprobe dataset from M. Schjølberg's Master thesis (2023) (Table 3), as nepheline is even more enriched in iron than the one from Farrivann (0.79 wt% FeO^{tot}). Furthermore, the calculated artificial separate from Anundsjøen is less enriched in aluminium than the one from Farrisvann and reach concentration of Al_2O_3 below requirement when the proportion of nepheline decreases below 30 % in the separate.

We therefore conclude that the nepheline associated with the LPC is too rich in iron to be interesting for the glass industry.

3.4 Petrogenesis

Processes behind the formation of mineralisation control both the chemistry of the minerals forming ore deposits and their geometries, including their volume. Understanding the formation of ore deposits is therefore a crucial aspect of mineral exploration.

Iron-Ti oxide and apatite-rich rocks (i.e. nelsonites) of magmatic origin are commonly associated with mafic and intermediate intrusive complexes related to anorthosite–mangerite–charnockite–granite (AMCG) and layered intrusions (Coint et al. 2023; Coint et al. 2020; Charlier et al. 2008; Dymek and Owens 2001). Nevertheless, the origin of these non-cotectic rocks has been widely debated and petrogenetic models evoking fractional crystallisation, liquid-liquid immiscibility, mineral accumulation and residual melts concentrated by filter pressing have been proposed as alternatives to explain their origin (Emslie 1975; Philpotts 1967).

Discovered in the late eighteen hundreds, the Kodal deposit is one of the largest Fe-Ti oxide and apatite deposits in Norway, with a total indicated resource of 14.6 Mt at 5.18% P_2O_5 and 24.12% Fe (Kodal Minerals PLC 2017) (Figure 9 and 16). Unlike known occurrences hosted within AMCG suites and mafic layered intrusions, the Fe-Ti oxide and apatite mineralisation at Kodal is hosted within alkaline monzonite. Three distinct models have been proposed to explain the genesis of the Kodal deposit: (i) silicate-liquid immiscibility leading to the separation of an Fe-rich melt (Kragh and Jensen 1991; Bergstøl 1972) (ii) fractional crystallisation and physical accumulation of apatite and Fe-Ti-oxides from a monzonitic magma (Petersen 1978; Lindberg 1985); and (iii) apatite and Fe-Ti oxide crystallisation at depth followed by upward transport, accompanied by mineral sorting, to shallow crustal levels (Andersen and Seiersten 1994).

In this chapter, we report results of fieldwork, petrographic descriptions of the host-rocks and Fe-Ti-P ores and composition (major and minor elements) of Fe-Ti oxides and apatite to constrain the main processes that led to the formation of the Kodal deposit. The findings offer important insights into the genesis of unusual Fe-Ti-P-(REE) but also Zr-Nb-REE

mineralisation in alkaline magmatic systems. Finally, we discuss the processes behind the formation of the nepheline occurrences.

3.4.1 Formation of Fe-Ti-P mineralisation

3.4.1.1 The Kodal ore deposit: geological and geochemical description

The ore body at Kodal comprises E-W trending lenticular shaped zone. It is approximately 2 km long and 100 m thick, undeformed, and dips sub-vertically towards south (Fig. 15).

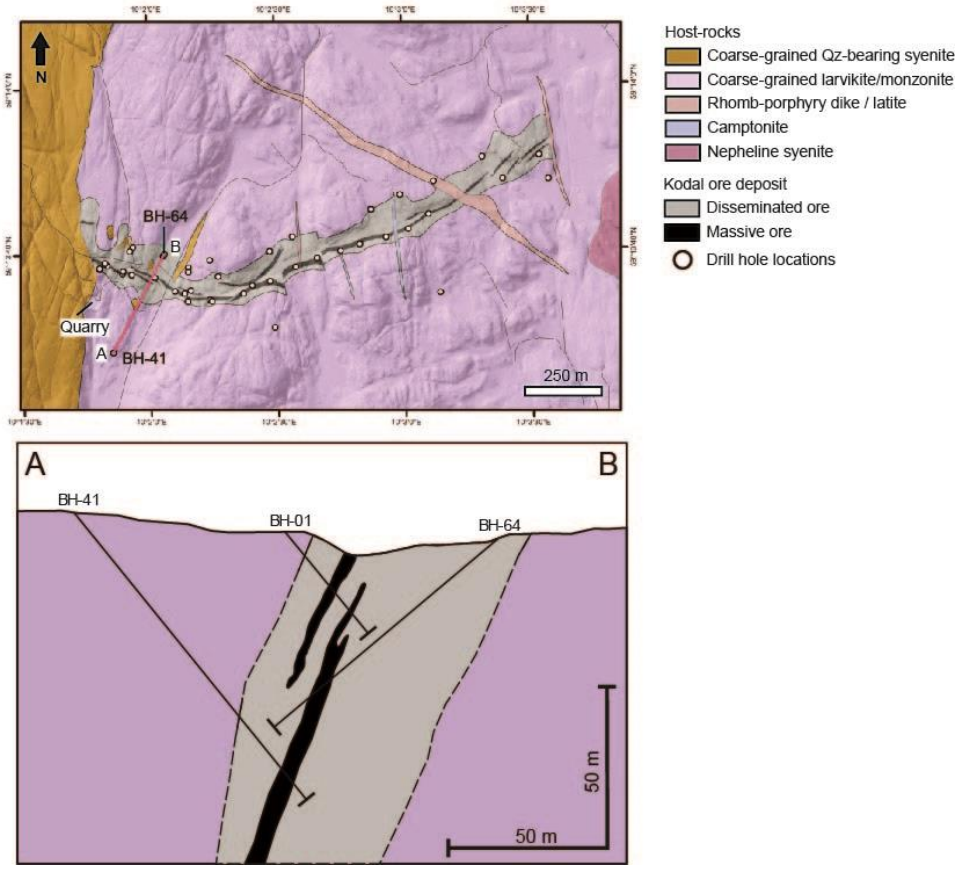

Figure 15: Geologic map of the Kodal area, and the cross section of the Kodal Fe-Ti-P deposit.

It is hosted within coarse-grained monzonite and cut by a quartz-bearing syenite to the west (Fig. 15). The monzonite is predominantly composed of grey to beige ternary feldspars (up to 90 vol.%) associated with aggregates of interstitial fine-grained mafic minerals (Fe-Ti oxides, apatite and clinopyroxene, and minor amphibole and biotite) (<10 vol.%) (Fig. 16A). It is dominantly massive but locally aligned feldspars are observed, which indicate flow texture (Fig. 16A-B). Recent U-Pb dating has shown ages at 283.9 ± 1.6 Ma and 282 ± 2 Ma for the monzonite (Mansur et al. submitted).

The pink coarse- to medium-grained syenite consists of alkali feldspar with minor interstitial quartz, biotite and/or amphibole, and magnetite (Fig. 16C). Miarolitic cavities are commonly present.

On the west side of the Kodal deposit, at the contact between the monzonite and syenite, mingling textures where the syenite 'infiltrates' the monzonite are commonly found. Often, at the contact between these two phases, centimetre accumulation of Fe-Ti oxides and apatite is found (Fig. 16D). In addition to the host monzonite and quartz-bearing syenite, a fine-grained monzodiorite is observed either with enclaves/pieces of the coarse-grained monzonite or in contact with pockets of massive Fe-Ti-P mineralisation. The fine-grained monzodiorite is mainly composed of feldspar, locally porphyritic (Fig. 16E), clinopyroxene and titanomagnetite, and minor apatite and ilmenite.

The Fe-Ti-P ore consists mainly of massive lenses, varying in thickness from a few centimetres to 3 m, composed of Fe-Ti oxides (titanomagnetite and ilmenite), apatite and variable amount of clinopyroxene, enveloped by a transitional zone formed of disseminated and patchy ores. In the transitional zone, the disseminated ore is characterized by Fe-Ti oxides, apatite and clinopyroxene aggregates forming a connected interstitial network around the feldspar phenocrysts (Fig. 16F). Locally, a greater proportion of the interstitial mafic minerals relative to feldspar led to the development of a net-textured ore. In those cases, the mafic minerals define an interstitial continuum within large feldspar crystals, often aligned, and their volume can reach up to 40%. The patchy ore consists of widely distributed centimetric lenses and irregularly shaped pods of massive ore displaying sharp contact with disseminated ore and/or monzonite (Fig. 16G).

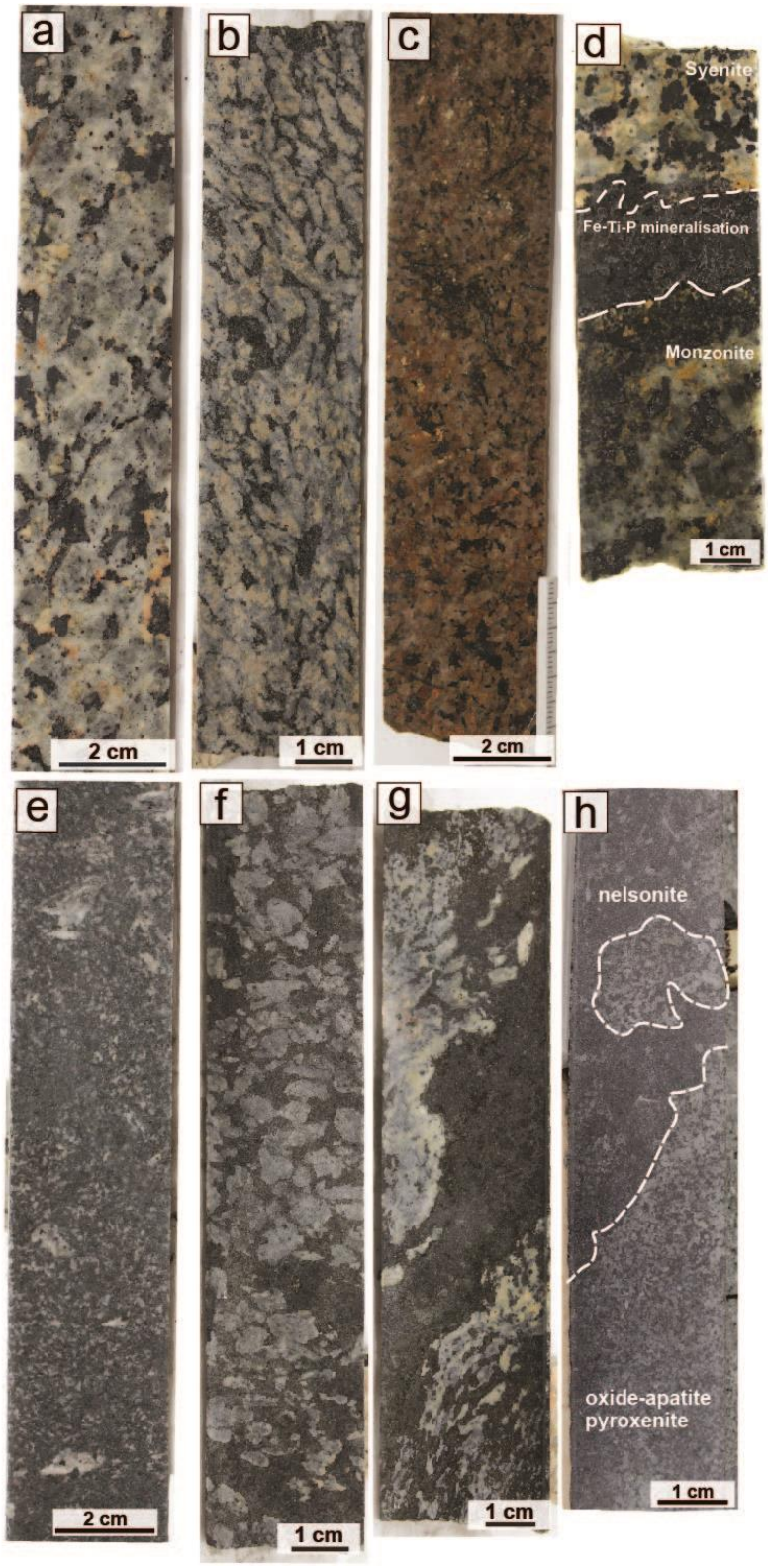

Figure 16: Photographs of representative lithologies of the Kodal Fe-Ti-P deposit. A-B. Coarse-grained monzonite with interstitial Fe-Ti oxides, apatite and clinopyroxene. C. Medium-grained syenite. D. contact between the syenite and monzonite. Not the accumulation of Fe-Ti oxides, apatite and clinopyroxene minerals in the contact of both rocks. E. Fine-grained monzodiorite. F. Disseminated ore characterized by Fe-Ti oxides, apatite and clinopyroxene aggregates forming a connected interstitial network around the feldspar phenocrysts. G. Patchy ore displaying sharp contact with disseminated ore and/or monzonite. H. Massive Fe-Ti-P ore with nelsonite and oxide-apatite pyroxenite and augite-poor domains. Note the sharp contact between both facies, and the occurrence of irregular blebs of the oxide-apatite pyroxenite ore within nelsonite domains.

The lenses of massive ore can be divided into clinopyroxene-poor (i.e., nelsonite) and clinopyroxene-rich domains (i.e., oxide-apatite pyroxenite) (Fig. 16H), the latter being dominant. The nelsonite domains contain approximately 65% in vol. of Fe-Ti oxides and 35% in vol. of fine apatite grains. The diopside-rich portions have 70% in vol of diopside and 30% in vol of Fe-Ti oxides and apatite. The contact between the oxide-apatite pyroxenite and nelsonite is commonly sharp (Fig. 16H). Similar to the monzonite host rock, U-Pb zircon ages of the massive ore range from 284.6 ± 1.8 Ma to 282.33 ± 1.4 Ma (Mansur et al. submitted).

The occurrence of Fe-Ti oxides, apatite and clinopyroxene was classified following their texture and host rock. As aforementioned, Fe-Ti oxides and apatite occur in monzonite, monzodiorite, nelsonite and oxide-apatite pyroxenite, whereas clinopyroxene occurs in all rock types apart from nelsonite.

In the monzonite host rock Fe-Ti oxides, apatite and clinopyroxene occur mostly interstitially, comprising up to 10% of the vol (Fig. 17A-B). Ternary feldspars composing around 90% of the rock, display light grey to beige-white colour and vary from medium- to coarse-grained. Titanomagnetite occurs as masses, rarely euhedral, and displays ilmenite lamellae exsolutions (Fig. 17C). Besides of exsolutions, ilmenite occurs mostly as irregular grains often associated with titanomagnetite (Fig. 17C). Overall, titanomagnetite is more abundant than ilmenite. Apatite crystals occur as inclusions in titanomagnetite and clinopyroxene, but also as euhedral crystals with well-defined contacts with other phases. Clinopyroxene varies from medium- to coarse-grained, is commonly rounded to irregular of shape and displays slight alteration along the fractures and rims to amphibole/biotite (Fig. 17B). Commonly, fine-grained biotite occurs at the contact between titanomagnetite and ternary feldspars, in which the biotite lamellas are oriented perpendicular to the contact (Fig. 17D).

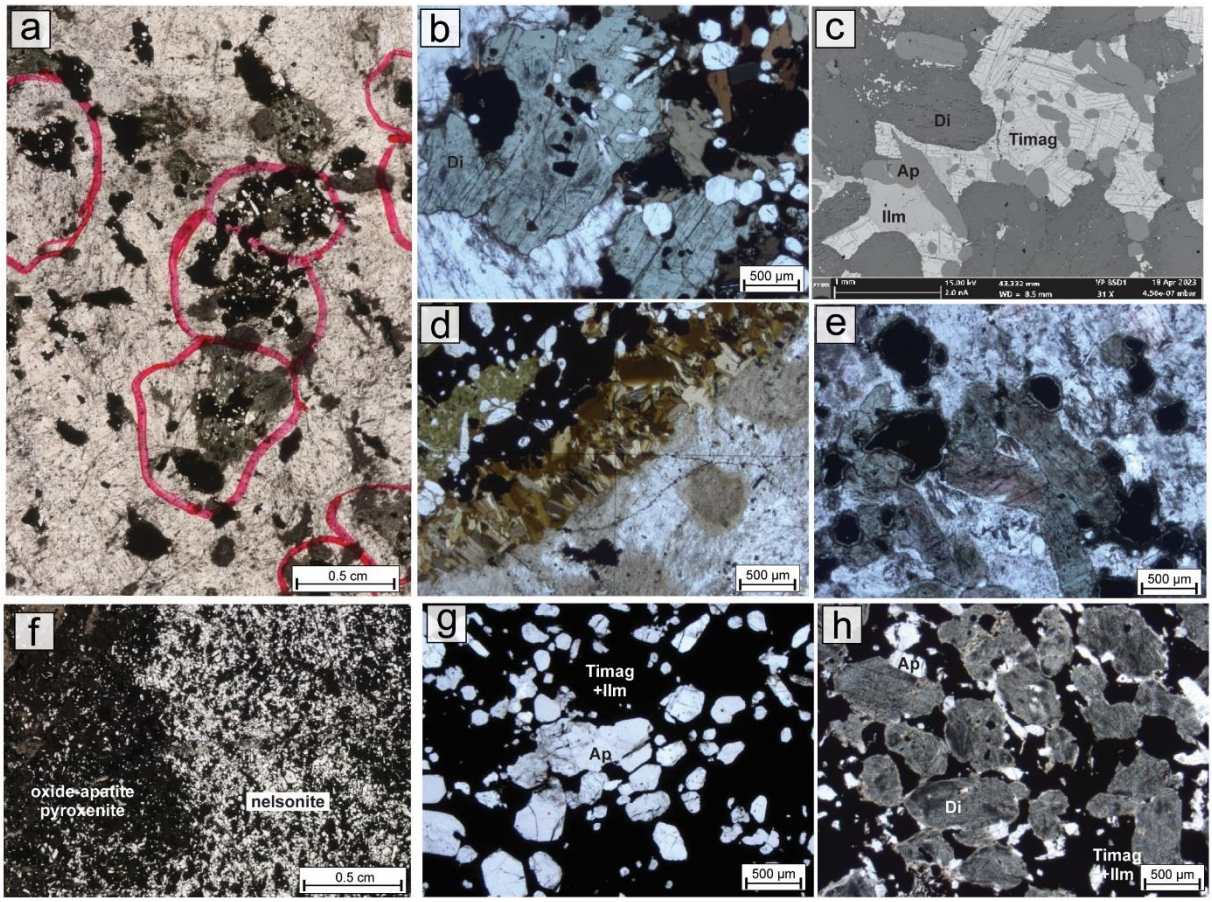

Figure 17: A. Scanned thin section image of the monzonite host rock showing the interstitial Fe-Ti oxides, apatite and clinopyroxene. B. Transmitted light photomicrograph of interstitial clinopyroxene, apatite and Fe-Ti oxides in the monzonite. C. BSE image of interstitial clinopyroxene, apatite and Fe-Ti oxides in the monzonite. D. Transmitted light photomicrograph showing an agglomeration of biotite in the contact between the ternary feldspar and Fe-Ti oxides. E. Transmitted light photomicrograph showing clinopyroxenite, Fe-Ti oxide and apatite in in the monzodiorite. F. Scanned thin section image of the contact between the oxide-apatite pyroxene and nelsonite. G. Nelsonite massive ore comprising abundant euhedral apatite crystals both included within and at contact with magnetite. H. oxide-apatite pyroxenite massive ore with partial alteration of the clinopyroxene crystals along fractures and rims.

In the monzodiorite the feldspars are mostly anhedral and contain inclusions of very fine-grained apatite needles (Fig. 17E). Clinopyroxene is subhedral, forms either aggregates with other clinopyroxene, magnetite and minor apatite (Fig. 17E) or occurs as homogeneously disseminated single grains. Titanomagnetite forms rounded grains together with ilmenite and show few ilmenite exsolution. Moreover, titanomagnetite is surrounded by a thin rim of titanite at the contact with surrounding silicates.

In the nelsonite, apatite grains occur included within larger Fe-Ti oxide masses or display sharp contact with smaller crystals. The proportion of apatite is highly variable but is commonly greater than 30% of the rock volume (Fig. 17F-H). In the oxide-apatite pyroxenite, the clinopyroxene crystals are medium- to fine-grained, and like those in the monzonite, display amphibole and biotite alteration along the edges (Fig. 17H).

Host rock		P2O5 wt%	CaO wt%	SiO2 wt%	F wt%	Cl wt%	Mn ppm	La ppm	Ce ppm	Nd ppm
Monzodiorite (n=7)	Min	41.38	52.09	0.296	2.545	0.125	470	660	3360	930
	Max	42.29	55.62	0.668	2.798	0.149	700	5470	8880	3680
	Mean	41.84	54.74	0.464	2.677	0.134	617	2381	4796	2007
	Median	41.89	55.22	0.384	2.706	0.132	660	1760	4150	1670
Monzonite (n=28)	Min	41.46	53.25	0.25	2.468	0.033	90	bdl	940	930
	Max	42.82	55.80	0.58	3.54	0.516	1080	7940	11620	5130
	Mean	42.15	54.69	0.353	2.891	0.196	424	3301	5937	2484
	Median	42.09	54.66	0.342	2.871	0.169	310	2935	5560	2555
Nelsonite (n=31)	Min	42.23	52.59	0.168	2.435	0.048	bdl	bdl	370	650
	Max	43.81	55.17	0.382	3.065	0.243	940	4010	6800	3040
	Mean	42.76	54.44	0.288	2.689	0.168	309	1866	4425	2025
	Median	42.76	54.40	0.290	2.704	0.166	310	1970	4600	2060
Oxide-apatite clinopyroxene (n=32)	Min	40.89	54.43	0.269	2.271	0.063	bdl	bdl	1190	bdl
	Max	43.93	55.40	0.501	2.751	0.792	1060	4890	7700	3050
	Mean	41.99	55.00	0.353	2.508	0.232	387	2232	4262	1831
	Median	41.98	55.02	0.331	2.509	0.158	380	2150	4080	1805

Table 4: Electron microprobe analyses of major, minor and trace elements in apatite from Kodal.

Minor and trace elements of apatite, titanomagnetite and ilmenite are currently being used to constrain the genesis of the Kodal deposit and are the topic of an ongoing work. Here, we present a summary of the major and minor elements analysed by microprobe.

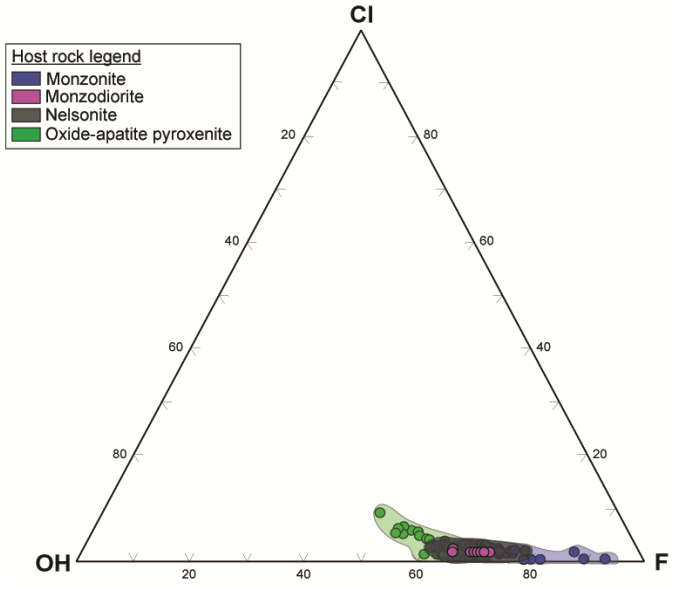

Figure 18: Ternary diagram showing the distribution of Cl, F and OH in apatite from different host rocks.

The concentration ranges for F, Cl, Mn, La, Ce and Nd in apatite, grouped by host rock type, are presented in the Table 4. Overall, apatite contains >2 wt% F and <1 wt% Cl (Table 4). The OH mole fraction in apatite was calculated according to Piccoli and Candela (2002) and

the results are plotted in the F-Cl-OH ternary space (Fig. 18). Kodal apatite displays <10 % mole fraction of Cl and shows a trend with decreasing F following increasing OH from monzonite to nelsonite/monzodiorite to oxide-apatite pyroxenite (Fig. 18).

Host rock		Fe %	Ti %	Mn ppm	Mg ppm	Al ppm	Cr ppm	V ppm	Zn ppm
Monzodiorite (n=4)	Min	70.14	0.219	1820	84	1307	75	487	410
	Max	71.72	0.887	6831	873	3551	151	711	466
	Mean	70.91	0.455	3218	455	2028	104	609	438
	Median	70.90	0.358	2110	431	1627	96	619	438
Monzonite (n=9)	Min	64.40	0.898	1866	398	3567	75	515	1253
	Max	69.81	4.613	13499	1496	9442	164	1277	2691
	Mean	68.54	1.808	5544	909	6447	116	891	1822
	Median	69.36	1.316	4608	838	6901	109	835	1615
Nelsonite (n=14)	Min	63.80	1.864	3733	1351	4694	75	1165	651
	Max	67.40	4.233	7993	11012	10754	185	1568	2434
	Mean	66.30	2.621	4775	5118	7657	125	1410	1467
	Median	66.76	2.485	4449	4942	7343	116	1437	1410
Oxide-apatite clinopyroxene (n=9)	Min	63.98	1.849	4322	1272	2943	89	879	715
	Max	67.28	4.747	7644	6242	10299	192	1669	2161
	Mean	65.76	3.629	6152	3740	7113	127	1242	1546
	Median	66.01	4.141	6420	3377	7648	116	1059	1711

Table 5: Electron microprobe analyses of major and minor elements in magnetite from Kodal.

The concentration ranges of La, Ce, and Nd are similar for apatite from nelsonite, oxide-apatite pyroxenite and monzodiorite, but differ from apatite hosted in the monzonite which yield the highest contents of La, Ce and Nd (Table 4).

Host rock		Mn %	Mg %	Al %	Cr %	V %	Zn ppm	Nb ppm	Ta ppm	Zr ppm
Monzodiorite (n=3)	Min	7.032	0.130	0.002	bdl	0.195	193	930	bdl	577
	Max	9.653	0.316	0.010	0.012	0.200	731	1573	770	614
	Mean	8.218	0.243	0.007	0.006	0.198	485	1179	257	597
	Median	7.968	0.282	0.010	0.005	0.198	530	1035	-	600
Monzonite (n=2)	Min	2.596	0.072	0.019	0.001	0.188	bdl	1216	377	489
	Max	2.943	0.320	0.022	0.007	0.201	844	1545	1368	688
	Mean	2.750	0.207	0.020	0.004	0.193	511	4145	846	614
	Median	2.710	0.229	0.020	0.003	0.190	691	1475	794	666
Nelsonite (n=11)	Min	1.802	0.182	0.019	bdl	0.188	bdl	517	bdl	570
	Max	4.030	1.623	0.110	0.016	0.216	844	895	1433	962
	Mean	2.561	0.836	0.031	0.007	0.205	373	698	283	782
	Median	2.385	0.671	0.022	0.005	0.207	193	699	0	792
Oxide-apatite clinopyroxene (n=8)	Min	1.866	0.137	0.021	0.001	0.192	257	238	bdl	777
	Max	3.586	1.368	0.034	0.010	0.217	1173	1028	1843	1177
	Mean	2.670	0.873	0.027	0.007	0.204	625	603	619	939
	Median	2.560	0.961	0.028	0.006	0.203	526	552	536	951

Table 6: Electron microprobe analyses of major and minor elements in ilmenite from Kodal.

Magnetite and ilmenite compositions also vary according to host rock types. Tables 5 and 6 show a summary of magnetite and ilmenite compositions and figure 3.4.5 highlights few elements that are useful to constrain the genesis of the Kodal deposit. The concentration of both very compatible (Cr, Ni, V, Zn and Mg) and less compatible (such as Al) elements in magnetite are higher in nelsonite and oxide-apatite pyroxenite compared to magnetite hosted in monzonite and monzodiorite (Figure 19A). Similarly, Zr, which is a compatible element in ilmenite, and Al and V (less compatible elements) are higher in nelsonite and oxide-apatite pyroxenite ilmenite relative to those from the monzonite and monzodiorite.

3.4.1.2 Petrogenetic processes behind the formation of the Kodal deposit

The formation of nelsonites in magmatic systems still highly debated. This is because a nelsonitic magma does not exist in nature and therefore, it is a result of fractional crystallisation, silicate-liquid immiscibility or mineral accumulation (Philpotts 1967; Charlier et al. 2008; Tollari et al. 2008). Lindberg (1985) proposed that at Kodal, the nelsonite would have formed by the early crystallisation of Fe-Ti oxides and apatite suggesting accumulation as the main process. Alternatively, Kragh and Jensen (1991) and Buelens and co-authors (2024) suggested that liquid immiscibility would have been the process involved in the origin of Kodal nelsonite, without providing detailed evidence of the process. Finally, Andersen and Seiersten (1994) proposed that Kodal represent a cumulate of ultramafic minerals formed at depth and carried upward during the emplacement of the monzonite.

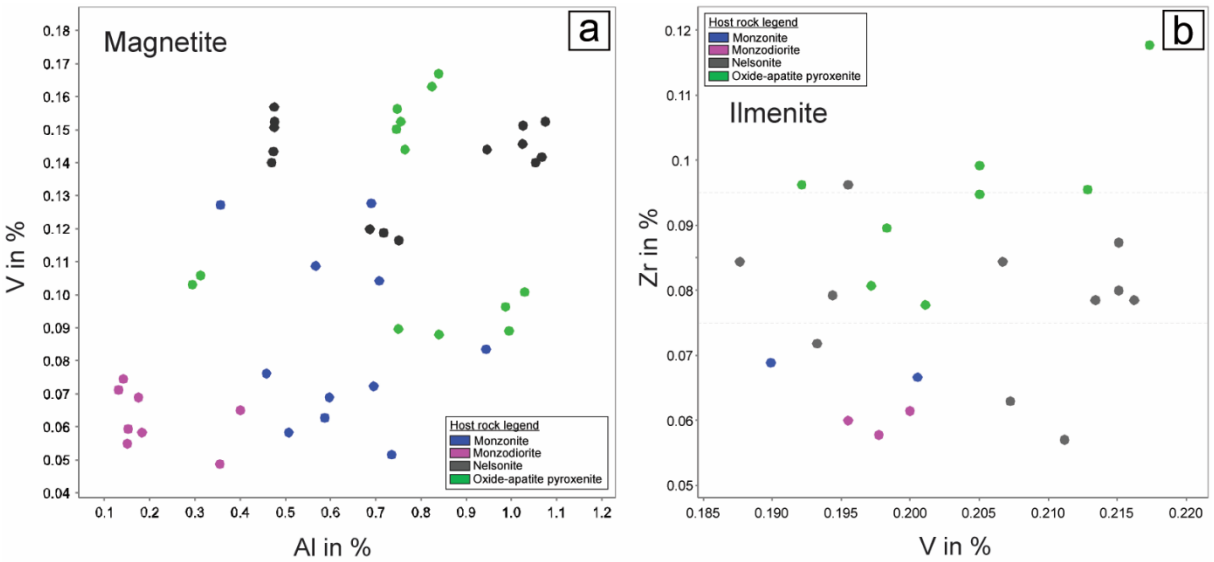

Figure 19: Biplot showing the distribution of V % vs Al % in magnetite (A) and Zr % vs V % in ilmenite (B) in different host rocks.

Charlier and Grove (2012) showed that the silicate-liquid immiscibility of a magma is achieved by fractional crystallisation, variations in melt composition caused by assimilation,

and by magma mixing. Our results support that silicate-liquid immiscibility mainly caused by magma mixing was essential for the formation of Kodal Fe-Ti-P mineralisation. One evidence for that is the concentration of Fe-Ti oxides and apatite at the contact between the monzonite and syenite (Fig. 17A), observed either in the drill cores and at the field in the west part of the Kodal deposit. Moreover, the similar crystallisation age between the monzonite, Fe-Ti-P mineralisation and the syenite suggest that the syenite, previously considered to postdate Kodal, is in fact cogenetic and intruded into the monzonite while the latter was still unconsolidated.

Microprobe results also show that incompatible and compatible elements of ilmenite and magnetite are both enriched in nelsonite and oxide-apatite pyroxenite relative to monzonite. Upon fractional crystallisation of a magma, compatible elements are the first ones to be incorporated into mineral structure, whereas incompatible elements remain in the melt until the end of the crystallisation. In the case of silicate-liquid immiscibility, i.e., Si- and Fe-rich melts, transition elements (including Ni, Cr, V) and HFSE (including Ti and REE) partition preferentially into the Fe-rich melt over the Si-rich melt (Schmidt et al. 2006; Veksler et al. 2006). Therefore, both compatible and incompatible elements behave similarly in the Fe-rich melt, and minerals that crystallize from a Fe-rich melt will be enriched in these elements.

Our results support that the combination of field observations, petrography and mineral chemistry is essential for the understanding of complex Fe-Ti-P mineral systems such as the Kodal deposit. We suggest that silicate-liquid immiscibility triggered by magma mingling was essential for the origin of the Fe-Ti oxide and apatite mineralisation at Kodal. The findings present here offer important insights into the genesis of unusual Fe-Ti oxide and apatite mineralisation in alkaline magmatic systems.

3.4.2 Formation Zr-REE-Nb mineralisation

The presence of Fe-Ti-P-rich rocks throughout monzonitic intrusions indicate that the process responsible for their formation was widespread in the monzonite from the southern part of the Oslo rift. Similarly, Zr-REE-Nb-rich rocks were found in several intrusions, locally in the vicinity of Fe-Ti-P-rich occurrences, but not exclusively. They display similar relationships with the host syenite or quartz monzonite as Fe-Ti-P-rich rocks do with monzonite and are found mostly in mingling zones where a syenitic magma has been involved.

Crystallisation of a residual melt which evolved through fractional crystallization and as a result is enriched in HFSE does not fit with the melanocratic nature of the rock (Fig. 11F-H). The lack of pegmatitic texture and thorough alteration in the Zr-Nb-(REE)-rich rocks indicate

that they are unlikely related exclusively to the formation of late-stage fluids in syenite. Accumulation of mafic and heavy minerals from a syenitic magma is an alternative explanation, but the lack of evidence for a well-developed modal layering or strong magmatic flow necessary to concentrate such a large amount of mafic minerals suggests otherwise. A third alternative is silicate liquid immiscibility, the same process proposed for the genesis of the Kodal deposit (see chapter 3.4.1). This hypothesis explains the low Si content of the mineralisation and their elevated concentrations in Nb, Zr and REE relative to their host syenite, as many trace elements tend to partition in the Fe-rich melt (e.g. Lester et al. 2013).

In several cases, occurrences lie in the vicinity of the contact with the Skien B1 basalts (Flyttig and Hesterønningane; Fig. 9). Close to the contact, the latter shows evidence of ductile deformation associated with metasomatism (epidote-rich veins), but its role, if any, in triggering the formation of the mineralisation remains unclear. Further study, including experimental and detailed studies of the Zr-Nb-REE occurrences, are necessary to understand and properly constrain the petrogenetic processes at stake.

3.4.3 Nepheline occurrences

No detailed petrogenetic studies relating the modal content of nepheline to a particular process in the lardalite (nepheline monzonite) or nepheline syenite exist; however, field and textural observations suggest that two distinct processes, or series of processes, are responsible for the formation of these occurrences. Lardalite classify as nepheline monzodiorite to nepheline monzonite in the international classification. The rock texture in the lardalite at the Farrisvann occurrence is typical of a cumulate (Fig. 3D) where both feldspar and nepheline euhedral phenocrysts have been physically accumulated along the contact with unit VIII of the LPC (Fig. 14). Variations of the nepheline/feldspar ratio, minerals which have similar densities, could relate to a difference in the magma composition which becomes more evolved toward the contact unit VIII. Nepheline syenite or foayite is more evolved than the lardalite (higher alkali, Fe, Si and lower Ca contents; Fig. 2). Its texture strongly differs from that of the lardalite. Alkali feldspar is prismatic, locally oriented by flow (trachytic texture), whereas nepheline is anhedral (Schjølberg 2023; Fig. 3E) suggesting that, unlike in the lardalite, nepheline crystallized late when the magma was more evolved. These observations are in accordance with nepheline from the Farrisvann being more enriched in Ca and depleted in K and Fe compared to nepheline from Anundsjøen.

The high modal proportion of nepheline in some areas of the LPC relate to either accumulation of nepheline and feldspar relative to other minerals or to evolution of a silica-undersaturated nepheline syenite magma.

4. PROSPECTIVITY MAPPING AND TESTING OF EXPLORATION TOOLS

As part of this project, we explored potential tools that can be used to assess the potential for Fe-Ti-P-(REE) associated with intrusive rocks of intermediate composition in the southern part of the Oslo rift. We first explore regional-scale prospectivity mapping, integrating data from various geophysical surveys and whole-rock geochemical data, using supervised machine learning. Based on the results, we then conduct local tests of two indirect methods drone-based magnetic surveys and soil geochemical sampling in areas identified as prospective by the model.

4.1 Supervised machine learning framework

This chapter comprises parts of the published manuscript by Wang and co-authors (2024; https://doi.org/10.3390/min14040377), including most of the illustrations. Since then, we field-proofed one more area, results which are added in the last subchapter (4.1.4.4).

“Machine learning has emerged as a powerful tool in the field of mineral potential mapping, and its successful applications have been reported across the world (Harris et al. 2022; Wang et al. 2023; Jiang et al. 2013; Juliani and Ellefmo 2019; Prado et al. 2020). One of its primary strengths in this context lies in its capacity to efficiently handle extensive and intricate multivariate datasets, a substantial improvement over traditional methods. Furthermore, machine learning allows for objective data integration, reducing the potential biases that can arise from human expertise. However, there are also potential limitations associated with this data-driven approach. In mineral exploration, it can be challenging to train models effectively due to limited and biased data. Typically, there are more negative cases (non-mineralized) than positive cases (mineralized), simply due to the rarity of mineral resources, and available data may be incomplete. For instance, only confirmed positive samples (known mineralisation) may be available, and negative samples (rocks devoid of mineralisation) must be randomly selected and/or conform to specific empirical guidelines from the area of interest. These factors can impact the accuracy and reliability of the models used in mineral exploration. Machine learning models are often considered as ‘black boxes’, meaning it can be difficult to understand how the

algorithms arrive at their predictions from the multi-variate features or how these features are associated with the underlying geological processes that control the mineralisation. In this project, we address these limitations and combine data science with geological domain expertise in developing our predictive model.

Based on the results from previous regional studies (Ihlen et al. 2014; Lindberg 1985), and especially known mineralisation sites such as Kodal (Andersen and Seiersten 1994; Bergstøl 1972), it is possible to identify critical parameters that characterize the Fe-Ti-P-REE mineralisation in the area. For instance, due to abundant magnetite, the mineralisation is characterized by positive magnetic anomalies (1000-3000 nT), whereas low content of potassium (K)-rich minerals yields lower K concentrations (generally below 2%) relative to the host rocks (Appendix A). Moreover, the mineralisation seems to be more promptly eroded relative to host rocks, thus being present in topographic depressions of secondary importance. These contrasting petrophysical properties of the ore compared to the host rock make this type of mineralisation prone to be detected by various classical geophysical exploration tools such as radiometric and magnetic surveys.

This study is dedicated to employing a machine learning approach to identify potential areas for early-stage exploration of Fe-Ti-P-REE resources within the southern Oslo Rift region. Existing high-resolution spatial datasets, including airborne magnetic, radiometric, and topographic maps, were used to generate predictive features, and rock samples with geochemical analyses were processed into training samples. For generation of the predictive model, two widely used classifiers were evaluated: random forest (RF) (Breiman 2001), which is splitting-based, and support vector machine (SVM) (Cortes and Vapnik 1995), which is continuity-based. Both classifiers were implemented with modifications to handle imbalanced datasets (i.e., there are significantly more negative samples than the positive ones) by adjusting class weights based on class frequencies and adjusting the cost matrix to penalize assigning samples to the overrepresented class (negative, non-mineralized) more heavily. The RF classification model was selected due to its superior performance, and the generated predictive map was compared to legacy data and verified in the field. It is proven valuable in terms of narrowing down areas that require further investigation for mineral exploration.

4.1.1 Data

This study utilizes high-resolution geospatial datasets, including airborne geophysics and the digital elevation model (DEM), to create a set of features as the input to our machine learning

model. Based on the domain knowledge described previously, these features are likely indicative of the target mineralisation, enabling us to build a robust predictive framework for mineralisation prospectivity assessment. To prepare the geospatial datasets and based on data availability, we extended the coverage beyond the study area, as shown in figure 20D. The magnetic and radiometric airborne geophysical datasets are compiled and stitched from multiple surveys conducted at different times. The compilations are provided by the Geological Survey of Norway (NGU) (https://geo.ngu.no/geoscienceportalopen/Search), which have a regular grid sampling resolution of 50 m. The magnetic data displays the total magnetic field anomaly (Fig. 20A), while the radiometric data indicates the abundance of potassium (K), thorium (Th), and uranium (U) in rocks and soils. An example of processed K data in weight percentage is presented in figure 20B.

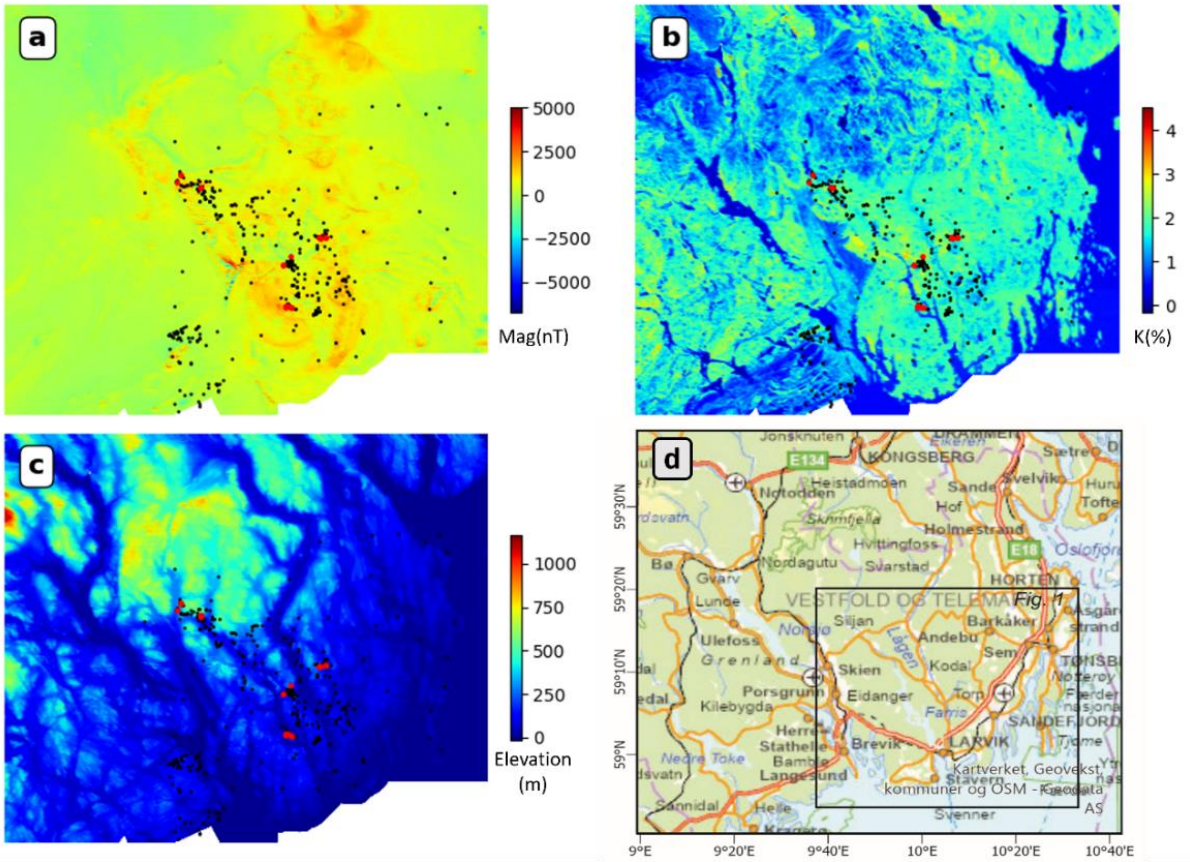

Figure 20: The high-resolution geospatial datasets projected onto a uniform grid with 50 m cell size: a) The total magnetic field anomaly (nT); b) Potassium (K) concentration (%); c) Topography (DEM) (m); d) Geography map to indicate the data coverage which is beyond the study region shown in figures 1 and 9. Field sample locations are marked in a) – c) and differentiated by using red dots to indicate mineralized samples and black dots to indicate non-mineralized samples. Figure from Ying et al. 2024.

For the DEM data used in this study (Fig. 20C), we obtained them from the Norwegian Mapping Authority (Kartverket) at a spatial resolution of 50 m (downloaded in January 2023 from

https://hoydedata.no/LaserInnsyn2/. To ensure spatial alignment of the features used in developing the predictive model, all datasets were projected onto a uniform grid with a cell size of 50 m.

To ensure a comprehensive training dataset, geologists collected and identified both positive and negative samples across different geological units for good spatial coverage. Geochemical data consisting of ICP-MS (inductively coupled plasma mass spectrometry) analysis from these field samples were used to measure the concentration of elements of interest in rocks. The methodology for the analyses followed as that reported in Coint et al. (2020). During the data preparation stage, mineralogists were consulted to separate the samples into positive and negative training datasets using geochemical and mineralogical indicator. We categorized our field samples based on their P_2O_5 concentration. Samples with P_2O_5 contents exceeding 4 wt. % were classified as mineralized, whereas those with P_2O_5 contents below 4 wt. % were categorized as non-mineralized. This concentration corresponds to the cut-off of the resource estimated associated with the Siilinjärvi deposit (see chapter 3.3 for more detail), only place where phosphorous is actively extracted in Europe. These classified samples were used as ground truth to develop a training dataset for our predictive model. Of the collected samples, 23 were classified as mineralized, whereas 406 were classified as non-mineralized. The distribution of the classified samples is marked in figures 20A-C on top of the geospatial maps.

4.1.2 Methodology and workflow

4.1.2.1 Training data sampling strategy

Figures 20A-C highlight a key advantage of our samples: their broad spatial distribution provides extensive coverage and a high proportion of confirmed negative samples, eliminating the need for synthetic negatives (e.g. SMOTE by Chawla et al. 2002). However, the dataset is highly imbalanced, with a 1:18 ratio of mineralized to non-mineralized samples, posing challenges for classification models that favour the majority class. Since mineral prospectivity mapping prioritizes identifying the minority class, we designed a sampling strategy to address this imbalance.

We assigned class labels to grid cells (50 m resolution) surrounding field samples. Negative training samples were drawn from a 50 m range around non-mineralized samples, while a larger 100 m range was used for mineralized samples. Overlapping grid cells were classified as positive, as shown in figure 21. This conservative spatial assignment ensures high-

resolution features are fully leveraged for better differentiation. It also aligns with mineral exploration logic – locations with both sample types suggest potential mineralisation.

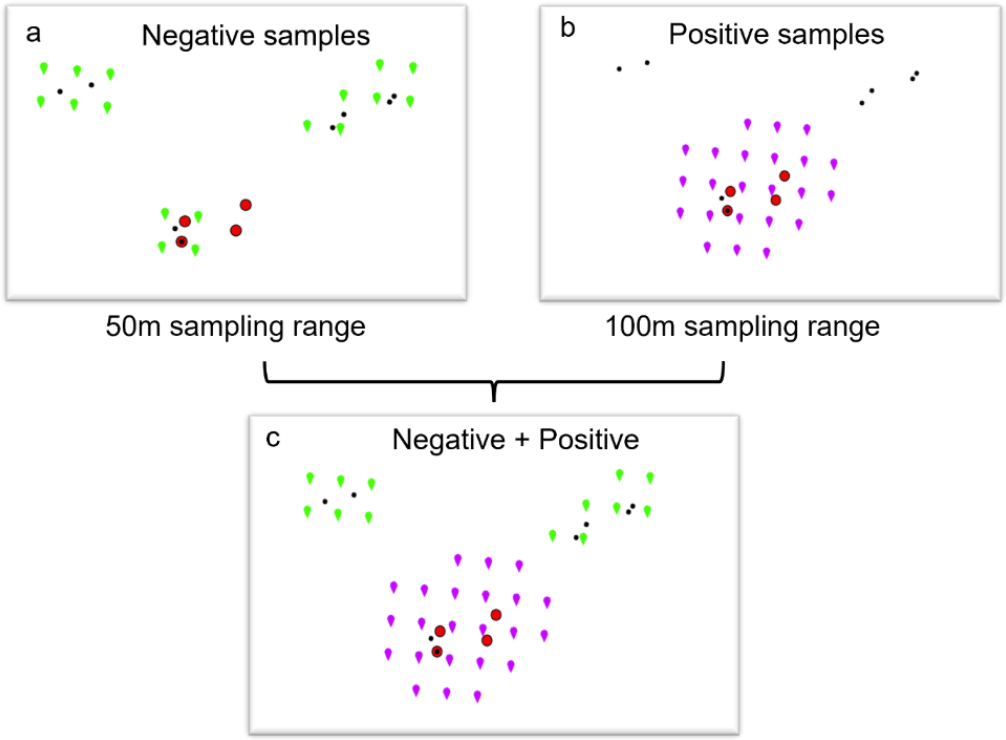

Figure 21: Illustration of the training data sampling strategy. The true locations of non-mineralized (i.e. negative) and mineralized (i.e. positive) field samples are indicated by black dots and red circles, respectively. The green and magenta pointers correspond to the uniform grid (with 50 m cell size) onto which the high-resolution spatial datasets are projected. Specifically, all green pointers are located within 50 m distance from at least one non-mineralized field sample, whereas all magenta pointers are located within 100 m from at least one mineralized sample. Figure from Ying et al. 2024.

The final training dataset achieves a more balanced 1:5.7 ratio (174:997), significantly improving upon the initial imbalance.

4.1.2.2 Feature engineering

Feature engineering is essential in machine learning, involving the extraction of meaningful features from raw data to enhance model performance. In this study, geoscientists with expertise in geophysics, geology, and mineralogy collaborated to identify significant features from three high-resolution geospatial datasets relevant to the target mineralisation.

For magnetic data, we applied filtering techniques commonly used in geophysical interpretation (Blakely 1996). These included upward continuation (enhancing deep-seated magnetic sources), analytical signal (highlighting shallow sources), and derivative-based filters (vertical and tilt derivatives) to enhance anomaly edges. Histogram equalization and logarithmic transformation were used when necessary to improve contrast and discriminatory

power. Five candidate features were generated: histogram-equalized magnetic data, analytical signal with logarithmic transformation, upward continuation at 500 m, vertical derivative with histogram equalization, and tilt derivative.

For radiometric data, we assessed absolute concentrations and ratios of K, Th, and U. Ratio operations (Th/K, U/K, U/Th) were applied to highlight anomalies, as individual channels tend to correlate in most rock types (Dentith and Mudge 2014). Six predictive features were derived: three histogram-equalized element channels (K, Th, U) and three ratio-based features (Th/K, U/K, U/Th). The analytical signal of Th/K with logarithmic transformation was included based on expert recommendations.

For topographic data, we extracted five predictive features: histogram-equalized DEM, vertical derivative, slope, and aspect components. Since topographic aspect is circular (0° and 360° both representing north), we transformed it into sine and cosine components to represent north-south and east-west facing slopes, ensuring a linear representation of slope direction.

We computed a 2D correlation matrix of all 16 candidate features using Pearson's correlation coefficient (-1 to +1, with 0 indicating no correlation). To prevent redundancy and improve model performance, we selected only independent features, setting a 0.7 correlation threshold. Four highly correlated features (mag_ft, mag_tdr, Th_ft, and U_ft) were removed. The final 12 features include 3 magnetic, 4 radiometric, and 5 topographic features, ensuring a diverse and uncorrelated input set for classification models. We refer to Wang et al. (2024) for detailed figures illustrating the engineered features and the selection process.

4.1.2.3 Classification model generation

After creating a training dataset with 174 mineralized and 997 non-mineralized samples, each represented by a 12-dimensional feature vector, we trained a classification model. Stratified random sampling ensured the class ratio was preserved, with 80% (936 samples) used for training/validation and 20% (235 samples) for testing.

We tested Random Forest (RF) and Support Vector Machine (SVM), as both are well-suited for complex classification problems but differ in their approach – RF partitions data into discrete groups, while SVM separates classes using a hyperplane. Both were implemented using scikit-learn (v1.2.2), with adjustments for class imbalance via weighted class penalties.

Model tuning was performed using a 5-fold cross-validation scheme. RF parameters included the number of trees and minimum leaf size, while SVM tuning involved kernel

selection and regularization adjustments. RF outperformed SVM, achieving 0.949 accuracy and 0.815 F1 score, compared to SVM's 0.775 accuracy and 0.538 F1 score.

On the test set, RF achieved 0.962 accuracy, with 0.900 accuracy for mineralized samples and 0.971 for non-mineralized samples, confirming its robustness and ability to handle class imbalance. RF was selected as the final model to predict mineral potential across the study region.

4.1.3 Result: a prospective map

A prospectivity map for the target mineralisation (indicated by elevated P_2O_5 concentrations) was generated for the study region using the trained RF model on the 12 feature maps (chapter 4. 1.2) and is shown in figure 22.

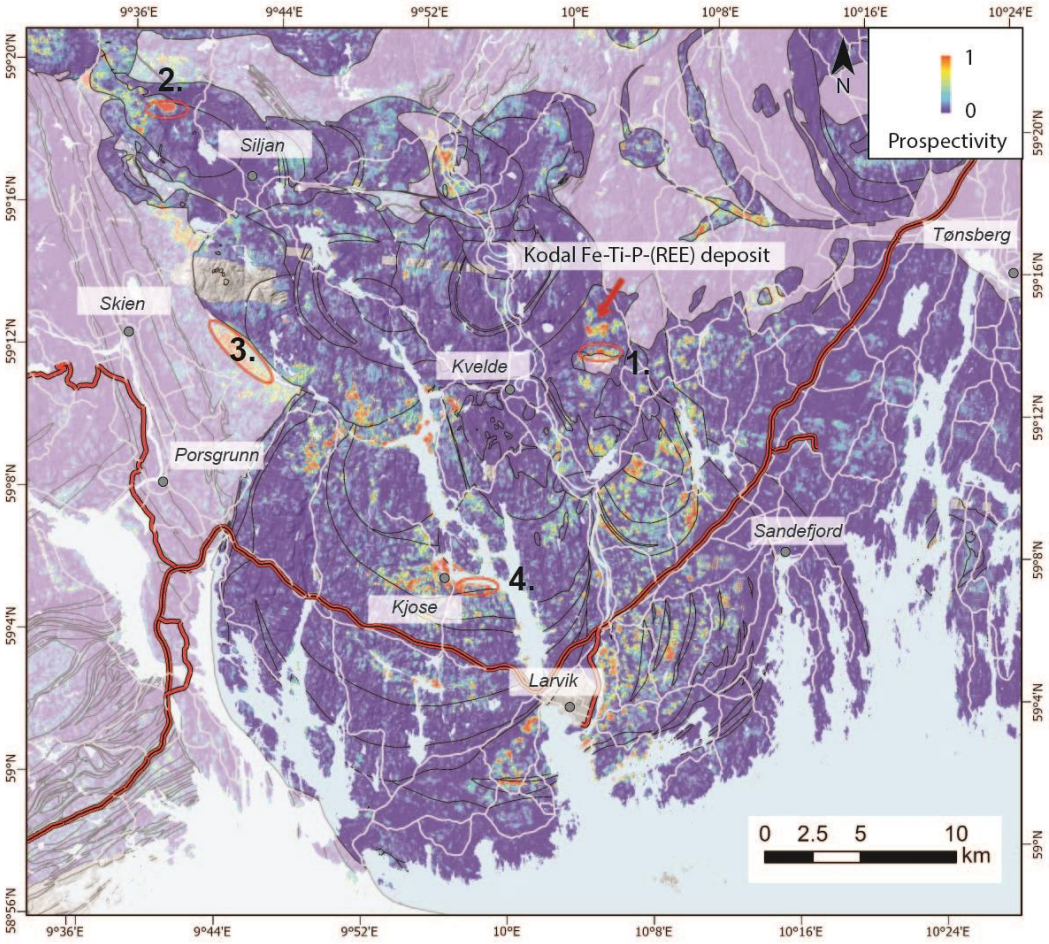

Figure 22: Prospectivity map of the target mineralisation generated using the RF classification model. The prospectivity measure is defined by the predicted probability of a sample belonging to the positive (mineralisation) class. Water bodies are masked and polygons where lithologies do not correspond to intermediate intrusive rocks are shaded in white. Figure modified from Ying et al. 2024. A high-resolution version of the figure can be downloaded with the supplementary material.

The map region contains 2 668 931 grid cells of size 50 m x 50 m. Each grid cell, referred to as a sample, is associated with a 12-dimentional feature vector and was classified by the trained RF model. Instead of using the predicted binary classes (mineralized or non-mineralized) directly for each sample, we opted to output the predicted probabilities of the sample belonging to the mineralized class. This probability measures the model's confidence in its predictions regarding whether a sample belongs to the mineralized class and therefore reflects the prospectivity of hosting the target mineralisation.

Permutation feature importances (Breiman, 2001) are computed to assess the importance of features in the trained RF model. These importances are quantified by assessing how much the model's prediction error increases when the values of a particular predictor are randomly shuffled or permuted. In figure 23, we show the feature importances in descending order, highlighting the most influential predictors. In general, the magnetic features and potassium (K) are the most important predictors for our model, while the topographic features are less influential. This is consistent with the domain knowledge described in 4.1.

Several areas are highlighted as highly prospective (yellow to red) for Fe-Ti-P-REE mineralisation in figure 22, and they make up about 0.3% of the entire region.

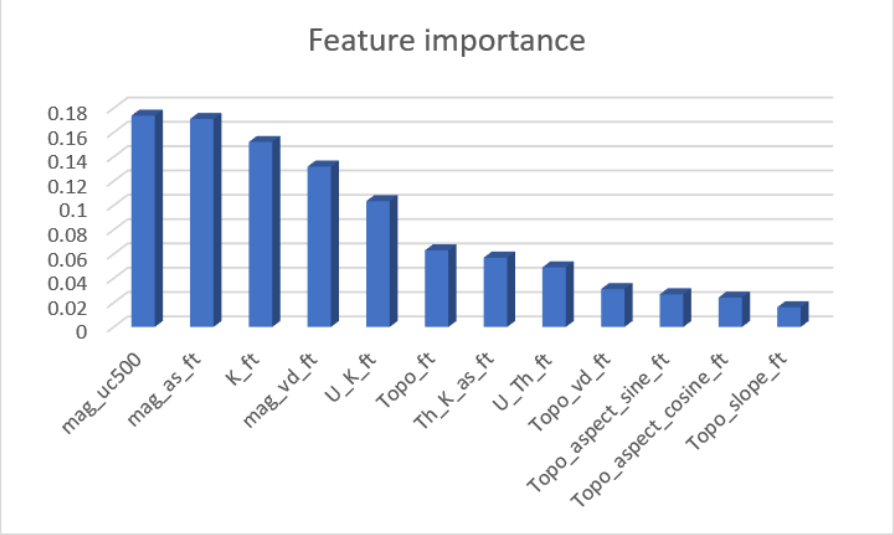

Figure 23: Feature importance for the RF model. Predictor abbreviations are explained in chapter 4.1.2. Figure from Ying et al. 2024.

4.1.4 Field-proofing

Field validation is essential to assess the quality of the prospectivity map. Four of the largest prospective areas were selected, including one of them we knew was unlikely to be mineralized

because of the lithology (Fig. 22, zone 3). Nevertheless, it is important to assess the strength, but also the pitfalls related to this new approach. We found Fe-Ti-P-(REE)-rich rocks in three out of four of them (Fig. 22). Below we go through each area and compare field observation with the prospectivity map.

4.1.4.1 Kodal I and Kodal II (Kodal area)

A second prospective anomaly, south of the main Kodal deposit (Kodal I) is visible in the prospectivity map (area 1 in Fig. 22). KODAL Minerals PLC, mineral exploration company who established the JORC resource estimate at Kodal I, reported the presence of some ore cropping out in the vicinity, in the location highlighted in figure 24A (Kodal Minerals 2017). Mapping in 2023 indicates that the magnetic anomaly is located at the boundary between a previously unknown fine-grained monzodiorite body and the main monzonite hosting the Kodal deposit. Like in many areas where Fe-Ti-P-rich rocks crop out, evidence of mingling and mixing between the two lithologies were documented and Fe-Ti-P-(REE) rich rocks were found in the mingling zone. Samples enriched in magnetite, ilmenite and apatite containing cm-scale phenocrysts of feldspars contain between 2.5 and 5.2 wt% P_2O_5 (Fig. 12, chapter 3.3.1), confirming the presence of Fe-Ti-P-rich rock in this area. The extent of the mineralisation at the surface is not possible to assess because of the extensive forest coverage and the challenging topography, however it confirms that the prospectivity map can lead to the discovery of new occurrences and the validity of such product to be used to guide future exploration projects in the area.

4.1.4.2 Siljan-Hvarnes intrusion

A second area of interest highlighted by the prospectivity map is the westernmost part of the Siljan-Hvarnes intrusion where three main prospective areas, corresponding to Kåsemyrene, Teigen and Meisholt occurrences are depicted by the map (Fig. 22 and 24B).

In Kåsemyrene, massive ore crops out in two old 2x3 m old excavation pits (Andersen 2021) (Fig. 11, chapter 3.3.1). The lack of outcrops in the vicinity of these pits prevent detailed geological mapping, however, evidence of Fe-Ti-P-(REE) patches and magma mingling is prevalent in the few outcrops in proximity of the two pits. Interestingly, the area highlighted as prospective in the predictive map (Fig. 22) is more extensive (Fig. 24B) than the area where ore was found at the surface, suggesting that the occurrence might be more significant than previously assumed. Further systematic mineral prospection is needed in the area to determine the extent of the latter. In the next chapter we deploy a drone magnetic survey over the area, in

addition to a soil survey to explore the potential extent of the mineralisation (see Chapters 4.2.3 and 4.3).

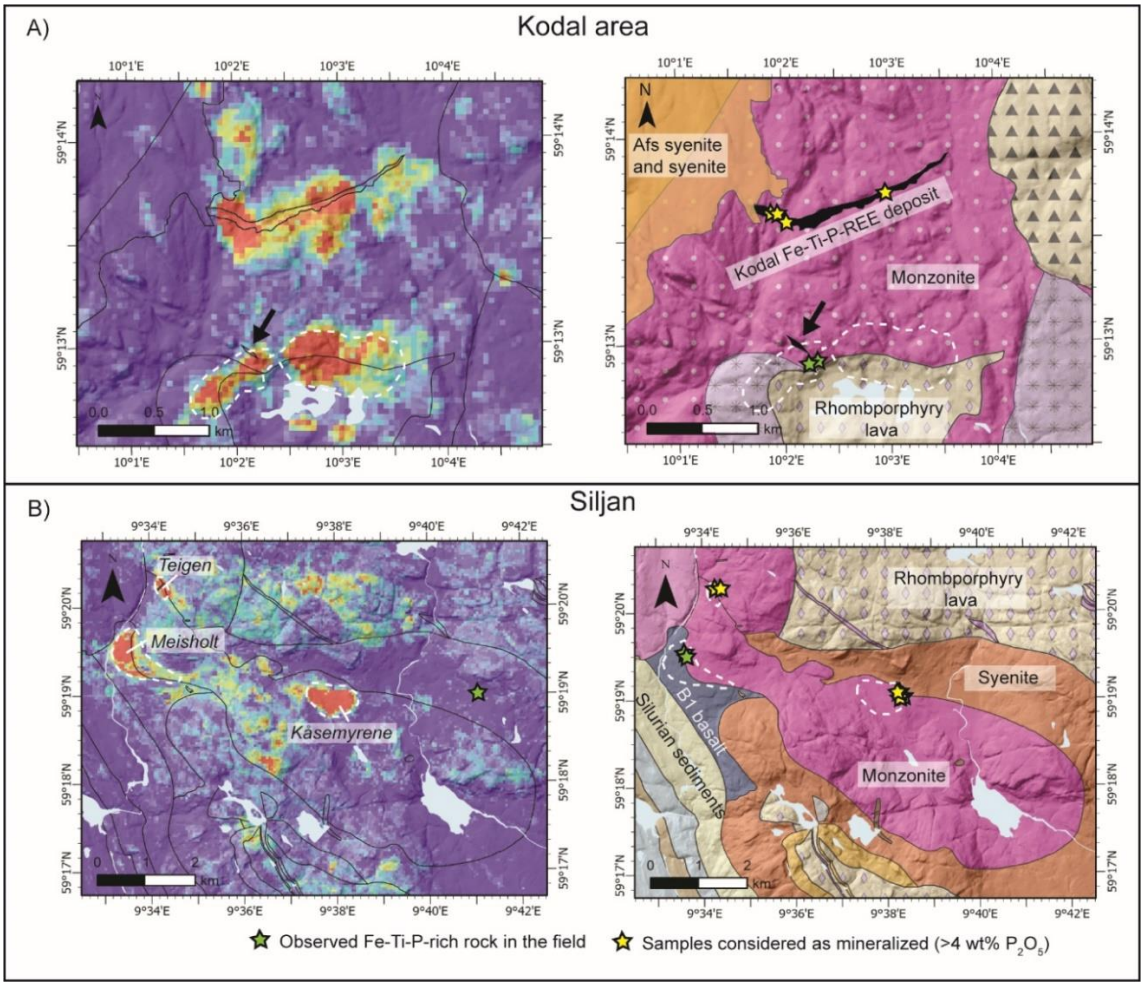

Figure 24: A) Prospective and geologic maps of the Kodal area. The black arrow depicts the location where ore was observed by Kodal minerals PLC in 2010. Green stars show the location of the ore we discovered while field-proofing the predictive map. B) Prospective and geologic maps of the westernmost part of the Siljan-Hvarnes intrusion highlighting mineralisation in Teigen, Meisholt and Kåsemyrene. Figure from Ying et al. 2024.

In Teigen, the prospectivity map does not predict the presence of a larger mineralized body associated with the occurrence we already sampled (see Chapter 3.3.1), information that can be taken further in planning future exploration surveys, after ground proofing the nature of the anomaly.

The Meisholt occurrence (Fig. 24B), like in Kåsemyrene, consists of several meter-scale excavation pits, where mineralisation crops out in contact with a coarse-grained monzonite. Samples retrieved from these pits do not reach more than 4 wt% P_2O_5 but can locally show enrichments in Nb and Zr (Fig. 12). Most of the prospective area highlighted by the prospectivity map is located within the basalt, according to the 1:250000 bedrock map, however after visiting the locality and sampling the mineralisation located close to the contact between

the syenite and the basalt, we suspect that the location contact might not be accurately located. Therefore, detailed mapping is required in this area to better understand the potential of this prospective anomaly.

4.1.4.3 Contact between B1-basalt and monzonite/syenites

Some prospective areas depicted by supervised machine learning however do not relate to the presence of Fe-Ti-P mineralisation. In the case of the area 3 (Fig. 22), the prospective area is located in basalt (Fig. 25), lithology which has similar petrophysical and geochemical characteristics as the Fe-Ti-P-rich rocks. Basalt is magnetic and contain low potassium, criteria depicted as prominent in the construction of the prospectivity map (Fig. 23). In order to remove false positive such as basaltic lithologies, we applied a shaded pattern to the polygon from the 1:250 000 bedrock map which did not correspond to the lithologies hosting Fe-Ti-P-rich mineralisation (Fig. 22). Uncertainties related to the location of the contact between the basalt and the syenite/monzonite on the map have to be considered carefully, as mentioned in the previous paragraph.

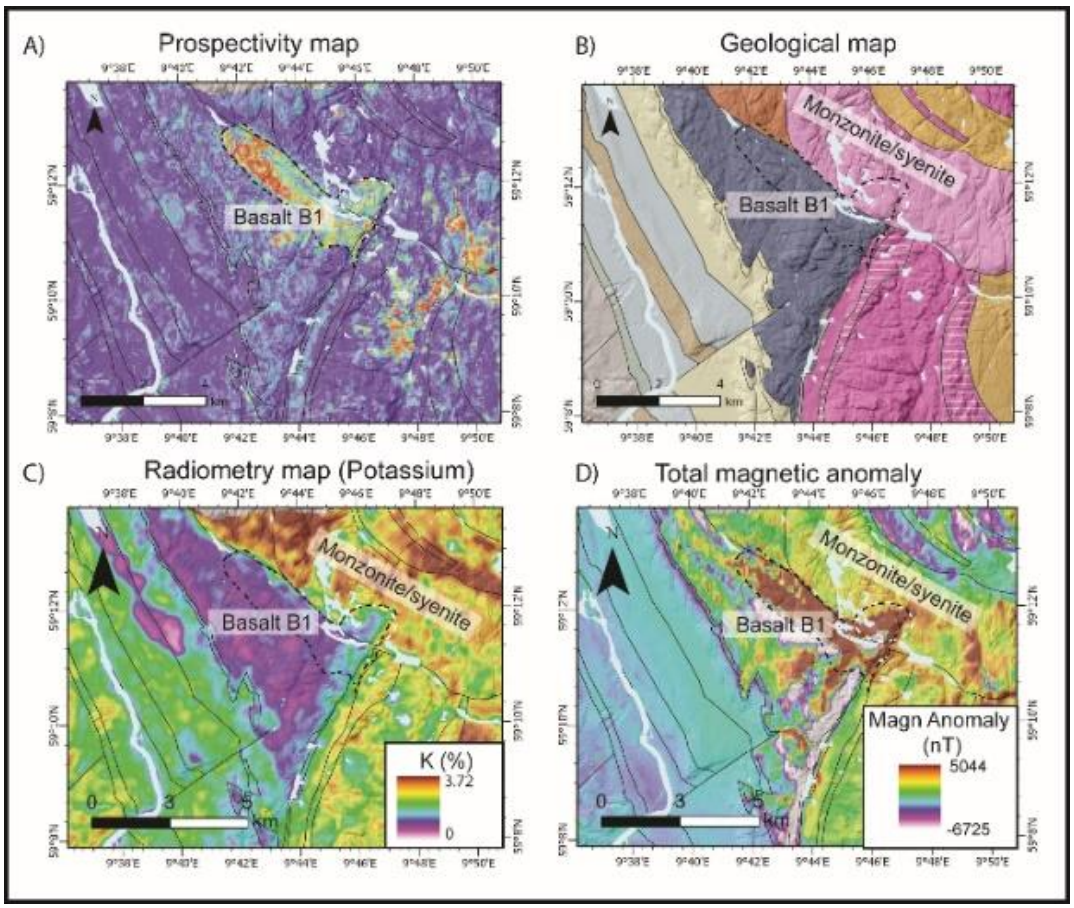

Figure 25: Comparison between the prospectivity map (A), the geologic map (B), the radiometry map for potassium (C) and the magnetic anomaly map (D). Figure from Ying et al. 2024.

The area with a lower prospectivity, indicated by the white dotted enclosure (Fig. 25) is nonetheless interesting. It is located in the syenite and monzonite. The potassium radiometric map shows that while the area does not have signature expected for basalt, it does not contain as much potassium as the surrounding monzonite and syenite. In the field, we could relate the high magnetic anomaly to the presence of pegmatitic syenites containing large crystals of magnetite, described as the Haukaråsen occurrence (Chapter 3.3.3). These pegmatitic rocks contain little phosphorous but have relatively high concentration of REE, Nb and Zr indicating that the prospectivity map also contains information that could highlight types of mineralisation that are not exactly the targeted ones but have similar properties, comparable to the case of Meisholt in Siljan where P_2O_5 concentration does not reach 4 wt %."

4.1.4.4 Kjose

Another area, located along the Farris Lake, close to Kjose, also appears as a prospective area on the prospectivity map (area 4 in figure 22). The occurrence of mineralisation along the lake shore (including on the southern side of the Bjørnøya island) was previously known, however, the prospectivity map shows that the mineralized area extends towards the East. Field proofing conducted summer of 2023 confirmed the presence of mineralisation eastward along the old train track and road parallel to the Farris Lake.

4.1.5 Summary

The use of machine learning, in this case supervised machine learning, provides a new powerful tool for targeted future mineral exploration campaigns. In the case of Fe-Ti-P-(REE) mineralisation, petrophysical and geochemical contrast between the ore and host-monzonite/syenite is large enough for regional datasets such as magnetics and radiometric data to record the presence of relatively small (100' meters to 1-2 km long and few meters wide) targets.

The presence of false positives indicates that despite the apparent robustness of machine learning, results have to be interpreted with care and that a thorough understanding of the local geology and the genesis of the mineralisation is necessary to use this map properly. Field proofing is essential before using the map to guide further prospective activities.

Applying machine learning methods to the available high-spatial resolution maps efficiently provides valuable insights to guide further investigation. Specifically, mineral exploration in the study area is challenging due to the extensive vegetation cover, making field

visits difficult. Geophysical data are cost-effective in terms of capturing large scale spatial variations in a short time. For this project, we benefited from these already available data to offer a first-order prediction of the study region's mineral potential for effective initial exploration.

4.2 Drone magnetic surveys

Magnetic data plays a crucial role in mineral exploration by defining the geometry, size and shape of important geological features of such as faults, contrast in lithologies and ore bodies. Over the past decades various methods of data filtering and inverse modelling have been developed and adapted for different applications, including mineral exploration (Nabighian et al. 2005). The recent arrival of drones on the market provides a new opportunity for conducting high-resolution magnetic surveys over areas which are potentially mineralized. Fe-Ti-P-(REE) mineralisation is enriched in magnetite (Chapter 3.3) which significantly contributes to the magnetic signature of a rock, making it an ideal target for this approach.

4.2.1 The main Kodal deposit

4.2.1.1 General considerations

The strategic objectives of the NGU involve conducting comprehensive aeromagnetic surveys across the entire country. This ongoing project progresses incrementally, and during the 1980s, the area encompassing the Kodal deposit (Fig. 26A & B) was surveyed using helicopter at an altitude of approximately 80 m above the ground. Only two flight lines passed over the close proximity of the mineralisation, rendering them insufficient for adequately constraining its geometry (Baranwal 2013; Fig. 29C).

With the rapid advancement of drone technology, it has recently become feasible to conduct aeromagnetic surveys using drones. Despite their limited range compared to helicopters or fixed-wing aircrafts, drone-based surveys offer at least three significant advantages:

1. They are substantially more cost-effective than other airborne surveying methods and are also more ecologically friendly.
2. They enable data collection with higher resolution at lower flight height, which is essential for accurately delineating and characterizing the three-dimensional structure of the target.

3. Drone surveys are versatile in that the pilot can adjust the flight plan in real time to address unexpected issues and situations or to change the data resolution.

In our study, we utilized a DJI M300 RTK multipurpose drone (Fig. 26D), equipped with a Sensys three-axis fluxgate magnetometer. Size and flight duration make this a suitable platform for surveying elongated ore bodies like the Kodal deposit, which have limited dimensions (Fig. 26B).

There are two main types of commonly used field magnetometers:

- Scalar magnetometers, which measure the total intensity of the geomagnetic field relative to fundamental physical constants.
- Vector magnetometers, which measure all three components of the geomagnetic field, but need more careful individual calibration.

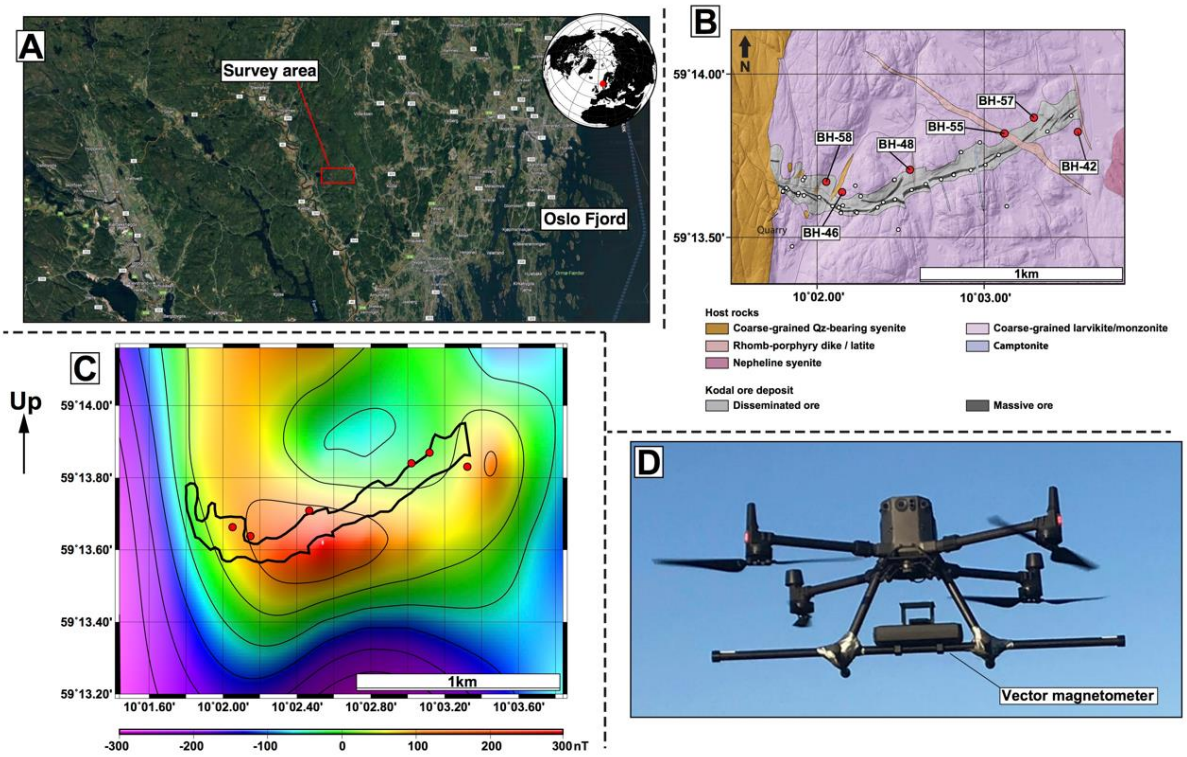

Figure 26: General presentation of the survey area. (A) Survey location. (B) Geologic map showing the location of boreholes and the associated profile of the Fe-Ti-P Kodal deposit on which the magnetic properties presented in table 7 were measured. (C) Regional magnetic data. These data have a low-resolution that make them impossible to directly interpret; however, they reveal a pattern consistent with what is observed on the drone magnetic anomalies. (D) Photo of the DJI M300 multipurpose drone with the 3-component R3 self-compensated magnetometer attached between its legs.

Scalar magnetometers are well-suited for helicopter surveys when suspended sufficiently far beneath the helicopter, to minimize interference from the helicopter's magnetic influence. This setup is not feasible for small drone surveys due to instability and payload

constraints. Here, a lightweight Sensys R3 3-component fluxgate magnetometer is rigidly attached to the drone body (Fig. 26D). This magnetometer is specifically designed for drone surveys and weighs a total of 1 kg including electronics and batteries. The magnetometer is equipped with two sensors. This is useful for reliability considerations as it allows us to double check the consistency of the data, in case one sensor fails. The data of the two sensors are of course included in the databases and since they are very much alike, we present here the result from only one of the sensors.

To quantify the drone's magnetic susceptibility tensor (a 3x3 matrix) and remanent magnetization vector (comprising three coefficients), we conducted daily calibration routines at the beginning of each morning's flight session (Honsho et al. 2009; Isezaki 1986). Drones lack moving parts besides their propellers and electric motors, such that their overall geometry remains constant during the survey. Their primary magnetic noise results from the currents driving the motors and moving permanent magnets within the motors. The noise potential of these sources remains consistent over time and is minimal in quiet flight conditions. Additional calibrations were therefore unnecessary in the Kodal survey.

The calibration flight patterns consist of alternating clockwise and counterclockwise loops to measure the geomagnetic field in all directions by different vector components of the magnetometer. These loops are followed by straight-line manoeuvres in various directions to cover the full range of positions the drone may assume during flight. During the Kodal survey, these patterns were executed at an altitude sufficiently high (approximately 50 m above the take-off point) to minimize the influence of any ground magnetic anomaly. Away from local sources, the variability of the magnetic measurements during the flight patterns can be attributed to the drone's magnetic influence. If no huge anomalies are present the constant background field should agree with the prediction of the local International Geomagnetic Reference Field (IGRF) (Alken et al. 2021; Thébault et al. 2015); The R3 magnetometer is self-compensated, equipped with an algorithm to quantify and eliminate the drone's magnetic influence from the data (https://sensysmagnetometer.com/products/magdrone-r4-magnetometer-for-drone/).

To cover the entire mineralisation and its surrounding host rock, we conducted a series of 40 flights along parallel routes spaced 20 meters apart, oriented at 340° perpendicular to the primary orientation of the Kodal ore body. The drone maintained an average speed of 3 m/s and a magnetic sampling frequency of 200 Hz. Official drone regulations prohibit flights exceeding 120 m above ground level (Norwegian Civil Aviation Authority: Flying drones in Norway

(https://luftfartstilsynet.no/en/drones/flying-in-norway/). At the time of the survey (June 2021), terrain-following capabilities were unavailable, i.e., the drone was flying at a constant altitude above sea level (and not above the ground). To remain within the permissible flight envelope, we manually adjusted the drone's altitude as needed.

4.2.1.2 Results

The magnetic data collected over the survey area were gridded using a minimum curvature algorithm (Smith and Wessel 1990) (Fig. 27A & B). Comparison to the IGRF reveals a prominent positive magnetic anomaly of up to 500 nT on the southern side of the mineralisation's outcropping portion.

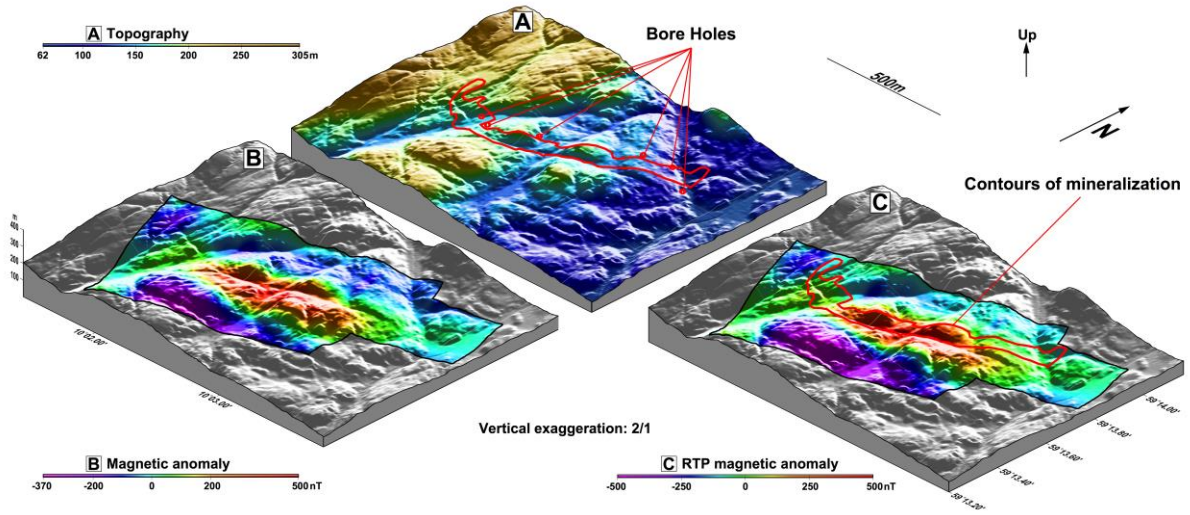

Figure 27: 3D representation of geophysical data collected during the drone-based aeromagnetic survey. (A) Topographic map with superimposed contours of the mineralisation. (B) Magnetic anomaly collected during the survey. (C) Reduction to the pole magnetic anomaly assuming the global magnetization vector aligns with the local geomagnetic field.

Interpreting these magnetic anomalies directly in terms of the ore body is complicated by the geometry of the geomagnetic field. Because the geomagnetic field is not vertical in the study area, the induced magnetic anomaly is shifted relative to its source. To address this issue, magnetic anomalies are commonly reduced to the pole (RTP). This transformation relocates the maximum of a magnetic anomaly above its source and minimizes horizontal dipolar components (e.g. Baranov 1957). Different methods can be used to perform this transformation. In our case, the data were acquired on a horizontal plane, which allowed the use of the direct RTP algorithms based on Fourier transform (Blakely 1995), without needing to first invert them into equivalent magnetization (e.g. Honsho et al. 2012).

A first attempt to reduce the magnetic anomalies to the pole assumed a purely induced magnetization within the local orientation of the IGRF. The resulting RTP magnetic anomaly, presented in figure 27C and 28A, still clearly displays a strong dipolar component. This indicates that the fundamental assumption of a purely induced magnetization is not optimal. We therefore need to explore other scenarios.

4.2.1.3 Discussion

In Kodal, the components of the IGRF at the time of the survey are:

X = 15.444 nT, Y = 1.029 nT, Z = 48.819 nT. The total field is F = 51.214 nT,

Inclination and declination are: I = 72.4°, and D = 3.8° (Alken et al. 2021; Thébault et al. 2015).

Two types of magnetizations exist within magnetized rocks: remanent magnetization and induced magnetization, both of which are vector quantities.

- **Remanent magnetization** can only be acquired by ferro-, ferri-, or antiferromagnetic materials when exposed to magnetic fields. The portion of magnetization that remains after the field is removed is known as remanent magnetization, or remanence. Depending on subsequent tectonic movements and changes of the geomagnetic field, remanent magnetization may not remain aligned with the local geomagnetic field.

- **Induced magnetization** arises spontaneously within any material when exposed to a magnetic field. In rock it is due to dia- and paramagnetic minerals in addition to the commonly dominating by ferro-, ferri-, or antiferromagnetic contributions. Except for extreme anisotropic cases, all these contributions align perfectly with the geomagnetic field direction.

For a young lithosphere, such as near a mid-ocean ridge axis - i.e., younger than the last geomagnetic polarity reversal at 780 ka (e.g. Cande and Kent 1995) – it is reasonable to assume that remanent and induced magnetization orientations are aligned and enhance each other (Szitkar et al. 2023; e.g. Dyment et al. 2018) However, for older crust and/or crust that has undergone tectonic movements, this assumption may not hold true (e.g. Szitkar et al. 2019; Szitkar and Dyment 2015; McEnroe et al. 2009). In our case, the mineralisation and surrounding host rock fall into the latter category. We therefore needed to find a way to estimate the characteristics of the average Natural Remanent Magnetization (NRM) of the Kodal mineralisation (e.g. Clark 2014).

In scientific drilling projects like IODP (International Ocean Discovery Program) or ICDP (International Continental Drilling Program), it is sometimes possible to reconstruct the geographic orientation of the remanent magnetization vector using the samples recovered from the bore holes. Especially in exploration drillings, a rotating cutting head is used and the axial orientation of the cylindrical sample that ends up inside the rotating tube of the drilling tool cannot be controlled.

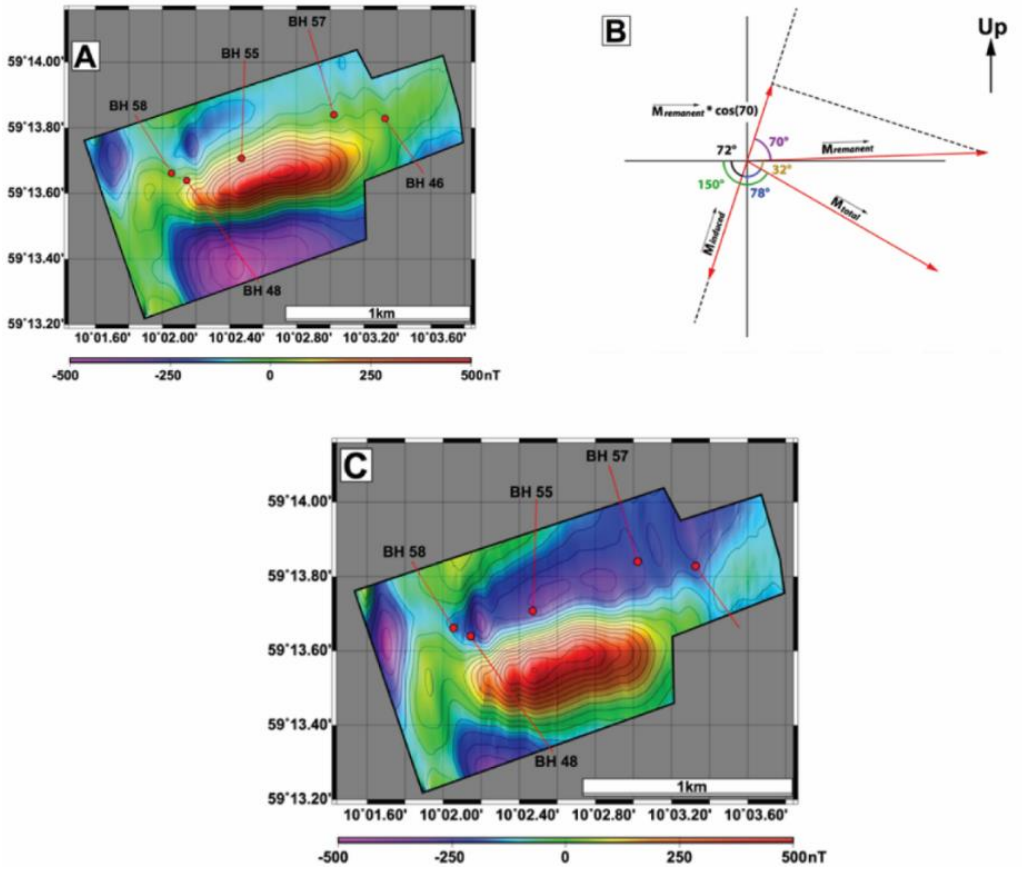

Figure 28: Optimization of the reduction to the pole. (A) RTP magnetic anomaly map using the local inclination and declination of the IGRF. This reduction is not optimal, as the RTP anomaly retains a strong dipolar component, necessitating adjustment. (B) Geometrical considerations leading to an optimized RTP magnetic anomaly. To suppress the dipolar component, a total magnetization vector with an inclination of 150° must be used. This deduction suggests the average remanence of the mineralisation has an inclination of 182°, partially counterbalancing the induced magnetization, which reduces the mineralisation magnetization at large scales. (C) Optimized RTP magnetic anomaly using the previously determined parameters. The dipolar component has been eliminated.

When brought back to the surface, it is highly likely that the rocks inside the rotating cutting tool are rotating as well, and it becomes impossible to reconstruct neither their original absolute nor their relative axial rotation with a satisfying degree of confidence. If the drill holes are perfectly vertical, this is a minor problem because the two radial components of the remanent magnetization vector would only misalign the magnetic declination D, and not the magnetic inclination I.

Table 7: Magnetic properties of various lithologies from the Kodal deposit cores

Lithology	Borehole number	Sample	East 32N_UTM	North 32N_UTM	Susceptibility (10^{-6} SI)	Remanense (mA/M)	Elevation (m)	Direction	Inclinaison	Core length (m)	Depth (m)
Mafic dike	BH57	KODAL091629	560214.67	6566239.72	14725	140	70	148	-45	121.3	46
Mafic dike	BH55	KODAL091617	560032.68	6566147.72	29363	131	129	156	-45	201.5	23.4
Syenite	BH58	KODAL091601	559023.69	6565866.73	158593	1698	159	195	-45	128.6	65
Syenite	BH58	KODAL091602	559023.69	6565866.73	31899	328	159	195	-45	128.6	66
Syenite	BH58	KODAL091603	559023.69	6565866.73	1713	367	159	195	-45	128.6	61
Syenite	BH58	KODAL091604	559023.69	6565866.73	11813	230	159	195	-45	128.6	66
Syenite	BH58	KODAL091605	559023.69	6565866.73	26574	775	159	195	-45	128.6	126
Syenite	BH-42	KODAL091641	560463.67	6566158.72	18370	181	68	339	-53	408	173.3
Syenite	BH-42	KODAL091642	560463.67	6566158.72	18273	3765	68	339	-53	408	180.1
Monzonite	BH48	KODAL091606	559418.68	6565881.72	61089	656	148	186	-46	193.3	4.5
Monzonite	BH48	KODAL091607	559418.68	6565881.72	69570	382	148	186	-46	193.3	9.8
Monzonite	BH55	KODAL091616	560032.68	6566147.72	81010	10313	129	156	-45	201.5	14.6
Monzonite	BH55	KODAL091618	560032.68	6566147.72	62480	2914	129	156	-45	201.5	30.2
Monzonite	BH55	KODAL091619	560032.68	6566147.72	75431	17469	129	156	-45	201.5	103.3
Monzonite	BH55	KODAL091620	560032.68	6566147.72	169477	4706	129	156	-45	201.5	124.5
Monzonite	BH57	KODAL091627	560214.67	6566239.72	86009	3367	70	148	-45	121.3	8.2
Monzonite	BH57	KODAL091628	560214.67	6566239.72	197593	22644	70	148	-45	121.3	26.4
Monzonite	BH57	KODAL091630	560214.67	6566239.72	35970	2637	70	148	-45	121.3	67.1
Monzonite	BH-42	KODAL091631	560463.67	6566158.72	36179	8375	68	339	-53	408	26
Monzonite	BH-42	KODAL091632	560463.67	6566158.72	106777	10517	68	339	-53	408	27.12
Monzonite	BH-42	KODAL091633	560463.67	6566158.72	64648	9832	68	339	-53	408	74.1
Monzonite	BH-42	KODAL091634	560463.67	6566158.72	127476	10707	68	339	-53	408	81
Monzonite	BH-42	KODAL091635	560463.67	6566158.72	187362	18814	68	339	-53	408	99.2
Monzonite	BH-58	KODAL091644	559023.69	6565866.73	212492	2260	159	195	-45	128.6	24.6
Monzonite	BH-46	KODAL091650	559116.69	6565821.73	60243	1562	166	180	-42	192	3
Monzonite	BH-46	KODAL091651	559116.69	6565821.73	52459	869	166	180	-42	192	10
Disseminated ore	BH48	KODAL091608	559418.68	6565881.72	187977	2857	148	186	-46	193.3	16.6
Disseminated ore	BH48	KODAL091609	559418.68	6565881.72	227945	133524	148	186	-46	193.3	28.2
Disseminated ore	BH48	KODAL091612	559418.68	6565881.72	383727	2770	148	186	-46	193.3	98.5
Disseminated ore	BH55	KODAL091621	560032.68	6566147.72	396706	24604	129	156	-45	201.5	129

Table 7: Magnetic properties of various lithologies from the Kodal deposit cores

Lithology	Borehole number	Sample	East 32N_UTM	North 32N_UTM	Susceptibility (10^{-6} SI)	Remanense (mA/M)	Elevation (m)	Direction	Inclinaison	Core length (m)	Depth (m)
Disseminated ore	BH55	KODAL091623	560032.68	6566147.72	196175	16632	129	156	-45	201.5	143.5
Disseminated ore	BH55	KODAL091626	560032.68	6566147.72	121856	1252	129	156	-45	201.5	186.8
Disseminated ore	BH-42	KODAL091636	560463.67	6566158.72	185100	33177	68	339	-53	408	108.7
Disseminated ore	BH-42	KODAL091637	560463.67	6566158.72	128222	2210	68	339	-53	408	114.1
Disseminated ore	BH-42	KODAL091638	560463.67	6566158.72	182157	80270	68	339	-53	408	117.8
Disseminated ore	BH-58	KODAL091643	559023.69	6565866.73	187700	4601	159	195	-45	128.6	7.3
Disseminated ore	BH-58	KODAL091645	559023.69	6565866.73	649174	101855	159	195	-45	128.6	30.4
Disseminated ore	BH-58	KODAL091646	559023.69	6565866.73	433164	15365	159	195	-45	128.6	46.7
Disseminated ore	BH-58	KODAL091647	559023.69	6565866.73	214449	4324	159	195	-45	128.6	75.6
Disseminated ore	BH-46	KODAL091652	559116.69	6565821.73	301711	48234	166	180	-42	192	34.5
Disseminated ore	BH-46	KODAL091653	559116.69	6565821.73	144254	1996	166	180	-42	192	76.2
Disseminated ore	BH-46	KODAL091654	559116.69	6565821.73	139816	1153	166	180	-42	192	98.6
Massive ore	BH48	KODAL091610	559418.68	6565881.72	654754	34947	148	186	-46	193.3	84.3
Massive ore	BH48	KODAL091611	559418.68	6565881.72	909919	18118	148	186	-46	193.3	94.1
Massive ore	BH48	KODAL091613	559418.68	6565881.72	593354	147824	148	186	-46	193.3	108.2
Massive ore	BH48	KODAL091614	559418.68	6565881.72	1518649	48619	148	186	-46	193.3	173.2
Massive ore	BH48	KODAL091615	559418.68	6565881.72	1294856	134677	148	186	-46	193.3	176.8
Massive ore	BH55	KODAL091622	560032.68	6566147.72	653906	15482	129	156	-45	201.5	135.5
Massive ore	BH55	KODAL091624	560032.68	6566147.72	1116388	78890	129	156	-45	201.5	156.5
Massive ore	BH55	KODAL091625	560032.68	6566147.72	843435	58713	129	156	-45	201.5	157
Massive ore	BH-42	KODAL091639	560463.67	6566158.72	614108	247012	68	339	-53	408	154
Massive ore	BH-42	KODAL091640	560463.67	6566158.72	264083	25502	68	339	-53	408	158.8
Massive ore	BH-58	KODAL091648	559023.69	6565866.73	750092	27764	159	195	-45	128.6	87.5
Massive ore	BH-58	KODAL091649	559023.69	6565866.73	1349874	18454	159	195	-45	128.6	10.25
Massive ore	BH-46	KODAL091655	559116.69	6565821.73	719820	364947	166	180	-42	192	129.6
Massive ore	BH-46	KODAL091656	559116.69	6565821.73	770300	24216	166	180	-42	192	139.3

Unfortunately, in our case, the drill holes were oblique with a 45° or 53° inclination (Table 7). In such a situation, the two radial components of the drill are no longer horizontal and their contribution to the magnetic inclination I varies depending on the chosen orientation. Since the original orientation of the recovered samples is impossible to determine, trying to estimate the orientation of the remanent magnetization vector using rock sample measurements is hopeless, and other approaches need to be explored.

To suppress the remaining dipolar component on the RTP magnetic anomaly, the only way is to assess the consequence of varying orientations of the total magnetization vector on its skewness. This vector being the sum of the induced and the remanent magnetization vectors, and the induced magnetization being known, it becomes possible to deduce the properties of the remanent magnetization vector.

We test different hypotheses for the orientation of the magnetization vector to optimize the RTP transformation. The results suggest that the total magnetization vector should have an inclination of ~150°, to be compared to the 72° of the induced magnetisation which is, by definition, aligned with the current geomagnetic field (see above for the characteristics of the IGRF) (Fig. 28B & C). Consequently, there is a difference of 78° between the inclination of the induced magnetization vector and that of the total magnetization vector.

To determine the direction of the remanent magnetization vector, an estimation of the intensity of the induced and the remanent magnetizations (i.e., of the norm of the vectors) is needed. We focus on the mineralisation, which is composed of pure and disseminated ore. The average magnetic susceptibility of the corresponding 30 recovered rock samples is equal to 0.56 SI. The ambient geomagnetic field intensity is F = 51.214 nT (Alken et al. 2021; Thébault et al. 2015), and the magnetic field strength is therefore:

H = F/μ_0 with $\mu_0 = 4.\pi * 10^{-7}$ => H = (51.214*10^{-9})/ ($4.\pi * 10^{-7}$) $\approx$ 41 A/m

Consequently, the average intensity of the induced magnetization of the Kodal mineralisation is M = χ.H = 0.56*41= 23 A/m, aligned with the local geomagnetic field (i.e., with an inclination of 72°). The average remanent magnetization intensity for the same samples is equal to 54 A/m, leading to a Koenigsberger ratio of Q = 2.34. The total magnetization vector having an inclination of 150°, the rules of vector summation reveals that the remanent magnetization can only have an inclination of 182° (Fig. 28B). Therefore, the projection of the remanent magnetization vector along the induced magnetization axis is equal to 54 * cos (70°) = 19 A/m in the opposite direction to that of the induced magnetization.

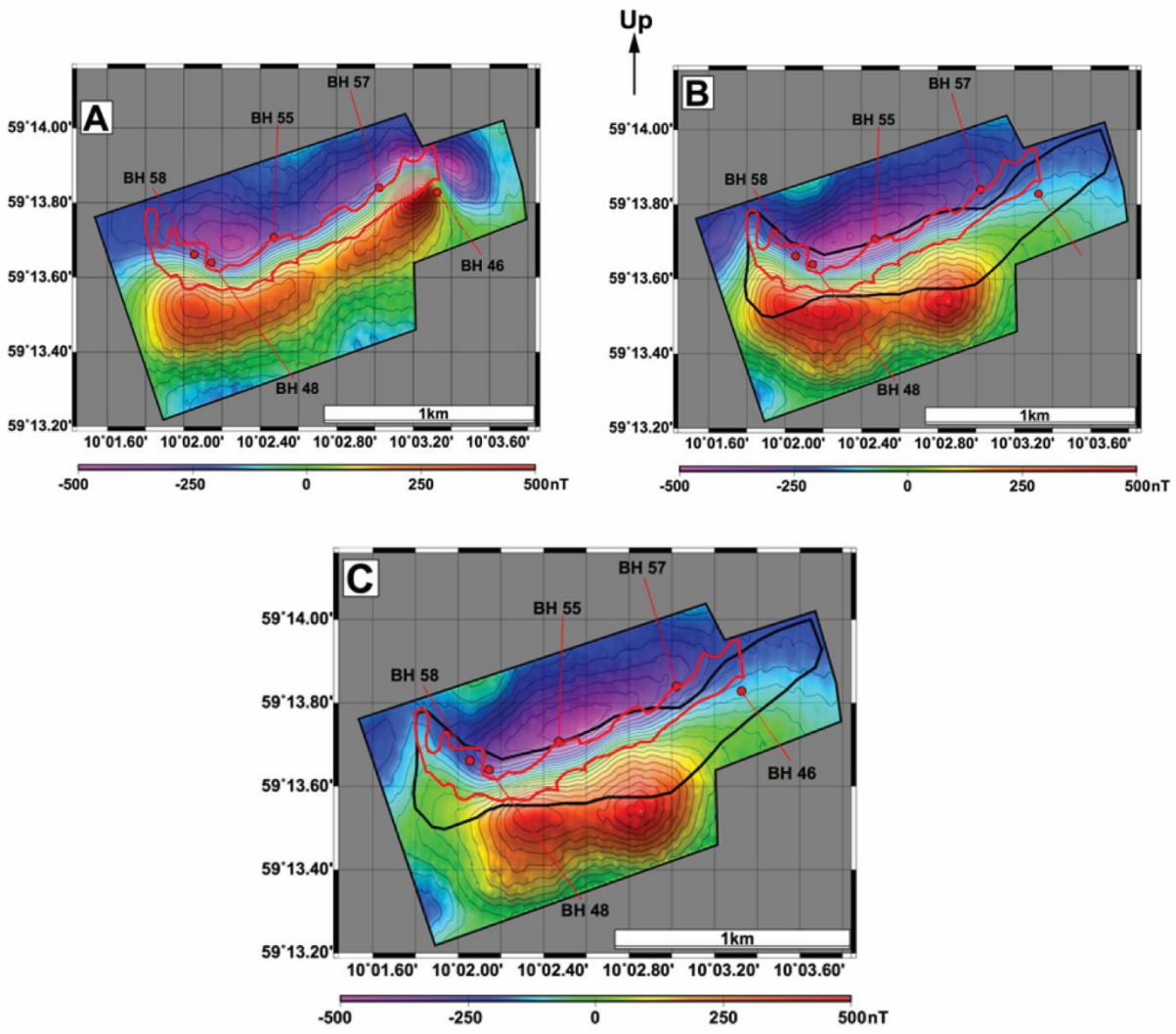

Figure 29: Magnetic models for the Kodal mineralisation. All models assume an 8 A/m magnetization for the mineralisation and a 2 A/m magnetization for the host rock, with vector orientations deduced from the RTP optimization process. (A) Synthetic magnetic anomaly assuming constant contours of the mineralisation at depth. The resulting anomaly has the same amplitude as the observed one, but the general shape does not match, indicating a change in the mineralisation geometry at depth, consistent with drilling observations. (B) Synthetic magnetic anomaly assuming the mineralisation shape progressively changes at depth, from its outcropping limits to those of the black contours at 100 m bgl. This shape is closer to the observed anomaly, but inconsistencies remain, particularly in the westernmost parts of the mineralisation. (C) Similar to (B) but assuming a weaker, 4 A/m magnetization in the western part, supported by geological evidence. The final synthetic magnetic anomaly matches the observed one in both amplitude and shape, leading to a well-constrained model of the Kodal mineralisation.

Consequently, there is a conflict between the induced and the remanent magnetizations which partially counterbalance and compensate each other's. Overall, the magnetization of the mineralisation is of approximately 8 A/m. The apparent mismatch between the amplitude of the magnetic anomaly measured by the drone and the magnetization values measured on the rock samples can therefore be explained by these conflicting magnetization vectors. In the following models, we use the 8 A/m value as the average magnetization of the mineralisation and deduce from it that the average magnetization of the surrounding host rock is equal to ~2 A/m.

4.2.1.4 Determination of the mineralisation 3D geometry

The optimized RTP magnetic anomaly reveals that the peak of the positive magnetic anomaly does not correspond to the outcropping part of the mineralisation but is instead shifted further south (Fig. 28C). Given the altitude of the drone flights, revealing sources located within the first hundreds of meters below the surface, such shift is consistent with a dipping of the mineralisation in the south direction, as also revealed by the drillings.

Now that the magnetization parameters (intensity and orientation) have been established, we can initiate the contouring of the mineralisation at depth (Fig. 29A & B). Defining its 3D geometry requires an iterative approach to avoid *ad-hoc* solutions. Rock sample measurements ensure that the model parameters are well-constrained.

1. The initial step involves leveraging the known surface contours of the mineralisation and extrapolating them to deeper levels. Based on our prior measurements, the overall magnetization within these contours is determined to be 8 A/m and the surrounding bedrock exhibits a magnetization of 2 A/m. We then proceed to calculate the synthetic magnetic anomaly within the experimental geometry (Fig. 29A), assuming a magnetized layer thickness of 500 meters. This thickness is not arbitrarily chosen; it aligns with findings from drillings, which indicate mineralisation extending to depths of several hundred meters below ground level. Furthermore, limitations in the geometry of the drone surveys restrict our ability to investigate magnetized sources beyond approximately 500 m depth. While the resulting synthetic magnetic anomaly accurately reflects the expected amplitude, its shape is found to be unsatisfactory as it is associated with a SW – NE orientation, unlike the observed magnetic anomaly which is characterized by an almost E-W orientation (Fig. 28C & 29A).

2. The combination of the outcropping shape of the mineralisation and its associated RTP magnetic signature suggests a shape at depth that differs from its surface contours. This hypothesis is confirmed by drillings, which reveal that the mineralisation dips towards the southeast as it extends eastwards. Thus, we propose a new contour for the mineralisation at 100 meters below ground level (bgl) and deeper. The contour gradually changes shape from the surface (red contour) to 100 meters bgl (black contour) (Fig. 29B). Adopting this contour at 100 meters bgl results in the synthetic magnetic anomaly

displayed in figure 29B, with a shape much closer to the observed one even if inconsistencies remain. The easternmost part of the mineralisation at this depth remains a hypothesis awaiting further testing through future drilling programs.

3. The final step involves assessing magnetization variations in the ore body towards the West (Fig. 27C). The observed positive magnetic anomaly has a smaller amplitude near the western end of the mineralisation compared to its centre. This smaller amplitude could be attributed to a deeply buried mineralisation, weaker magnetization of the host-rock and/or the mineralisation itself, or a combination of both (Fig. 28C). Nevertheless, since the Kodal deposit reaches ground level in its western part as well, the hypothesis of a deeper buried mineralisation can be ruled out in favour of variations of its average magnetization. Westward, the Kodal deposit is intersected by quartz-bearing syenite with lower susceptibility and remanence. This rock type may locally contribute to significant volumes, potentially explaining the weaker anomaly observed in the western part of the deposit. Additionally, samples from the westernmost boreholes (BH48 and 58), across all rock types, exhibit slightly lower susceptibility and remanence than samples further east. Magnetic measurements on drilled samples reveal that the average remanence of rocks is weaker in the west (Bore Hole BH-58) than in the east of the mineralisation.

Through gradual refinements and guided by geological observations and interpretation, we have derived a synthetic magnetic anomaly with a shape and amplitude consistent with the measured anomaly. The final model suggests a mineralisation with a shape that progressively changes at depth and with an average 8 A/m magnetization in the central and eastern parts, whereas its western part is associated with an average 4 A/m magnetization (Fig. 29C). This nested approach was therefore necessary to develop a realistic model of the 3D geometry of the Kodal Fe-Ti-P mineralisation (Fig. 30A & B).

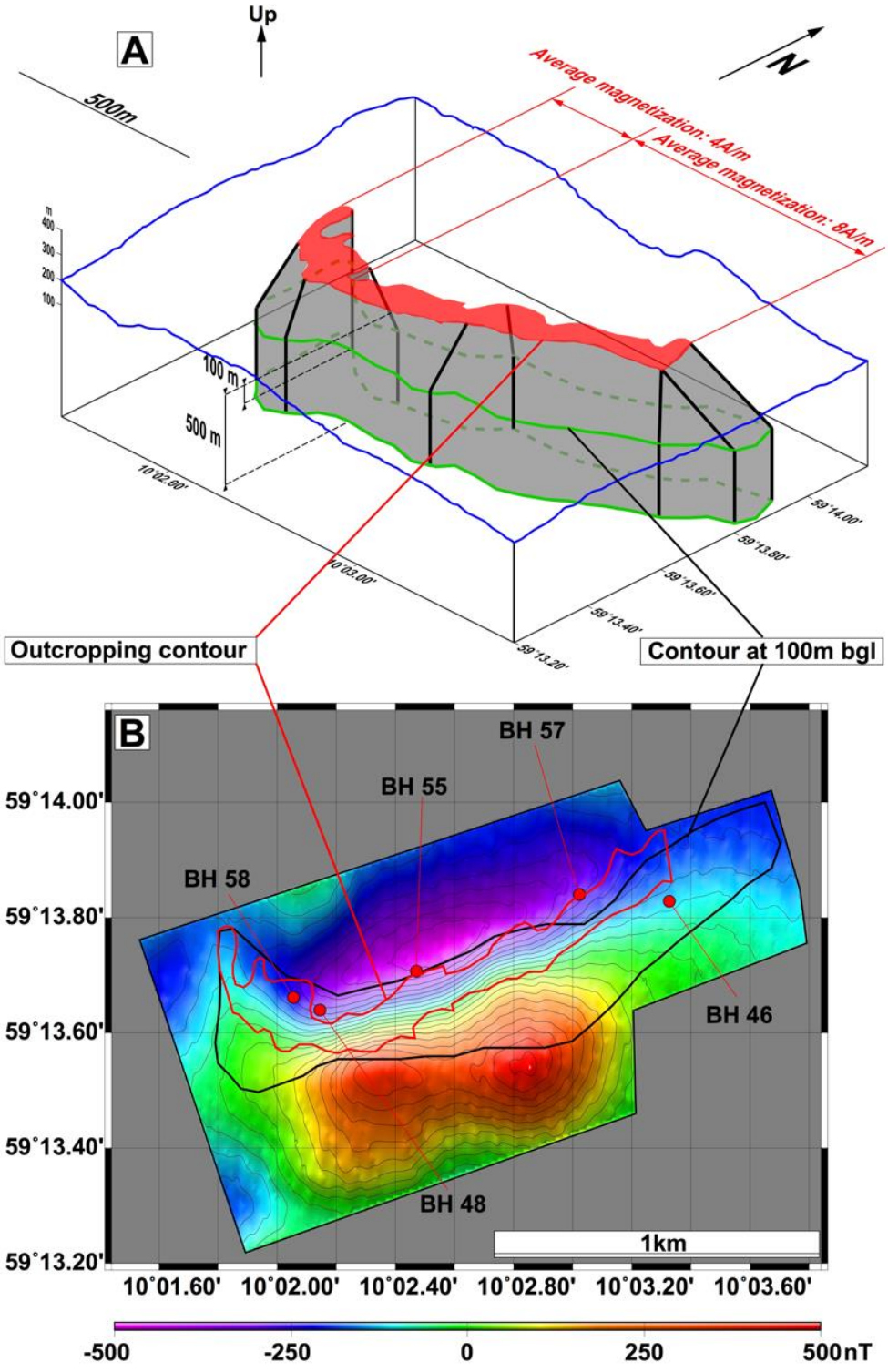

Figure 30: Visualization of the mineralisation 3D geometry. (A) 3D projection of the mineralisation geometry. (B) Synthetic magnetic anomaly considering the south-eastward dip. The black line represents the surface contour of the mineralisation, while the red line represents the estimated contour of the mineralisation 100 m below the topography.

Given the inherent uncertainties of potential field studies (e.g. Al-Chalabi 1971), it is important to note that this solution is not unequivocal. Nevertheless, the model parameters are well

constrained by geological observations and measurements and are therefore associated with a much higher degree of reliability than in many other modelling situations involving potential fields. Therefore, we have confidence that this model offers a realistic representation of the 3D geometry of the Kodal mineralisation.

4.2.2 Kodal II

The above-mentioned survey in Kodal was extended towards the South in June 2023 over an area labelled as Kodal II (or Kodal South). We flew the same DJI M300RTK drone with the magnetometer. The last area, in Siljan will be discussed in the next chapter of this report. The summary of the different survey locations is displayed in figure 31.

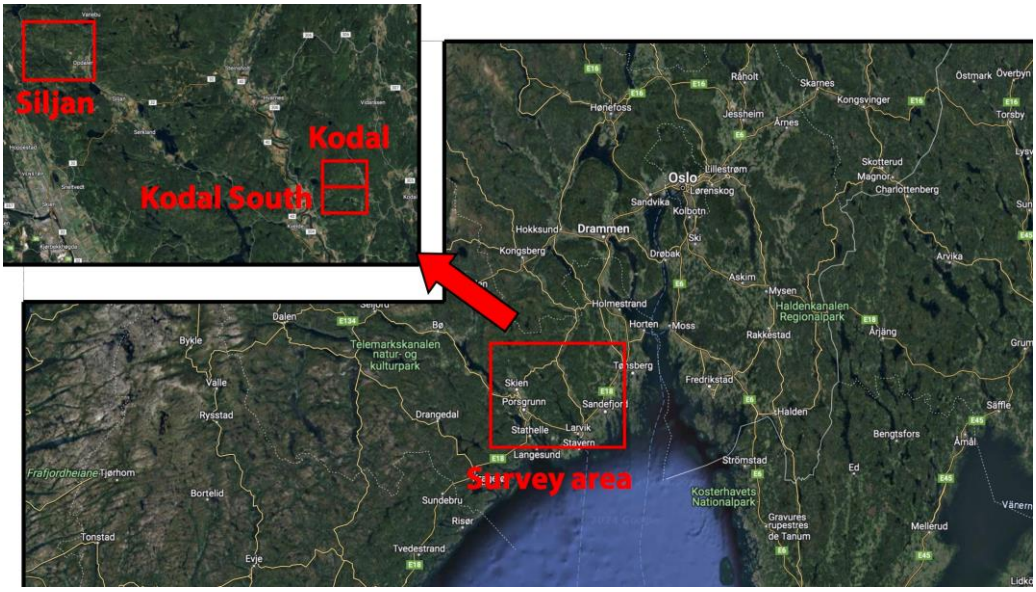

Figure 31: Localization of the surveys in Kodal II and Siljan compared to the first survey in Kodal. There is a continuum between the Kodal II and Kodal I areas.

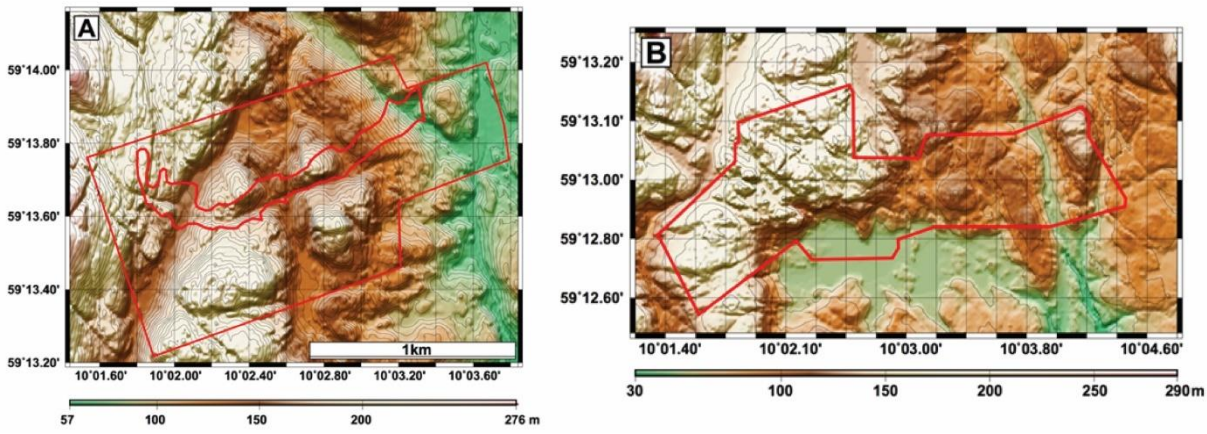

Figure 32: (A) Topography over Kodal I deposit and (B) Topography over Kodal II occurrence. The two areas are connected, ensuring a continuum in the magnetic data acquisitions.

The airborne survey started on June 24th, 2023, and continued until the 27th of June 2023. The drone took off from a single spot. We used the UGcS software, and the drone followed the topography, at an altitude of 80 m above the ground to cope with the demanding topography and dense tree cover. The topography of the area is displayed in figure 32 as well as the continuum with the first Kodal survey.

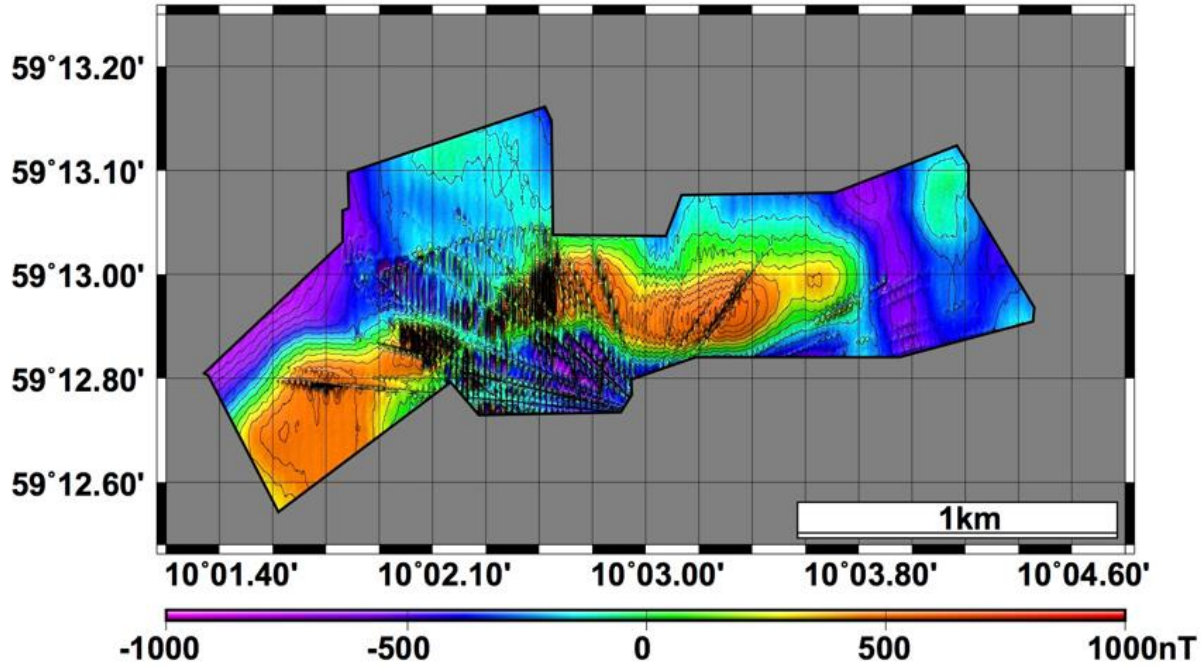

Figure 33: Raw magnetic anomaly over the Kodal II area. The lines with the shape of a fan starting from the south of the polygon are transit lines from and to the take-off point of the drone at the beginning and end of each flight. They are removed during the data processing.

In the Kodal II area, the routes were flown in an N-S direction. The total magnetic anomaly is presented in figure 33. A total of 136 lines were flown with a flying speed of 3 m/s and a total of 2 km^2 covered.

Magnetic data were recorded at 5 ms intervals, resulting in data with a sample increment of 1.5 cm. This sampling frequency is not adjustable, but it is higher than needed. It was therefore later down-sampled to a frequency of 1 acquisition per second, i.e., every 3 m for the main survey and 1 m for the high-resolution survey, which resulted in a drastic reduction of the noise.

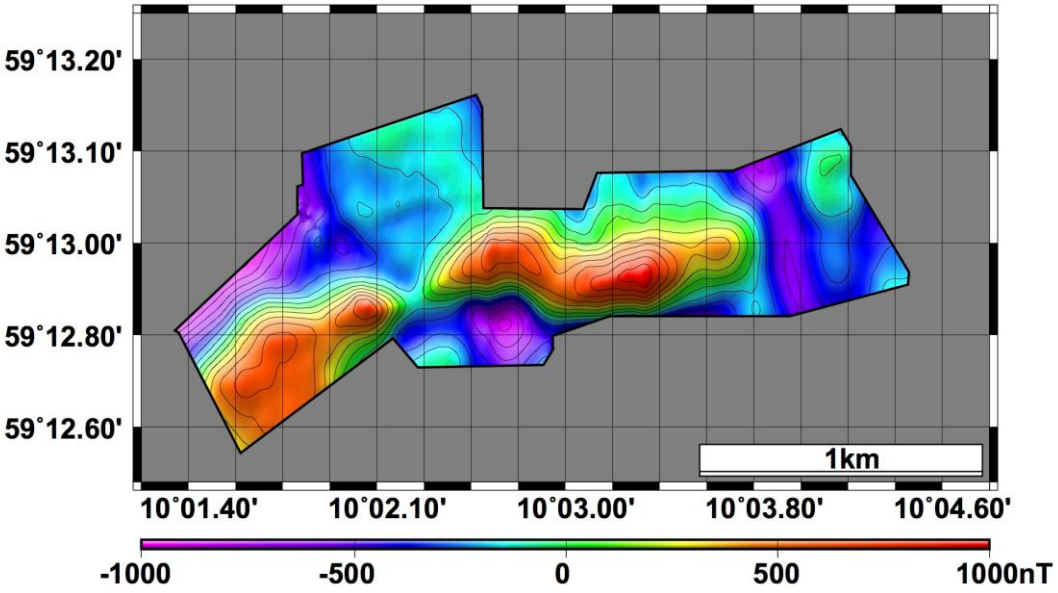

Figure 34: Final magnetic anomaly over the Kodal II area after having removed all the transit lines between the take off point and the survey area and micro-levelled the data.

The total field anomaly data were split into lines and then were gridded using a minimum curvature method with a grid cell size of 10 meters. This cell size is a third of the 30 meters average line spacing for the main survey area. For the high-resolution data, the cell size is exactly half of the route spacing. The micro-levelled data were later gridded using minimum curvature algorithm (Fig. 34).

4.2.3 Siljan-Kåsemyrene

The last drone survey of this report took place in the Siljan-Hvarnes intrusion, at the Fe-Ti-P-(REE) Kåsemyrene occurrence (Fig. 31).

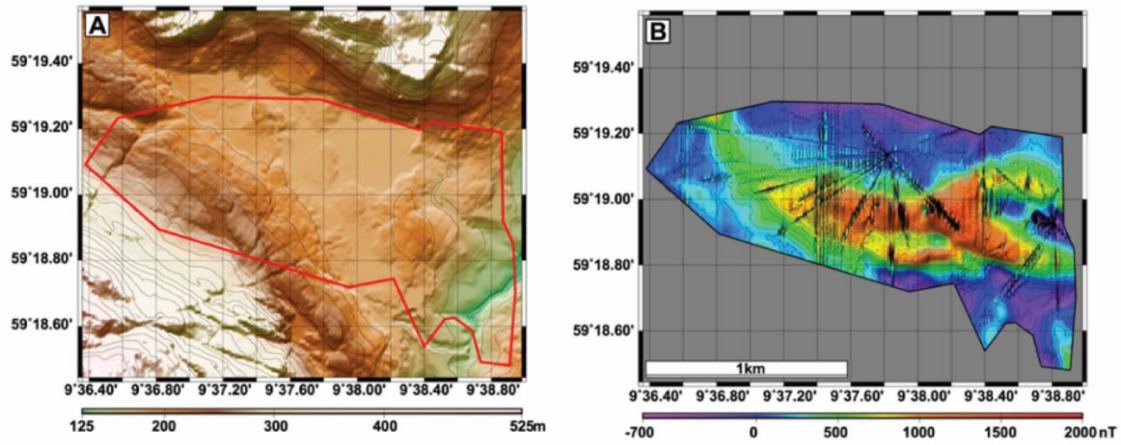

Figure 35: (A) Topography and (B) Raw magnetic anomaly over the Siljan area. As in Kodal II the transit lines can be seen. These lines are removed during the processing.

The processing of the data was similar to what was done in Kodal and Kodal II. The topography of the area and the unprocessed magnetic data are displayed on figures 35A & B respectively. The survey area was located in a local topographic low flanked by a steep cliff on the northern side and hills on the southern side.

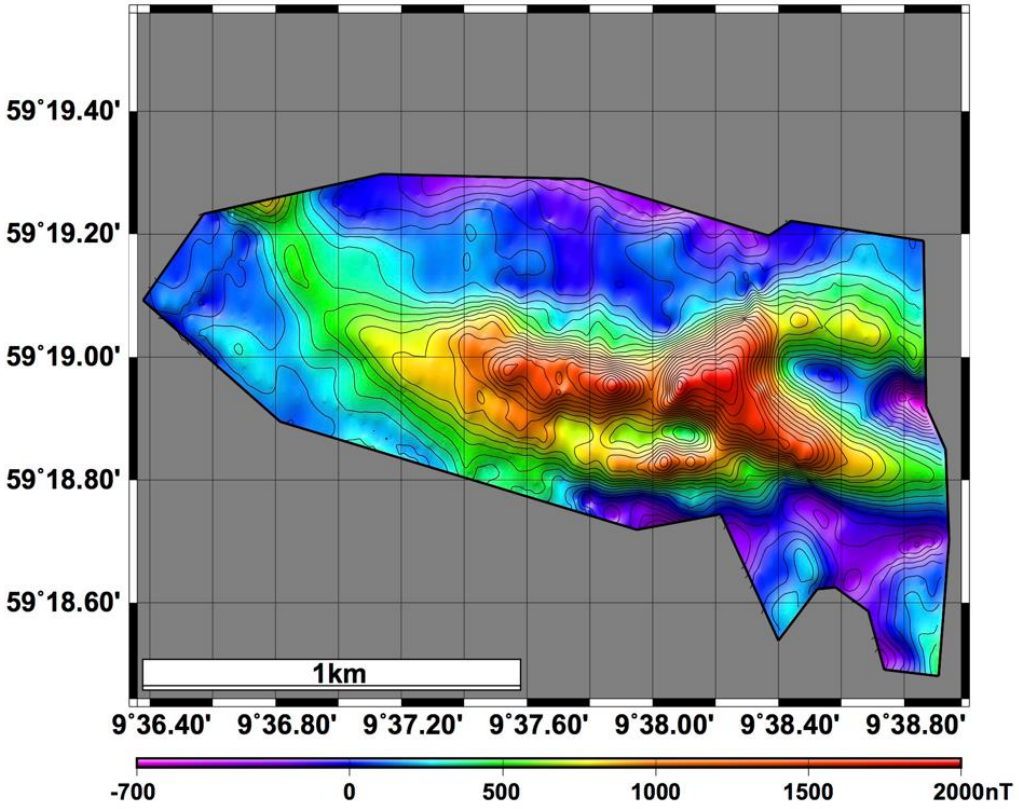

Figure 36: Processed magnetic anomaly over the Kåsemyrene occurence. All the transit lines have been removed, as well as the IGRD and the magnetic anomaly has been micro-levelled.

As for Kodal II, the flight lines were in the N-S direction and the altitude above the ground was set at 35 m. The total distance flown was 200 km and the average speed was 3 m/s. The frequency of the magnetic data acquisition was 5 ms. The processed magnetic anomaly is displayed on figure 36.

4.2.4 Summary

The three drone surveys conducted over the Kodal area and Kåsemyrene (Siljan-Hvarnes intrusion) area have significantly enhanced both data acquisition methods and the understanding of the mineralisation geometries. As the first-ever drone deployment undertaken at NGU, the 2021 survey served as a proof of concept, demonstrating the efficiency and reliability of drones for high-resolution geophysical data acquisition. Subsequent surveys benefited from refinements in flight geometry, notably through the integration of more

advanced software to better follow the topography and maintain a consistent wavelength content in the signal. These deployments represent a milestone in NGU's technological advancements, improving both the efficiency and cost-effectiveness of data acquisition procedures.

These data contribute to major scientific and industrial challenges, such as understanding the evolution of Earth's geomagnetic field and assessing the mining potential of mineralized zones. The success of these initial deployments has led to numerous subsequent drone surveys across Norway, and drones are now an integral part of NGU's annual summer fieldwork campaigns.

4.3 Soil Geochemical survey

Soil geochemical surveys are essential tools in mineral exploration, offering critical insights into the dispersion of elements associated with ore deposits (e.g., Kyser et al., 2015). In Fennoscandia, soils are often comprised by till (i.e., surficial sediments deposited by glaciers), which result from glacial erosion, entrainment, transportation, and depositional processes (i.e. glacial ice movement) where bedrock is the main source (McClenaghan et al. 2021). Till deposit covers most of the northern hemisphere (McMartin and McClenaghan 2001) and thus, local and regional-scale sampling of this media is effective for mineral exploration in glaciated terrain. The application of till geochemical studies as a vector for bedrock mineralisation has been a successful tool for many mineral deposit discoveries (e.g. Canada, Plouffe et al. 2022; Plouffe et al. 2012).

By analysing soil samples for major and trace elements, we can detect surface anomalies that may signal the surficial expression of mineralized systems at depth. This method is both cost-effective and minimally invasive compared to traditional drilling, making it a valuable approach for early-stage exploration.

In this study, we assess the effectiveness of soil geochemistry in detecting Fe-Ti-P-(REE) mineralisation by carrying out a geochemical transect across the contact between the host monzonite/syenite and mineralized zones within the Kåsemyrene area, hosted by the western part of the Siljan-Hvarnes intrusion (Fig. 37; Chapters 3.3.1 and 4.2.3). We implement systematic field sampling and quantification procedures to evaluate element dispersion patterns, potential enrichment zones, and the relationships between soil chemistry and bedrock

mineralisation. The results will provide insights into the applicability of soil surveys for Fe-P-REE exploration and contribute to refining geochemical exploration models for similar geological settings.

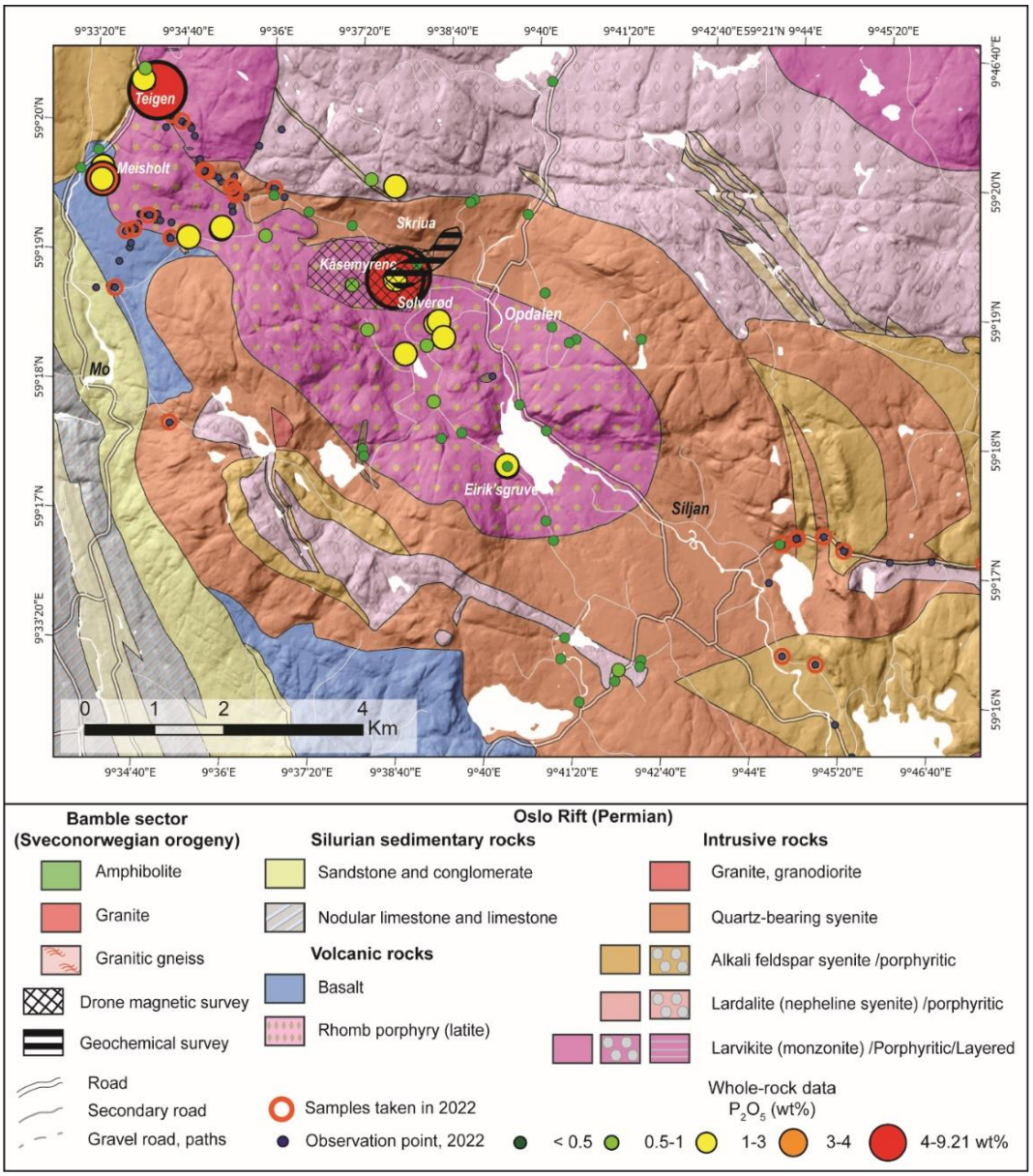

Figure 37: Geologic map of the western part of the Siljan-Hvarnes intrusion. Locations of the magnetic drone and soil geochemical surveys over the Kåsemyrene occurrence are shown.

The heterogeneous nature of the Fe-Ti-P-(REE) mineralisation in the southern Oslo rift, and the glaciated nature of the area, pose significant challenges for mineral exploration. On one hand, the mineralisation consists of centimetre to meter wide titanomagnetite–apatite–ilmenite-clinopyroxene-rich pockets irregularly distributed within <1 km^2 areas hosted by monzonite/larvikite. On the other hand, till deposits are not derived from in-situ weathering of the underlying bedrock but instead result from glacier transport. In Fennoscandia, glacier

transport can vary from a few meters to several kilometres which can then mask the location of mineralized bedrock. In the Kåsemyrene area, ice transport and direction (i.e., glacier movement direction) are poorly constrained. Thus, a soil survey transect was carried out to assess whether secondary dispersion of ore minerals (i.e., their geochemical fingerprint) can be traced in the overlying soil material (i.e., till). Given the magnetite-rich nature of the mineralisation, the survey not only included a geochemical characterization of soil, but also magnetic susceptibility measurements were taken on the same sample batch. In addition, field and laboratory measurements were taken to further assess cost effective approaches for soil anomaly identification in the area. In this chapter, we present the results of the survey and evaluate the proficiency of the soil geochemical and geophysical properties as vectors for mineral exploration.

4.3.1 The Siljan area

Siljan (Fig. 37) was the chosen survey area as several P-Fe-Ti-REE occurrences have been recorded here and it is also highlighted by the regional mineral potential mapping (MPM) study (Fig. 22 & 24B) as an extensive prospective area (see chapter 4.1).

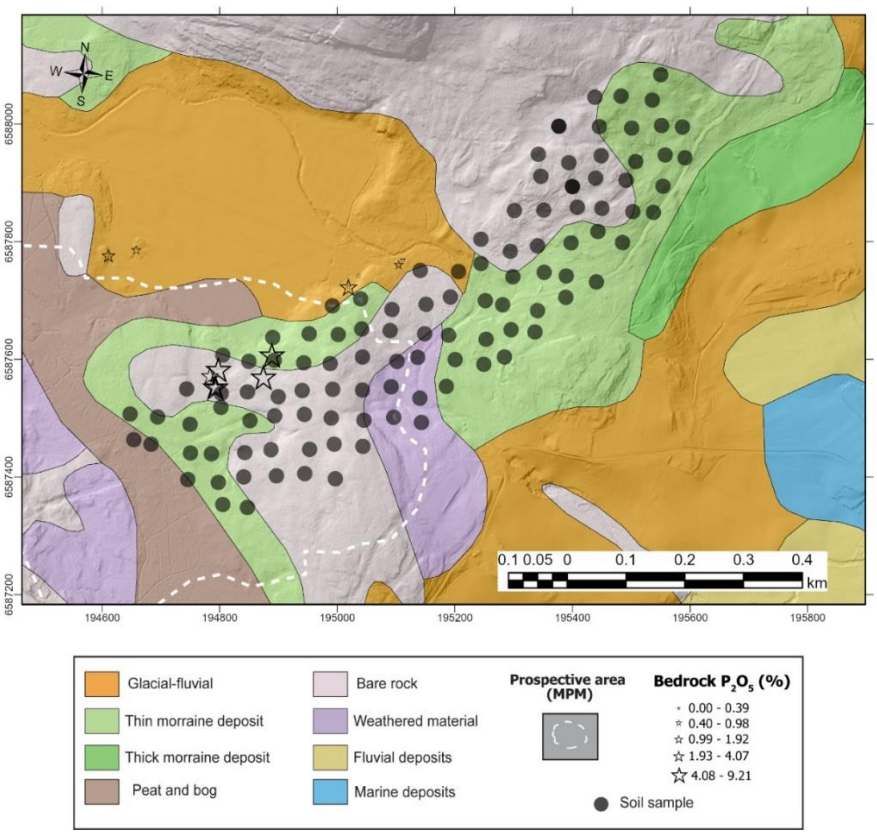

Figure 38: Quaternary geology map of the eastern part of the Kåsemyrene occurrence. The transects soil sample locations are shown as black points. The white dashed line corresponds with the contour of the location of Siljan's prospective area indicated by the mineral potential mapping (MPM) study (see chapter 4.1)

The Quaternary map shows that this area is mainly covered by moraine deposits, sediments derived from weathering and glaciofluvial processes, and bare rock (Fig. 38). However, during the field campaign it was noticed that till deposits are found throughout the surveyed area. The dominant geological units in Kåsemyrene-Siljan are quartz-monzonite and monzonite (Fig. 37), locally porphyritic (see chapter 3), with monzonite hosting several Fe-Ti-P-(REE) occurrences (Fig. 9 & 37; chapter 3.3).

4.3.2 Sampling methods

A NE-trending transect with a 50 m x 50 m resolution was designed to cross over areas outside and inside the highly prospective zone identified by the regional MPM (see chapter 4.1). The sample media was the C-horizon from areas covered by till sediments (moraine deposits). Areas containing glaciofluvial and marine deposits were excluded from the survey. Sample pits were dug by paint-free steel shovels down to the mineral soil layer. In locations where the soil profile was thin, till sediments and weathered rock material were mixed. Samples were transferred into Rilsan® plastic bags using a small steel shovel (Flem et al. 2020). Every 10^{th} sample, a field duplicate was taken ($n= 9$). After collection, the samples' wet weight was recorded and then these were air-dried at temperatures of 20 - 40 °C for more than 3 months. These were subsequently dry-sieved using a 2 mm nylon mesh. For each sample a 50 ml Kautex box was filled using a stainless-steel spoon. The remaining < 2mm sieved fraction was filled back into the sample bag and stored for future use. The >2 mm fraction was discarded.

4.3.3 Analytical methods

Geochemical and magnetic susceptibility analyses were carried out on the collected soil material, both in the lab and in the field. To reduce the uncertainty associated with field measurements, all of these were done in sequence following the same protocol at the end of each working day. The field measurements were carried out by placing the sensors for both instruments (magnetic susceptibility meter and portable XRF) on top of the soil material transferred to the plastic bag.

4.3.3.1 Magnetic susceptibility

Field measurements were taken with a SM30 magnetic susceptibility meter (ZH instruments) using the interpolation mode (mode 3). The instrument has a sensitivity (lowest measurement capable of recording) of 1×10^{-7} SI and it has a surface of integration of 50 mm diameter. Each

soil sample analysis (2 s) was bracketed by two 2 s analyses of blank (instrument targeting the air) for instrument drift correction.

The laboratory measurements were made at NGU's facilities directly on the sieved soil material contained in the Kautex boxes (same material subject to geochemical analysis) using a Bartington MS3/MS2K system. The instrument has a sensitivity of 1 x 10^{-6} SI. This sensor is designed to take measurements on flat and smooth surface and has a surface of integration (spot size) of ca. 25.4 mm diameter. Amplitude changes of a low-frequency magnetic field measured by the MS3 with a magnetic susceptibility (MS) achieve a resolution of 2 μSI. Each sample measurement was conducted as follows: One analysis of a disk-shaped reference material (provided by Bartington instruments) was performed every ten samples, then 1 successive analysis of the sample lasting 0.1 s each were bracketed by two 0.1 s analyses of blank (gun targeting the air) for instrument drift correction.

4.3.3.2 Geochemistry

Major and trace element measurements were taken in the field using a Niton XL5 portable XRF. The instrument carries out spot analysis using an 8 mm diameter sensor. For this study, the Mining calibration model ("Mining Profile") was implemented so that each measurement lasted ca. 2 minutes. A total suite of 15 elements were systematically quantified with the portable XRF (Si, P, S, Al, Fe, Ca, Rb, Sr, Zr, Nb, Ba, La, Ce, Pr, Nd).

Quantification for major and trace element was carried at the NGU facilities. Major element concentrations (SiO_2, Al_2O_3, Fe_2O_3, TiO_2, MgO, CaO, Na_2O, K_2O, MnO, P_2O_5) were obtained from fused glass pellets using a S8 Tiger 2nd generation XRF (4 KW Rh-X-ray tube). The glass pellets were made by fusing a mixture of 0.6 grams of the soil sample with 4.2 g of lithium tetraborate ($Li_2B_4O_7$; i.e., total concentration quantification). The same glass pellets were analysed for trace elements (Be, Rb, Sr, Y, Zr, Nb, Sn, Cs, Ba, La, Ce, Pr, Nd, Sm, Eu, Gd, Tb, Dy, Ho, ER, Tm, Yb, Lu, Hf, Ta, W, Pb, Bi, Th, U, V, Cr, Cu, Zn, Ga) by LA-ICP-MS, using an Agilent 8900 triple-quadrupole ICP-MS coupled to an Analyte Excite 193 nm excimer laser system from Teledyne-Cetac-Photon Machines. Trace elements were also analysed from pressed pellets at the S8 Tiger XRF.

4.3.4 Results

4.3.4.1 Magnetic susceptibility

The magnetic susceptibility measurements taken with both instruments showed a spread over three orders of magnitude indicating significant variability associated with changes of the soil's magnetic composition.

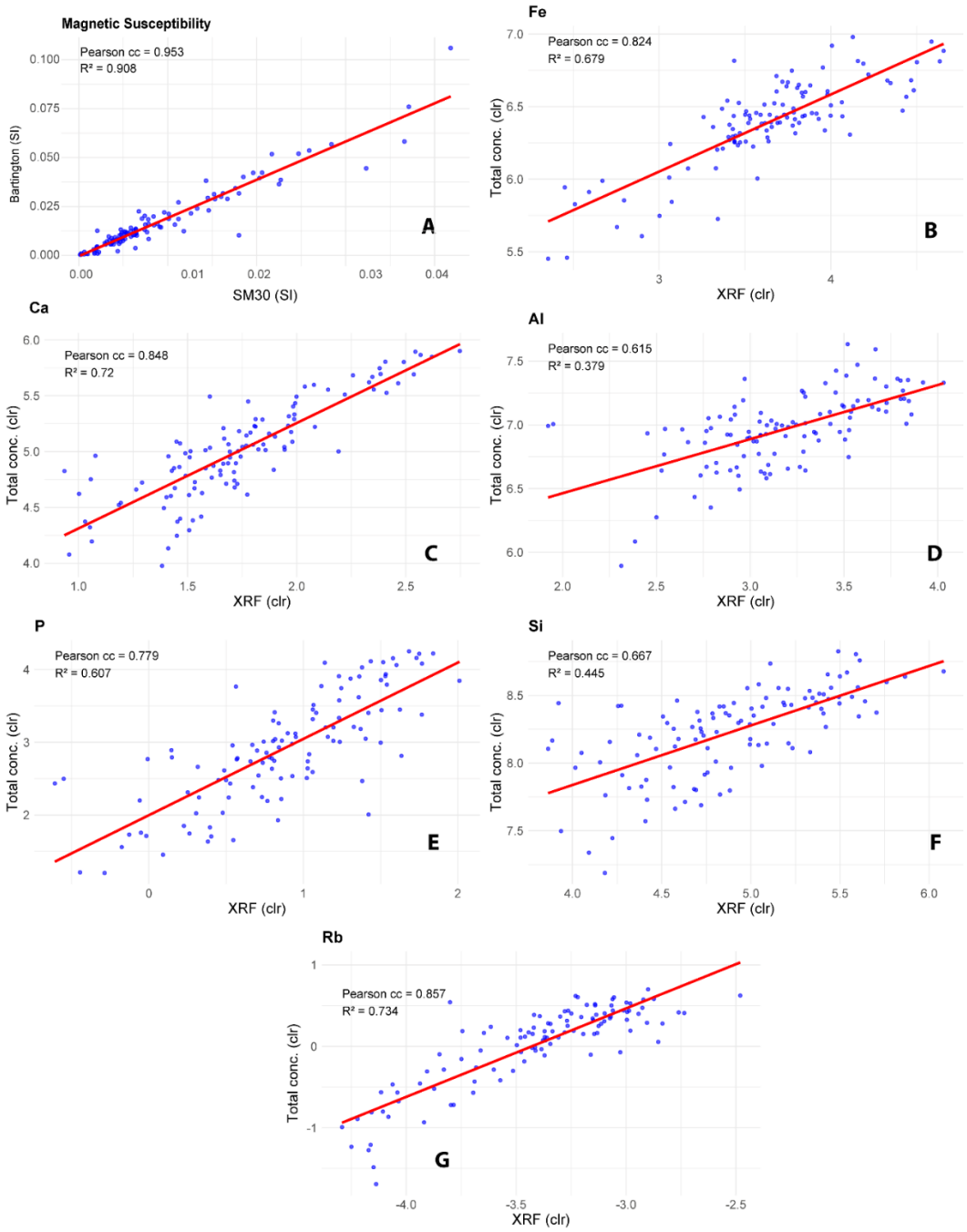

Figure 39: Scatter plots showing correlation between portable XRF (un-sieved samples) and total concentration (Total conc.; sieved samples) method carried out at NGU laboratory as well as magnetic susceptibility measurements taken on un-sieved (field measurements done with SM30) and sieved (laboratory measurements taken with the Bartington MS3/Ms2K system) material. Note that raw concentrations have been transformed to center-log ratios (clr).

In both cases, the ordinary versus field duplicate sample plots show low correlation indicating a high magnetic variability of the soil even within the same sample site (Appendix C). However, this variability could also be amplified by the grain size heterogeneity of the sample.

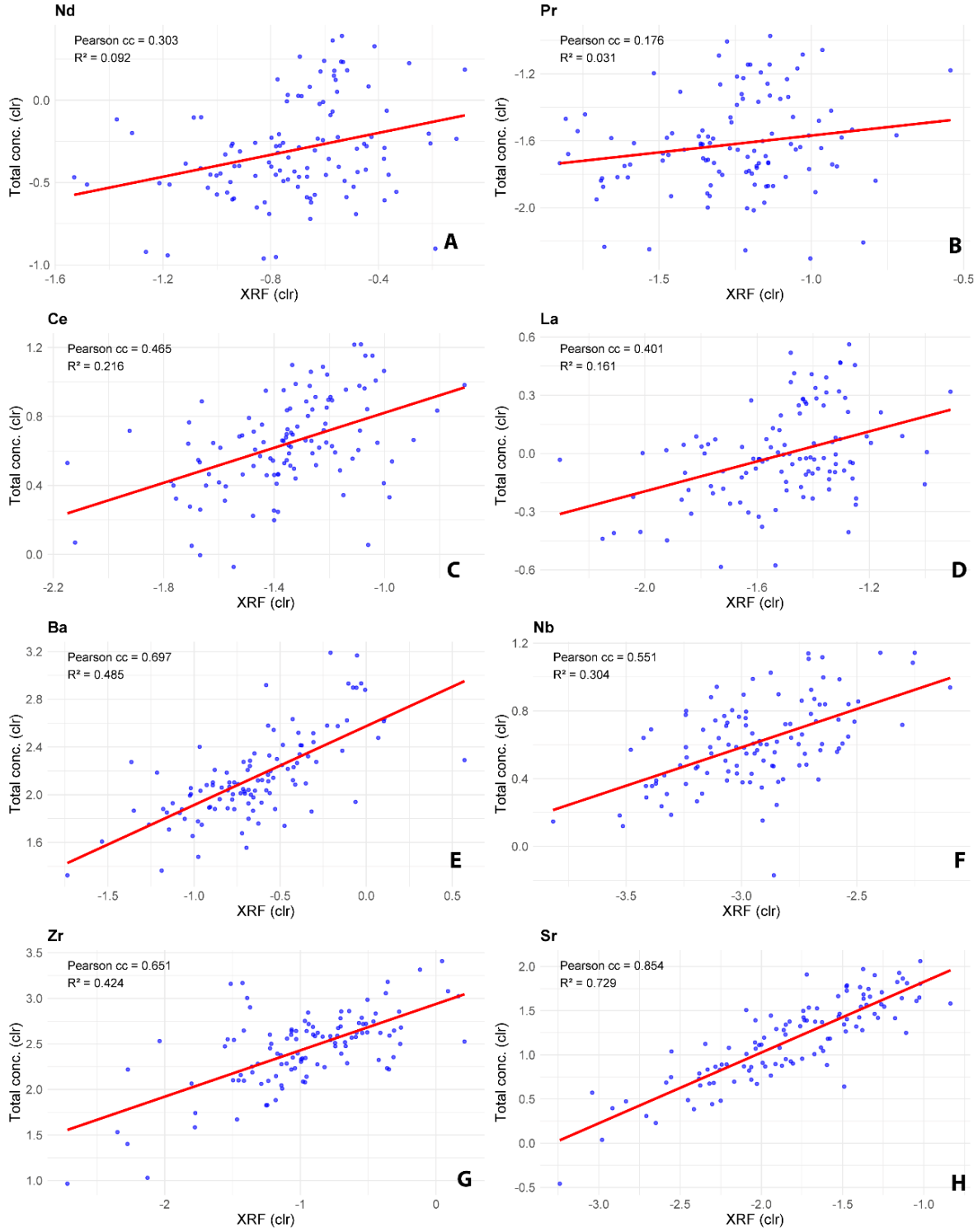

Figure 40: Scatter plots showing correlation between portable XRF (un-sieved samples) and total concentration (Total conc.; sieved samples) method carried out at NGU laboratory. Note that raw concentrations have been transformed to center-log ratios (clr).

For the in-house magnetic susceptibility measurements using the Bartington MS3/MS2K system, the reference material shows good reproducibility as it yields average and median values of 402 x 10^{-5} µSI and 406 x 10^{-5} µSI, and standard deviation of 2.0 x 10^{-5} µSI. These results indicate that there was only a -0.81% and -0.73% offset from manufacturer reference value (Appendix C). Notably, the correlation between both instrument measurements is very high as it achieved a R^2 of 0.91 and Pearson correlation coefficient (cc) of 0.95 (Fig. 39A).

4.3.4.2 Geochemistry

The overall quality assurance (Appendices D and E) of the portable XRF and laboratory geochemical quantifications is satisfactory.

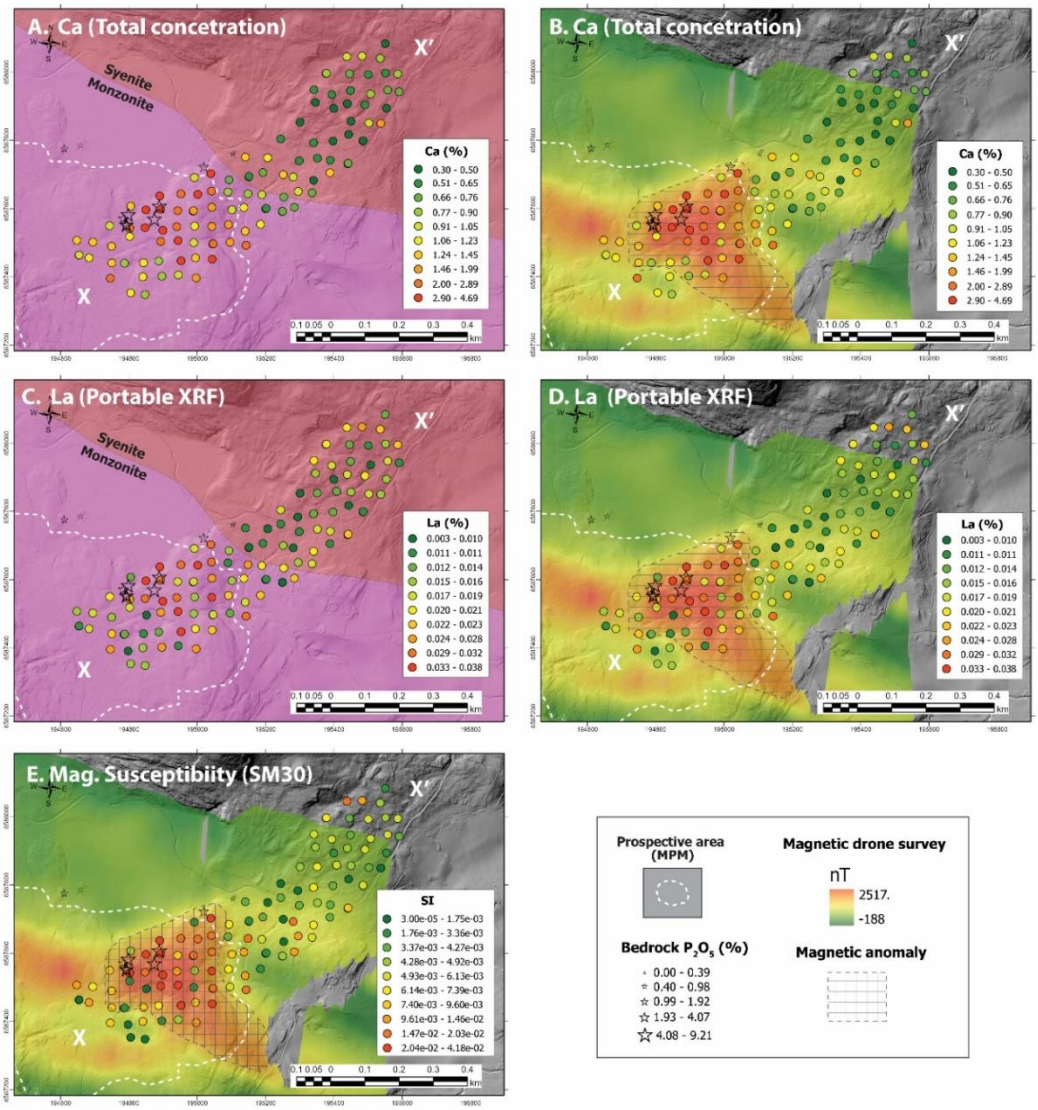

Figure 41: Results from the geochemical survey for Ca and La contrasted against the bedrock map (A, C) and the magnetic drone survey (B, D). In E, are displayed the field magnetic susceptibility measurements over the magnetic drone survey. The X-X' describes the trend (N38°E) of the profiles presented in figure 42.

Ordinary versus duplicate sample plots for elements quantified by both methods achieve Pearson cc >0.6 for several elements indicating fair reproducibility within the same sampling site (Appendices D and E**)**.

The same is true for the rest elements quantified by the total concentration method (Appendix F). In addition, element concentrations that were obtained in the field and in the NGU laboratory, display Pearson cc mostly between 0.6 to 0.9, except for Nd. Pr, Ce, and La which are ≤0.6 (Figs. 39 & 40).

4.3.4.3 Spatial context of the soil survey results

Figures 41 and 42 illustrate plan and profile views of selected element concentrations and magnetic susceptibility data from the soil survey.

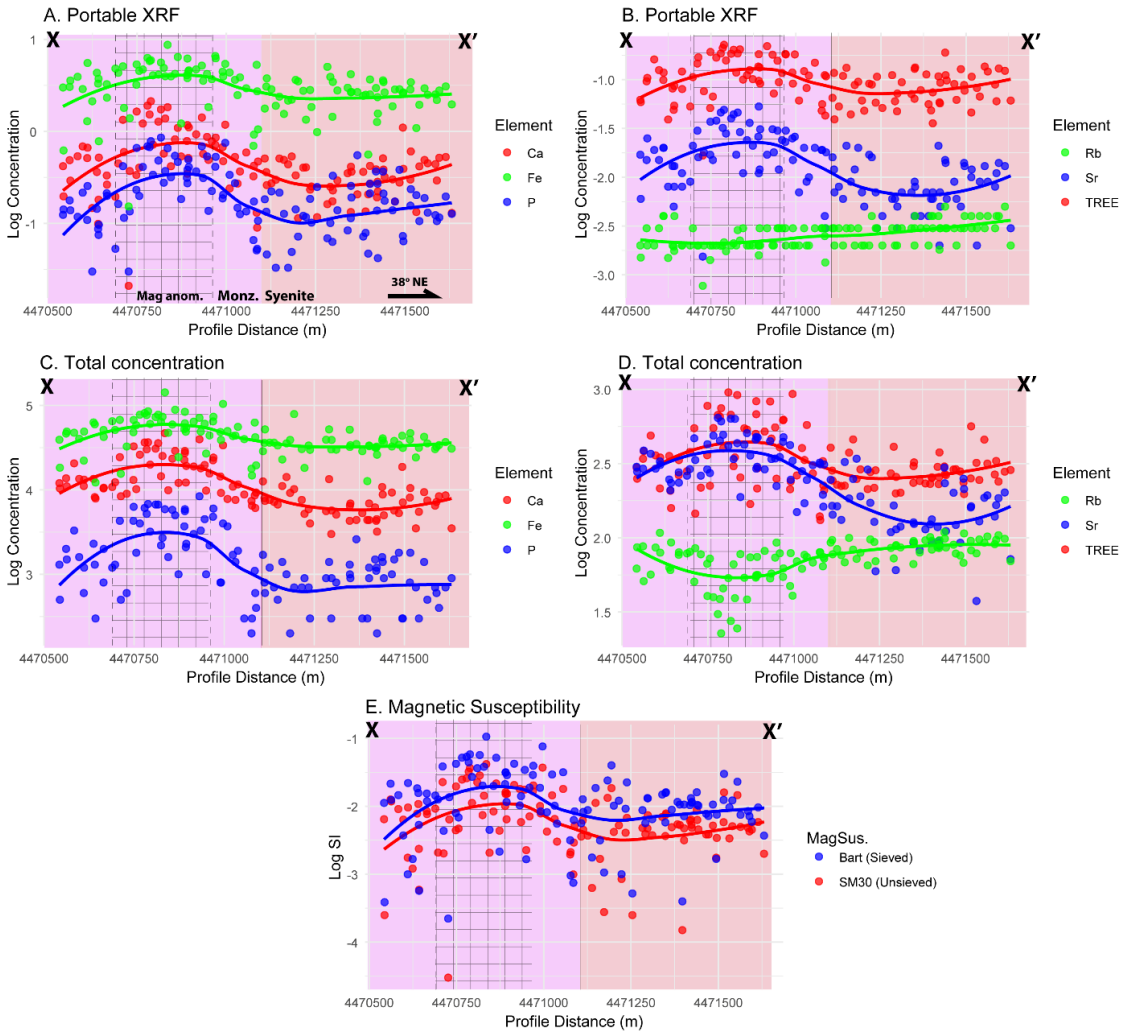

Figure 42: Geochemical profiles projected along a 38°NE trend (see figure 41) showing concentration variability for major and trace elements measured in the field (portable XRF) and NGUs laboratory (Total concentration) and magnetic susceptibility. Note that in all cases the enrichment or depletion (e.g. Rb) of the selected elements coincide with the occurrence of the magnetic drone anomaly. The regression line was calculated using the local regression method (i.e., LOESS method)

We have also added the local lithology and magnetic drone survey map to provide a spatial context to the results.

Higher values of Ca and La (as a proxy for REE) are located within the monzonite but close to its contact with the syenite (Fig. 42A & 42C). Moreover, these elevated concentrations are clustered within the magnetic high indicated by the drone survey (Fig. 41B-D), and they decrease as the transect crosses the anomaly. Geochemical profiles done along the transect (Fig. 42A-D) further show the consistent spatial correlation among the airborne magnetic high, Ca-P-Fe (major elements), and Sr-TREE (total rare earth elements) and magnetic susceptibility. Although noisier than the geochemical vectors, magnetic susceptibility was also able to successfully detect the drone magnetic anomaly (Figs. 41E & 42E). Notably, it was recognized that Rb and K (not shown) concentrations systematically decrease as they approach the magnetic anomaly (Fig 42B, D). In general, our results indicate that soil composition preserved on top of the drone magnetic anomaly is dominated by Ca-P-rich and Fe-rich magnetic minerals such as apatite and magnetite, respectively. Furthermore, monzonite's content of primary K (and Rb) hosted mainly in feldspar (K-feldspar) declines as magnetite-apatite-ilmenite mineralisation takes over (Chapter 3.3). This gives the southern Oslo Rift mineralized bedrock a distinctive low K and high magnetic signature, which we demonstrate in this contribution, it is also preserved in the overlying till sediments.

4.3.5 Implications for mineral exploration

- Despite the apparent heterogenous nature of the P-Fe-Ti-P-REE mineralisation, the 50 m x 50 m survey was able to successfully identify mineralisation at Siljan, which is also highlighted by a magnetic high indicated by the drone survey.
- Results from field and laboratory analyses for major and trace elements, and magnetic susceptibility measurements are largely correlated indicating that field measurements done with the portable XRF and SM30 magnetic susceptibility meter can successfully detect P-Fe-Ti-P-REE mineralisation.
- Depletions in K and Rb at the expense of increasing Ca-P-Fe in soil are consistent with the nature of the mineralized rocks (magnetite-apatite-ilmenite rich) hosted by the larvikite/monzonite (K-Rb rich).
- The strong spatial correlation between Ca-P-Sr-REE in soil and local mineralisation suggests limited ice transport in this area so that the overlying till material preserves a relatively equivalent geochemical signature to that of the underlying bedrock.

5. HIGHLIGHTS AND CONCLUSIONS

In this chapter we summarize the conclusions associated with the different chapters of this report and the key features associated with Fe-Ti-P-(REE) mineralisation in the southern part of the Oslo rift. In addition, we highlight the potential tools that can be used to assess the prospectivity of the area.

- Intermediate to felsic alkaline rocks from the southern part of the Oslo rift host Fe-Ti-P-REE and HFSE mineralisation.
- Fe-Ti-P and Zr-Nb-REE occurrences and deposits are found in areas where two magmas mixed (mingling zones). Mineralisation can also be found at the contact between the B1 basalts or basaltic xenoliths and syenite (Hesterønningane). Mineralisation occurs where the magma underwent a sudden change in chemistry, temperature or potentially also pressure.
- Monzonite and monzodiorite are more likely to host Fe-Ti-P-mineralisation. As with as Kodal I, these can get large enough to be considered as deposits. Apatite in these rocks contain a total amount of REO around 1 -1.5 wt% in Kodal I and 1.5-3.2 wt% TREO in Kåsemyrene.
- Zr-Nb-REE occurrences are smaller in size and concentrate elements usually more common in felsic magmas. They are hosted in evolved monzonite or syenite.
- The most enriched samples in Nb, Zr and REE are pegmatites from Haukaråsen which are hosted by a syenite.
- Machine learning is a powerful new tool that can be used to assess the prospectivity of entire regions, integrating available geological datasets. A good understanding of the geology and petrogenesis of the mineralisation is necessary to interpret the results.
- Fe-Ti-P-(REE) mineralisation are associated with positive magnetic anomalies, although the strong remanence of the samples should be considered as it can considerably weakens the signature. For the same reason, large negative anomalies should not be discarded.
- Drone magnetic surveys provide detailed magnetic data, which in the case of Fe-Ti-P-(REE) mineralisation are a crucial step toward targeted mineral exploration.

- Soil surveys can be used as a mineral exploration tool to locate Fe-Ti-P-(REE) occurrences. Geochemical and magnetic property variations can be picked up using field equipment such as portable XRFs and magnetic susceptibility meters.
- The Kåsemyrene occurrence is likely larger than just the small excavation 2 pits that were sampled, based on the three prospective methods used in this project. Drilling is necessary to further assess the extent of the mineralisation.

ACKNOWLEDGMENTS

This project was funded by the Geological Survey of Norway and Treschow-Fritzøe. This report compiles the work of a master student, Marius Schølberg (University of Science and Technology – NTNU, Trondheim, Norway), and of a PhD student, Pierre Buelens (University Libre de Bruxelles, Belgium). We wish to thank for their contribution to the project. In addition, we would like to thank our colleagues from the Laboratorium at NGU who made this geochemical-intensive project possible. We would like to thank Malin Andersson and Tor Erik Finne for their assistance planning the soil geochemical survey and Iain Henderson for helping with sampling. We greatly appreciated working in collaboration with Tord Andersen, region geologist of Vestfold. Finally, we would like to thank Enzo Caraballo Rojas from the Université de Laval in Québec, Canada who performed the microprobe analyses.

Isotopic analyses for this study were performed in the MiMaC laboratory, supported by the Research Council of Norway project number 269842/F50.

REFERENCES

Al-Chalabi M (1971) Some Studies Relating To Nonuniqueness In Gravity And Magnetic Inverse Problems. Geophysics 36:835-855. doi: 10.1190/1.1440219.

Alken P, Thébault E, Beggan CD, Amit H, Aubert J, Baerenzung J, Bondar TN, Brown WJ, Califf S, Chambodut A, Chulliat A, Cox GA, Finlay CC, Fournier A, Gillet N, Grayver A, Hammer MD, Holschneider M, Huder L, Hulot G, Jager T, Kloss C, Korte M, Kuang W, Kuvshinov A, Langlais B, Léger JM, Lesur V, Livermore PW, Lowes FJ, Macmillan S, Magnes W, Mandea M, Marsal S, Matzka J, Metman MC, Minami T, Morschhauser A, Mound JE, Nair M, Nakano S, Olsen N, Pavón-Carrasco FJ, Petrov VG, Ropp G, Rother M, Sabaka TJ, Sanchez S, Saturnino D, Schnepf NR, Shen X, Stolle C, Tangborn A, Tøffner-Clausen L, Toh H, Torta JM, Varner J, Vervelidou F, Vigneron P, Wardinski I, Wicht J, Woods A, Yang Y, Zeren Z, Zhou B (2021) International Geomagnetic Reference Field: the thirteenth generation. Earth, Planets and Space 73:49. doi: 10.1186/s40623-020-01288-x.

Andersen T, Seiersten M (1994) Deep cumulates in a shallow intrusion- origin and crystallization history of a pyroxenite (jacupirangite SL) body in the Larvik pluton, Oslo Region, South Norway. Neues Jahrbuch Fur Mineralogie-Monatshefte:255-274.

Andersen T, Frei R, Sørensen H, Langager Westphal N (2004) Porphyritic syenite at Lake Mykle, the Oslo Rift- a possible derivative of larvikite. NGU Bulletin 442:23-28.
Andersen T, Erambert M, Larsen AO, Selbekk RS (2010) Petrology of Nepheline Syenite Pegmatites in the Oslo Rift, Norway: Zirconium Silicate Mineral Assemblages as Indicators of Alkalinity and Volatile Fugacity in Mildly Agpaitic Magma. Journal of Petrology 51:2303-2325. doi: 10.1093/petrology/egq058.
Andersen T, Erambert M, Larsen AO, Selbekk RS (2013) Petrology of nepheline syenite pegmatites in the Oslo Rift, Norway: Zr and Ti mineral assemblages in miaskitic and agpaitic pegmatites in the Larvik Plutonic Complex. Mineralogia 44:61-98.
Andersen TE (2021) Petrogenesis of Fe-Ti-P rich rock in the Siljan-Hvarnes Intrusion, S.E. Norway Institutt for geovitenskap og petroleum. NTNU, pp 134.
Baranov V (1957) A new method for interpretation of aeromagnetic maps: pseudo-gravimetric anomalies. Geophysics 22:359-382.
Baranwal V (2013) Compilation of various airborne geophysical data in the Oslofjord area NGU report. Geological Survey of Norway, pp 38.
Bergstøl S (1972) The jacupirangite at Kodal, Vestfold, Norway, a potential magnetite, ilmenite and apatite ore. Miner Depos 7:233-246.
Bingen B, Nordgulen O, Viola G (2008) A four-phase model for the Sveconorwegian orogeny, SW Scandinavia. Norwegian Journal of Geology 88:43-72.
Blakely RJ (1995) Potential Theory in Gravity and Magnetic Applications. Cambridge University Press, Cambridge.
Blakely RJ (1996) Potential theory in gravity and magnetic applications. Cambridge university press.
Bowell RJ, Chapman C, McDougall C, Martindale R, Pittbuck M (2021) Preliminary economic assessment of Norra Kärr Rare Earth deposit and potential biproducts, Sweden In: consulting S (ed). pp 275.
Breiman L (2001) Random forests. Machine learning 45:5-32.
Buelens P, Debaille V, Decrée S, Coint N, Mansur E (2024) Multi-stage evolution of the monzonitic Larvik Plutonic Complex (Oslo Rift, Norway) and its implications for the formation of the Kodal Fe-Ti-P(−REE) deposit. Lithos 484-485:107743. doi: https://doi.org/10.1016/j.lithos.2024.107743.
Cande SC, Kent D (1995) Revised calibration of the geomagnetic polarity timescale for the Late Cretaceous and Cenozoic. Journal of Geophysical Research: Solid Earth 100:6093-6095.
Charlier B, Sakoma E, Sauvé M, Stanaway K, Auwera JV, Duchesne J-C (2008) The Grader layered intrusion (Havre-Saint-Pierre Anorthosite, Quebec) and genesis of nelsonite and other Fe–Ti–P ores. Lithos 101:359-378. doi: http://dx.doi.org/10.1016/j.lithos.2007.08.004.
Charlier B, Grove TL (2012) Experiments on liquid immiscibility along tholeiitic liquid lines of descent. Contrib Mineral Petrol 164:27–44. doi: 10.1007/s00410-012-0723-y.
Charlier B, Namur O, Bolle O, Latypov R, Duchesne JC (2015) Fe-Ti-V-P ore deposits associated with Proterozoic massif-type anorthosites and related rocks. Earth-Science Reviews 141:56-81. doi: 10.1016/j.earscirev.2014.11.005.
Chawla NV, Bowyer KW, Hall LO, Kegelmeyer WP (2002) SMOTE: synthetic minority over-sampling technique. Journal of artificial intelligence research 16:321-357.
Clark DA (2014) Methods for determining remanent and total magnetisations of magnetic sources – a review. Exploration Geophysics 45:271-304. doi: 10.1071/EG14013.
Coint N, Keiding JK, Ihlen PM (2020) Evidence for Silicate–Liquid Immiscibility in Monzonites and Petrogenesis of Associated Fe–Ti–P-rich rocks: Example from the Raftsund Intrusion, Lofoten, Northern Norway. Journal of Petrology 61. doi: 10.1093/petrology/egaa045.
Coint N, Mansur E, Keiding JK, Skår Ø (2023) Trace elements in ilmenite, titanomagnetite and apatite unravel the petrogenesis of Fe-Ti-P (+/-Zr) rich rocks and associated nelsonite from the Raftsund intrusion, Vesterålen-Lofoten AMCG suite, Northern Norway. Lithos:107389. doi: https://doi.org/10.1016/j.lithos.2023.107389.
Corfu F, Dahlgren S (2008) Perovskite U–Pb ages and the Pb isotopic composition of alkaline volcanism initiating the Permo-Carboniferous Oslo Rift. Earth and Planetary Science Letters 265:256-269. doi: https://doi.org/10.1016/j.epsl.2007.10.019.
Cortes C, Vapnik V (1995) Support-vector networks. Machine learning 20:273-297.
Dahlgren S, Corfu F (2001) Northward sediment transport from the late Carboniferous Variscan Mountains: zircon evidence from the Oslo Rift, Norway. Journal of the Geological Society 158:29-36.

Decrée S, Coint N, Debaille V, Hagen-Peter G, Leduc T, Schiellerup H (2023) The potential for REEs in igneous-related apatite deposits in Europe. Geological Society, London, Special Publications 526:SP526-2021-2175. doi: doi:10.1144/SP526-2021-175.
Dentith M, Mudge ST (2014) Geophysics for the mineral exploration geoscientist. Cambridge University Press.
Dymek RF, Owens BE (2001) Petrogenesis of Apatite-Rich Rocks (Nelsonites and Oxide-Apatite Gabbronorites) Associated with Massif Anorthosites. Economic Geology 96:797-815. doi: 10.2113/gsecongeo.96.4.797.
Dyment J, Szitkar F, Levaillant D (2018) Ridge propagation, oceanic core complexes, and ultramafic-hosted hydrothermalism at Rainbow (MAR 36°N): Insights from a multi-scale magnetic exploration. Earth and Planetary Science Letters 502:23-31. doi: https://doi.org/10.1016/j.epsl.2018.08.054.
Emslie RF (1975) Major rock units of the Morin Complex, southwestern Quebec. Geological Survey of Canada Paper 74-48:37.
Flem B, Andersson M, Finne TE, Minde Å (2020) Mineral soil geochemistry in southern Trøndelag In: Norway GSo (ed). Geological Survey of Norway, pp 127.
Goodenough KM, Schilling J, Jonsson E, Kalvig P, Charles N, Tuduri J, Deady EA, Sadeghi M, Schiellerup H, Muller A, Bertrand G, Arvanitidis N, Eliopoulos DG, Shaw RA, Thrane K, Keulen N (2016) Europe's rare earth element resource potential: An overview of REE metallogenetic provinces and their geodynamic setting. Ore Geology Reviews 72:838-856. doi: 10.1016/j.oregeorev.2015.09.019.
Harris JR, Naghizadeh M, Behnia P, Mathieu L (2022) Data-driven gold potential maps for the Chibougamau area, Abitibi greenstone belt, Canada. Ore Geology Reviews 150:105176.
Honsho C, Dyment J, Tamaki K, Ravilly M, Horen H, Gente P (2009) Magnetic structure of a slow spreading ridge segment: Insights from near-bottom magnetic measurements on board a submersible. Journal of Geophysical Research: Solid Earth 114.
Honsho C, Ura T, Tamaki K (2012) The inversion of deep-sea magnetic anomalies using Akaike's Bayesian information criterion. Journal of Geophysical Research: Solid Earth 117. doi: https://doi.org/10.1029/2011JB008611.
Ihlen PM, Schiellerup H, Gautneb H, Skår Ø (2014) Characterization of apatite resources in Norway and their REE potential — A review. Ore Geology Reviews 58:126-147. doi: http://dx.doi.org/10.1016/j.oregeorev.2013.11.003.
Isezaki N (1986) A new shipboard three-component magnetometer. Geophysics 51:1992-1998.
Jiang L, Li C, Cai Z, Zhang H (2013) Sampled bayesian network classifiers for class-imbalance and cost-sensitive learning 2013 IEEE 25th International Conference on Tools with Artificial Intelligence. IEEE, pp 512-517.
Juliani C, Ellefmo SL (2019) Prospectivity mapping of mineral deposits in Northern Norway using radial basis function neural networks. Minerals-Basel 9:131.
Kieffer MA, Dare SAS, Gendron M (2024) Trace element discrimination diagrams to identify igneous apatite from I-, S- and A-type granites and mafic intrusions: Implications for provenance studies and mineral exploration. Chemical Geology 649:121965. doi: https://doi.org/10.1016/j.chemgeo.2024.121965.
Kodal Minerals P (2017) Group annual report and financial statements for the year ended 31 March 2017. pp 75.
Kragh K, Jensen OA (1991) An immiscible iron-rich liquid in a larvikite magma? GeoSkrifter 38:32-34.
Larsen BT, S. O, B. S, Heeremans M (2008) The Permo-Carboniferous Oslo Rift through six stages and 65 million years. International Union of Geological Sciences 31:52-58. doi: 10.18814/epiiugs/2008/v31i1/008.
Lester GW, Kyser TK, Clark AH, Layton-Matthews D (2013) Trace element partitioning between immiscible silicate melts with H2O, P, S, F, and Cl. Chemical Geology 357:178-185. doi: https://doi.org/10.1016/j.chemgeo.2013.08.021.
Lindberg PA (1977) Rapport vedr. undersøkelser av nefelingehaltene i Lågendalen. Norsk hydro, pp 8.
Lindberg PA (1985) Fe-Ti-P Mineralizations in the Larvikite-Lardalite Complex, Oslo Rift. NGU Bulletin 402:93-98.
Lutro O, Nordgulen Ø (2008) Oslofeltet. Berggrunnskart 1: 250 000.
Mansur ET, Coint N, Slagstad T, Miranda ACR, Huyskens M, Andersen T (submitted) Temporal, spatial and compositional relationships between alkaline intrusions and associated Fe-Ti-P

mineralisation in the southern Oslo Rift, Norway: constraints from whole-rock geochemistry and U-Pb and Hf isotopes systematics in zircon. Norwegian Journal of Geology.
Marks MAW, Hettmann K, Schilling J, Frost BR, Markl G (2011) The Mineralogical Diversity of Alkaline Igneous Rocks: Critical Factors for the Transition from Miaskitic to Agpaitic Phase Assemblages. Journal of Petrology 52:439-455. doi: 10.1093/petrology/egq086.
McClenaghan MB, Spirito W, Day S, McCurdy M, McNeil R, Adcock S (2021) Overview of surficial geochemistry and indicator mineral surveys and case studies from the Geological Survey of Canada's GEM Program. Geochemistry: Exploration, Environment, Analysis 22:geochem2021-2070. doi: 10.1144/geochem2021-070.
McEnroe SA, Fabian K, Robinson P, Gaina C, Brown LL (2009) Crustal magnetism, lamellar magnetism and rocks that remember. Elements 5:241-246.
McLemore VT, Kogel J, Trivedi N, Barker J, Krukowski S (2006) Nepheline syenite. Industrial Minerals & Rocks (7th Edition) Published by Society for Mining, Metallurgy, and Exploration, Inc, Colorado:653-670.
McMartin I, McClenaghan MB (2001) Till geochemistry and sampling techniques in glaciated shield terrain: a review.
Morimoto N (1988) Nomenclature of Pyroxenes. Mineralogical Magazine 52:535-550. doi: DOI 10.1180/minmag.1988.052.367.15.
Nabighian MN, Grauch VJS, Hansen RO, LaFehr TR, Li Y, Peirce JW, Phillips JD, Ruder ME (2005) The historical development of the magnetic method in exploration. Geophysics 70:33ND-61ND.
Namur O, Charlier B, Holness MB (2012) Dual origin of Fe-Ti-P gabbros by immiscibility and fractional crystallization of evolved tholeiitic basalts in the Sept Iles layered intrusion. Lithos 154:100-114. doi: 10.1016/j.lithos.2012.06.034.
Neumann E-R (1980) Petrogenesis of the Oslo region larvikites and associated rocks. Journal of Petrology 21:499-531.
Neumann E-R, Tilton GR, Tuen E (1988) Sr, Nd and Pb isotope geochemistry of the Oslo rift igneous province, southeast Norway. Geochim Cosmochim Ac 52:1997-2007. doi: https://doi.org/10.1016/0016-7037(88)90180-9.
Neumann ER, Dunworth EA, Sundvoll BA, Tollefsrud JI (2002) B1 basaltic lavas in Vestfold–Jeløya area, central Oslo rift: derivation from initial melts formed by progressive partial melting of an enriched mantle source. Lithos 61:21-53. doi: https://doi.org/10.1016/S0024-4937(02)00068-3.
Neumann ER, Wilson M, Heermans M, Spencer EA, Obst K, Timmerman MJ, Kirstein L (2004) Carboniferous-Permian rifting and magmatism in southern Scandinavia, the North Sea and northern Germany: a review In: Wilson M, Neumann E-R, Davies GR, Timmerman MJ, Heermans M, Larsen BT (eds) Permo-Carboniferous Magmatism and Rifting in Europe. The Geological Society of London, pp 11-40.
Neumann ER (2019) Origin and evolution of the early magmatism in the Oslo Rift (Southeast Norway): Evidence from multiple generations of clinopyroxene. Lithos 340:139-151. doi: 10.1016/j.lithos.2019.04.025.
Niobec (2013) Expansion project of the Niobec Mine in Saint-Honoré.
Olaussen S, Larsen BT, Steel R (1994) The Upper Carboniferous-Permian Oslo Rift; basin fill in relation to tectonic development. Can Soc Petrol Geol Mem 17:175-197.
Pedersen LE, Heaman LM, Holm PM (1995) Further Constraints on the Temporal Evolution of the Oslo Rift from Precise U-Pb Zircon Dating in the Siljan-Skrim Area. Lithos 34:301-315. doi: Doi 10.1016/0024-4937(94)00014-S.
Petersen JS (1978) Structure of the Larvikite-Lardalite complex, Oslo-region, Norway, and its evolution. Geologische Rundschau 67:330-342.
Philpotts AR (1967) Origin of certain iron-titanium oxide and apatite rocks. Economic Geology 62:303-315. doi: 10.2113/gsecongeo.62.3.303.
Plouffe A, Ferbey T, Levson V, Bond J (2012) Glacial history and drift prospecting in the Canadian Cordillera: recent developments. Geological Survey of Canada, Open File 7261:51.
Plouffe A, Kjarsgaard I, Ferbey T, Wilton D, Petts D, Percival J, Kobylinski C, McNeil R (2022) Detecting buried porphyry Cu mineralization in a glaciated landscape: a case study from the Gibraltar Cu-Mo deposit, British Columbia, Canada. Economic Geology 117:777-799.
Prado EMG, de Souza Filho CR, Carranza EJM, Motta JG (2020) Modeling of Cu-Au prospectivity in the Carajás mineral province (Brazil) through machine learning: Dealing with imbalanced training data. Ore Geology Reviews 124:103611.

Rämö OT, Andersen T, Whitehouse MJ (2022) Timing and Petrogenesis of the Permo-Carboniferous Larvik Plutonic Complex, Oslo Rift, Norway: New Insights from U-Pb, Lu-Hf and O Isotopes in Zircon. Journal of Petrology 63:1-29. doi: 10.1093/petrology/egac116.
Rasmussen E, Neumann ER, Andersen T, Sundvoll B, Fjerdingstad V, Stabel A (1988) Petrogenetic Processes Associated with Intermediate and Silicic Magmatism in the Oslo Rift, South-East Norway. Mineralogical Magazine 52:293-307. doi: DOI: 10.1180/minmag.1988.052.366.01.
Reich M, Simon AC, Barra F, Palma G, Hou T, Bilenker LD (2022) Formation of iron oxide–apatite deposits. Nature Reviews Earth & Environment. doi: 10.1038/s43017-022-00335-3.
Schjølberg M (2023) Geochemical & Mineralogical assessment of the Anundsjøen, Larvik Potential Nepheline Syenite for use in glass and ceramics. Norwegian University of Science and Technology, NTNU, pp 89.
Schmidt MW, Connolly JAD, Günther D, Bogaerts M (2006) Element Partitioning: The Role of Melt Structure and Composition. Science 312:1646-1650.
Slagstad T, Marker M, Roberts NMW, Saalmann K, Kirkland CL, Kulakov E, Ganerod M, Rohr TS, Mokkelgjerd SHH, Granseth A, Sorensen BE (2020) The Sveconorwegian orogeny - Reamalgamation of the fragmented southwestern margin of Fennoscandia. Precambrian Research 350.
Slagstad T, Skår Ø, Bjerkan G, Coint N, Granseth A, Kirkland CL, Kulakov E, Mansur E, Orvik AA, Petersson A (2024) Subduction and loss of continental crust during the Mesoproterozoic Sveconorwegian Orogeny. Precambrian Research 409:107454.
Smith WH, Wessel P (1990) Gridding with continuous curvature splines in tension. Geophysics 55:293-305.
Sundvoll B, Larsen B (1990) Rb-Sr isotope systematics in the magmatic rocks of the Oslo rift.
Szitkar F, Dyment J (2015) Near-seafloor magnetics reveal tectonic rotation and deep structure at the TAG (Trans-Atlantic Geotraverse) hydrothermal site (Mid-Atlantic Ridge, 26 N). Geology 43:87-90.
Szitkar F, Dyment J, Petersen S, Bialas J, Klischies M, Graber S, Klaeschen D, Yeo I, Murton BJ (2019) Detachment tectonics at Mid-Atlantic Ridge 26 N. Sci Rep-Uk 9:11830.
Szitkar F, Gernigon L, Lim A, Brönner M (2023) Oceanic Core Complex or not? When bathymetric structures challenge seafloor spreading models. Tectonophysics 849:229734.
Thébault E, Finlay CC, Beggan CD, Alken P, Aubert J, Barrois O, Bertrand F, Bondar T, Boness A, Brocco L (2015) International geomagnetic reference field: The 12th generation. Earth, Planets and Space 67:1-19.
Tollari N, Barnes SJ, Cox RA, Nabil H (2008) Trace element concentrations in apatites from the Sept-Îles Intrusive Suite, Canada — Implications for the genesis of nelsonites. Chemical Geology 252:180-190. doi: https://doi.org/10.1016/j.chemgeo.2008.02.016.
Tremblay J, Bédard L, Matton G (2015) A petrographic study of Nb-bearing minerals at the Saint-Honoré niobium deposit. Br Columbia Geol Surv Pap 3:75-81.
Veksler IV, Dorfman AM, Danyushevsky LV, Jakobsen JK, Dingwell DB (2006) Immiscible silicate liquid partition coefficients: implications for crystal-melt element partitioning and basalt petrogenesis. Contrib Mineral Petrol 152:685-702. doi: 10.1007/s00410-006-0127-y.
Wang L, Peeters L, MacKie EJ, Yin Z, Caers J (2023) Unraveling the uncertainty of geological interfaces through data-knowledge-driven trend surface analysis. Computers & Geosciences 178:105419.
Wang Y, Coint N, Mansur ET, Acosta-Gongora P, Miranda ACR, Nasuti A, Baranwal VC (2024) Leveraging Domain Expertise in Machine Learning for Critical Metal Prospecting in the Oslo Rift: A Case Study for Fe-Ti-P-Rare Earth Element Mineralization. Minerals-Basel 14:377.

GEOLOGICAL
SURVEY OF
NORWAY

· NGU ·

Geological Survey of Norway
PO Box 6315, Sluppen
N-7491 Trondheim, Norway

Visitor address
Leiv Eirikssons vei 39
7040 Trondheim

Tel (+ 47) 73 90 40 00
E-mail ngu@ngu.no
Web www.ngu.no/en-gb/